



Flow Assurance Risks in Multistage Centrifugal Pumps: Investigating Design and Operation Variables During Reflux

Willem Sibinga Mulder

Flow Assurance Risks in Multistage Centrifugal Pumps:

Investigating Design and Operation Variables
During Reflux

Willem Sibinga Mulder

To obtain the degree of Master of Science
at the Delft University of Technology.

Student number:	4685644	
Project duration:	April, 2024 – February, 2025	
Thesis committee:	Dr. Ir. R.L.J. Helmons (Chair), Dr. ir. A.M. Talmon, Ir. F. van Grunsven,	TU Delft, TU Delft Allseas

Style:	Modified TU Delft Report Style
Language Check:	Grammarly and ChatGPT

This thesis is confidential and cannot be made public until February 4, 2024.

An electronic version of this thesis is available at <http://repository.tudelft.nl/>.

Preface

This report marks the completion of my thesis project, *Flow Assurance Risk in Multi-Stage Centrifugal Pumps: Investigating Design and Operation Variables during Reflux*. It also concludes my MSc program in Offshore and Dredging Engineering at Delft University of Technology.

Over the past ten months, I have dedicated significant effort to this project, combining theoretical research with an experimental phase. Designing and constructing a test setup was something I aspired to include in my thesis, and I am pleased that this goal was achieved. The process was both challenging and rewarding.

I would like to thank my daily supervisors, Dr. Ir. Rudy L.J. Helmons and Ir. Frans van Grunsven, for their guidance, constructive feedback, and encouragement. Their support during meetings and discussions has been a great help throughout this project.

Special thanks also go to Ed Stok, Huib Zuurmond, André van den Bosch, and others who supported me during the experimental phase, as well as to the employees at Allseas who provided advice and assistance along the way.

Finally, I want to thank Allseas for sponsoring this project and providing the facilities and resources needed to carry it out successfully.

*Willem Sibinga Mulder
Delft, January 2025*

Summary

Deep-sea mining (DSM) focuses on extracting valuable resources, such as polymetallic nodules, from seabeds at depths of up to 5000 meters. These nodules contain critical metals but pose technical challenges due to extreme conditions like high pressure and long transport distances.

A critical component of deep-sea mining (DSM) is the vertical transport system (VTS), which lifts nodules from the seabed to the surface using a riser system with two-phase (solid-liquid) or three-phase (solid-liquid-gas) flow. The VTS plays a vital role in determining throughput, energy consumption, and the overall stability of the mining operation. Multistage centrifugal pumps are promising for powering the VTS due to their ability to handle high pressures and coarse solids. While the risk of blockages is minimal under normal operating conditions, flow assurance within the pump becomes a significant concern during reflux situations. In such cases, gravity causes the nodule-water mixture to reverse direction, substantially increasing the risk of blockages and clustering. This highlights the importance of analysing reflux scenarios in greater detail to ensure reliable system performance.

To address these challenges during reflux, a test setup is developed to investigate operational and design variables as well as pump geometry. Two model pumps were constructed: one without impeller and diffuser blades, focusing on the effects of internal spacing, and one with blades, aimed at evaluating overall reflux performance. The key vulnerabilities identified in this thesis provide a clear understanding of where issues may arise in the pump design and the underlying mechanisms causing them. This knowledge enables potential users of the multistage centrifugal pump to make informed adjustments, preventing flow assurance challenges in their systems.

Both the pump geometry and mixture variables were thoroughly analysed. For the geometry, the curvature of the impeller blades was found to cause solid accumulation at the entry, posing a significant risk of blockages. This research identified the issue and proposed modifications to the blade edges, which proved highly effective in eliminating accumulation and significantly improving solid flow. Narrowing diffuser vanes and shallow blade inclination were found to promote contact-dominated flow, velocity reductions, and obstructions. At the diffuser-impeller transition, solids entering from multiple directions caused bridging and blockages. Mixture variables also had a notable impact. Solids within the pump's design specifications passed through unobstructed when processed in single-solid batches. However, increased solid concentration at the pump inlet led to accelerating blockage formation. Higher-density solids demonstrated better performance by maintaining higher velocities and reducing the risk of obstructions.

To enhance future testing, it is recommended to use transparent materials, as implemented in this study. This approach provided valuable insights into the flow dynamics and greatly improved the ability to observe and analyse potential blockages. Additionally, optimizing the geometry of the impeller and diffuser blades is critical for improving the pump's overall performance. Adjustments should focus on reducing blockages and promoting smooth solid flow, while carefully balancing throughput efficiency and pump capacity. These design improvements are essential to ensure reliable and efficient operation, particularly in demanding applications as deep-sea mining.

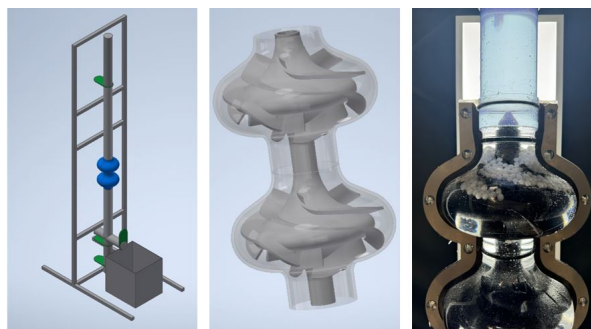


Figure 1: Left: Experimental setup, Middle: Overview of the 3D model of the pump, Right: Visualization of obstructions within the pump.

Contents

Preface	i
Summary	ii
Nomenclature	ix
1 Introduction	1
1.1 The System	3
1.2 Problem Definition	4
1.3 Research Objectives	4
1.4 Research Questions	4
1.5 Research Approach	5
2 Literature	6
2.1 Introduction	6
2.2 Vertical Hydraulic Transport	6
2.2.1 Hydraulic Lifting	6
2.2.2 Pumping Mechanisms	8
2.3 Multi-stage Centrifugal Pump	11
2.4 Particle Dynamics in Multi-Stage Centrifugal Pumps	14
2.4.1 Flow Assurance in Pumps	14
2.4.2 Particle Transport	17
2.4.3 Dimensionless Flow Parameters	18
2.5 Conclusion	19
3 Methodology	21
3.1 Introduction	21
3.2 Design Phase	22
3.2.1 3D Model Pump	22
3.3 Experimental Setup	25
3.3.1 Overview Setup	25
3.3.2 Experimental Measurement	28
3.4 Experiments as planned	28
3.4.1 A: Fallpipe Experiments	29
3.4.2 B: Pump without Blades Experiments	29
3.4.3 C: Pump with Blades Experiments	30
4 Fallpipe Experiment	31
4.1 Introduction	31
4.2 Series A1: Terminal Settling Velocity	31
4.3 Series A2: Settling Behavior of Batch	34
4.4 Take Away: Fallpipe	35
5 Pump Without Blades Experiment	36
5.1 Introduction	36
5.2 Series B1: Test Matrix	36
5.3 Series B2: In-Depth Analyses	38
5.4 Series B3: Shortened Fallpipe	42
5.5 Conclusion: Pump Without Blades	43
6 Pump With Blades Experiment	44
6.1 Introduction	44
6.2 Series C1: Initial Evaluation	45
6.3 Series C2: Performance Analysis	49
6.4 Series C3: Adjusted Pump	52
6.5 Take Away: Pump With Blades	56

7	Practical Implications	57
7.1	Stages	57
7.2	Hydrostatic Pressure Difference	57
7.3	Connection of Pump Housing	57
7.4	Comparison to Previous Research by OMI:	58
8	Conclusion and Recommendations	59
8.1	Conclusion	59
8.1.1	Flow Assurance	59
8.1.2	Blockage Mechanisms	59
8.1.3	Vulnerable Pump Areas	60
8.1.4	Influence of Variables	60
8.1.5	Evaluation of Experimental Setup for Investigating Reflux and Flow Assurance in Multi-Stage Centrifugal Pumps	60
8.2	Recommendations	61
8.2.1	Recommendations for Future Testing	61
8.2.2	Recommendations for an Improved Setup	61
8.2.3	Adjustments for the Current Test Setup	61
	References	62
A	Python Code: Particle Reynolds Number	65
B	Python Code: Required Pump Pressure	67
C	Testing	68
D	Pump-Pipe Connection Drawing	72
E	Fallpipe Settling	74
F	Pump One: Pump Without Blades	85
G	Drag Force	87
H	Pump Two: Pump With Blades	90
I	Confirmation Tests	97
J	List of tests	103

List of Figures

1	Left: Experimental setup, Middle: Overview of the 3D model of the pump, Right: Visualization of obstructions within the pump.	ii
1.1	Overview of Clarion Clipperton [41]	2
1.2	Overview Nodule Field [41]	3
1.3	Autonomous SCV's and Riser-Based [62]	3
1.4	Overview of System: 1- Production Support Vessel, 2- Umbilical cable, 3- Nodule collector, 4- Jumper hose, 5- Riser base, 6- Riser, 7- Multi-stage centrifugal pump, 8- Riser, 9- Motor, 10- Pump housing, 11- Pump stage. [17]	4
2.1	Overview hydraulic lifting [9]	6
2.2	Sections of a representative slurry pump [33]	8
2.3	Positive Displacement Pump [27]	9
2.4	Overview of System: 1- Production Vessel, 2- Umbilical cable, 3- Nodule collector, 4- Jumper hose, 5- Riser base, 6- Riser, 7- Multi-stage centrifugal pump, 8- Riser, 9- Motor, 10- Pump housing, 11- Pump stage. [17]	10
2.5	Schematic diagram of airlifting system [14]	10
2.6	Over-all structure of six-stage lifting motor pump. 1-Inlet flange, 2- Motor barrel, 3-Motor, 4 Connection section, 5- Coupling, 6- Suction housing, 7-Slide bearing, 8- Pump shaft, 9- Impeller 1 , 10- Space guide, 11- Pump body seal ring, 12- Impeller port ring, 13 Impeller 2, 14- Damper disc, 15 - Pump cylinder body, 16 - Outlet flange. [23]	11
2.7	Design parameters for the impeller [36]	12
2.8	Impeller velocity diagrams (1 = inlet, 2 = outlet) [42]	13
2.9	(a) Computational model overview for a two-stage pump, and (b) splitter plate layout.	14
2.10	1. Transition of the pipeline into the pump. 2. Transition from the first to the second stage. 3. Junction between the impeller and the diffuser. [13]	15
2.11	Pressure cloud on the guide vane after being collided with 10–20 mm particles: (a) pressure cloud graph at 2 s; (b) pressure cloud graph at 10 s; (c) pressure cloud graph at 15s [13]	16
2.12	Pressure cloud on the guide vane after being collided with 20–30 mm particles: (a) pressure cloud graph at 2 s; (b) pressure cloud graph at 10 s; (c) pressure cloud graph at 15s [13]	16
2.13	2D cross-sectional visualization of pump with solids highlighted in black to illustrate internal flow channels.	16
3.1	Model pump	22
3.2	Overview of the pump specifications used for experimental tests. The key components are labeled as follows: (1) Minimum Shaft Diameter, (2) Incl. Key, Hub Diameter, (3) Solid Passage Diameter, (4) Ball Passage Diameter, (5) Impeller Eye Diameter, (6) Diffuser Support Thickness, (7) Blade Thickness, (8) Impeller Outlet Diameter, (9) Impeller Outlet Width, (10) Impeller Hub-to-Shroud Distance, (11) Diffuser Inlet Diameter.	23
3.3	Comparison of the test setup	25
3.4	Configurations of the fallpipe	26
3.5	Influence of installed tube on initial concentration batch	26
3.6	Overview lower part setup. (Green box: water outlet valve, Red box: Solid collector, Blue box: Screw cap, Yellow box: Fallpipe)	27
3.7	Comparison of 3D printed pump models: (a) and (b) without blades, (c) and (d) with blades.	27
3.8	Fastec IL5	28
3.9	Overview Experimental tests	28
4.1	Wall friction	32
4.2	Comparison of measured and theoretical terminal settling velocities for Glass and POM spheres	33

4.3	Overview of Settling behavior Test Glass Spheres, 20 mm, Initial Concentration 46%, Batch Height 20 cm, Timestamp 0.297 s)	34
4.4	Overview of Settling behavior Test (Glass Spheres, 10 mm, Initial Concentration 26%, Batch Height 20 cm, Timestamp: 0.297 s)	34
5.1	Comparison of Left and Right Views: Test Results with 30 mm Solid Showing Solids Retained at Different Locations.	37
5.2	Results for 30 mm POM spheres under varying batch heights and concentrations.	38
5.3	Test results for Pump One with 30 mm POM spheres.	39
5.4	Solid entrapment locations from tests, summarizing results from a total of 40 tests.	39
5.5	Results showing various issues: (a) Arrival of the solid cluster, (b) Solids retained at diffuser support, and (c) Obstruction with multiple solid sizes.	42
6.1	Comparison of throughput at initial batch concentrations. The results are shown for glass spheres and POM spheres.	46
6.2	Comparison between 10 mm and 20 mm solid obstruction	47
6.3	Diffuser Vanes Obstructions.	47
6.4	Impeller barrier blockages.	48
6.5	Diffuser vanes blockages.	48
6.6	Throughput for all batch types: the upper graph represents glass spheres, and the lower graph represents POM spheres.	50
6.7	Comparison of impeller obstructions for glass spheres and POM spheres.	51
6.8	Impeller blades adjustment.	52
6.9	Results for Type 3 glass spheres (10, 14, 17, 20, and 25 mm). Only Type 3 is shown as other types were not tested.	53
6.10	Results for all types with POM spheres.	53
6.11	Visualization of obstructions: (a) Transition between diffuser and impeller and (b) Connection between pump halves.	54
6.12	Extension of the blockage upward along the diffuser blade.	54
6.13	Transition Blockage Animation.	55
7.1	Cross-section of the pump stage used by OMI, showing the defined angle as described in [43].	58
C.1	L: Nodule dispenser 55 % and 10cm height, R: Nodule dispenser 26% and height of 20 cm	68
D.1	Drawing Pump Model	73
E.1	Glass spheres - Solid Size:5mm	74
E.2	Glass spheres - Solid Size 10mm	74
E.3	Glass spheres - Solid Size 15mm	75
E.4	Glass spheres - Solid Size 20mm	75
E.5	Glass spheres - Solid Size 25mm	75
E.6	Glass spheres - Solid size 25mm	76
E.7	Comparison of Velocities: Test Data vs Theoretical Models for Density 2400 kg/m ³ ($R^2 = 0.90$)	76
E.8	POM spheres - Solid Size 5mm	77
E.9	POM spheres - Solid Size 10mm	77
E.10	POM spheres - Solid Size 15mm	77
E.11	POM spheres - Solid Size 20mm	78
E.12	POM spheres - Solid Size 25mm	78
E.13	POM spheres - Solid Size 30mm	78
E.14	Comparison of Velocities: Test Data vs Theoretical Models for Density 1400 kg/m ³ ($R^2 = 0.90$)	79
E.15	Comparison of measured and theoretical velocities for filtered data, 2400kg/m ³ ($R^2 = 0.81$) 1400kg /m ³ ($R^2 = 0.88$)	79
E.16	Overview of settling behaviour test 4004 (2400 kg/m ³ , 20 mm, initial density 46, batch height 10 cm)	80
E.17	Overview of settling behaviour test 4008 (2400 kg/m ³ , 20 mm, initial density 46, batch height 20 cm)	80

E.18 Overview of settling behaviour test 4013 (2400 kg/m ³ , 20 mm, initial density 26, batch height 20 cm)	80
E.19 Overview of settling behaviour test 4016 (2400 kg/m ³ , 10 mm, initial density 26, batch height 10 cm)	81
E.20 Overview of settling behaviour test 4019 (2400 kg/m ³ , 10 mm, initial density 26, batch height 20 cm)	81
E.21 Overview of settling behaviour test 4022 (2400 kg/m ³ , 10 mm, initial density 46, batch height 10 cm)	81
E.22 Overview of settling behaviour test 4025 (2400 kg/m ³ , 10 mm, initial density 46, batch height 20 cm)	82
E.23 Overview of settling behaviour test 5002 (1400 kg/m ³ , 20 mm, initial density 26, batch height 10 cm)	83
E.24 Overview of settling behaviour test 5005 (POM spheres, 20 mm, initial concentration 46%, batch height 20 cm, Timestamp: 0.509s)	83
E.25 Overview of settling behaviour test 5007 (1400 kg/m ³ , 20 mm, initial density 26, batch height 10 cm)	83
E.26 Overview of settling behaviour test 5010 (1400 kg/m ³ , 20 mm, initial density 46, batch height 20 cm)	84
E.27 Overview of settling behaviour test 5018 (POM spheres, 10 mm, initial concentration 26%, batch height 20 cm, Timestamp: 0.509s)	84
E.28 Overview of settling behaviour test 5023 (1400 kg/m ³ , 10 mm, initial density 46, batch height 20 cm)	84
F.1 Test 7001 to 7010 (1400 kg/m ³ , 30mm, Initial batch concentration 55%, bed height 20cm	85
F.2 Test 7021 to 7030 (1400 kg/m ³ , 30mm, Initial batch concentration 55%, Batch height 10cm	85
F.3 Test 7031 to 7040 (1400 kg/m ³ , 30mm, Initial batch concentration 26%, Batch height 20cm	86
F.4 Test 7011 to 7020 (1400 kg/m ³ , 30mm, Initial batch concentration 26%, Batch height 10cm	86
G.1 Situation sketch Drag Force	87
G.2 Velocity vector and streamline patterns for a sphere-to-tube diameter ratio of 0.5, $Re = 100$, and $n = 1$ [4].	88
G.3 Flow visualization around the sphere at $G/D = 0.5$ and $Re = 5000$. The left panel shows the flow structure visualized using laser illumination and a Rhodamine dye injection technique, the middle panel presents the normalized instantaneous velocity (V), and the right panel depicts the dimensionless vorticity (ω^*). [12]	88
G.4 Schematic of sphere motion in the channel [16]	89
H.1 Comparison for sizes 10, 14, and 20 with density 2400 kg/m ³	90
H.2 Comparison for sizes 10, 17, and 25 with density 2400 kg/m ³	90
H.3 Comparison for sizes 10, 14, 17, 20, and 25 with density 2400 kg/m ³	91
H.4 Throughput comparison for sizes 10, 14, and 20 (3000 g)	91
H.5 Throughput comparison for sizes 10, 14, 17, 20, and 25 (3000 g)	91
H.6 Comparison for sizes 10, 14, and 20 with density 1400 kg/m ³	92
H.7 Comparison for sizes 10, 17, and 25 with density 1400 kg/m ³	92
H.8 Comparison for sizes 10, 14, 17, 20, and 25 with density 1400 kg/m ³	93
H.9 Average throughput for sizes 10, 14, and 20 with density 1400 kg/m ³	93
H.10 Throughput comparison for sizes 10, 14, 17, 20, and 25 (1500 g) at 2400 kg/m ³	94
H.11 Throughput comparison for sizes 10, 14, 17, 20, and 25 (3000 g) at 2400 kg/m ³	94
H.12 Throughput comparison for sizes 10, 14, 17, 20, and 25 (878 g) at 1400 kg/m ³	94
H.13 Throughput comparison for sizes 10, 14, and 20 (878 g) at 1400 kg/m ³	95
H.14 Throughput comparison for sizes 10, 17, and 25 (878 g) at 1400 kg/m ³	95
H.15 Throughput comparison for sizes 10, 14, 17, 20, and 25 (1745 g) in Mixed configuration at 1400 kg/m ³	95
I.1 Overview of Confirmation Test Setup	97
I.2 Frame from Confirmation Test	97
I.3 Friction Test: Visual Analysis of Rolling vs Sliding	98
I.4 Force Balance: Forces Acting on the Solid	99

List of Tables

2.1	Overview of some Riser System Tests and Results in Deep-Sea Mining	8
3.1	Specifications of the Real-Life Pump and Model Pump	23
4.1	Summary of Mean Mass and Mean Terminal Settling Velocity for Glass Spheres	32
4.2	Summary of Mean Mass and Mean Terminal Settling Velocity for POM Spheres	32
5.1	Summary of Results for POM Spheres by Size, Concentration, and Batch Height.	37
5.2	Weight and Approximate Number of Spheres for Different Initial Concentrations and Batch Heights.	37
5.3	Summary of results showing blockages for different solid sizes under layered and mixed conditions	41
5.4	Summary of retained data for POM spheres, categorized by size, density, and initial concentration, including the amount retained in grams and percentage.	42
6.1	Overview of Tests Conducted in Series C1	45
6.2	Overview of Tests Conducted in Series C2	49
6.3	Overview of Tests Conducted in Series C3	52
6.4	Summary of average number of blockages for POM spheres at different locations under various configurations.	55
C.1	Summary of Results for Tests with Different Densities and Sizes	69
C.2	Step-by-Step Experimental Procedure	71
H.1	Summary of Throughput and Percentages for Different Sizes and Situations (Glass Spheres)	92
H.2	Summary of Throughput and Percentages for Different Sizes and Situations (POM Spheres)	93
H.3	Summary of Throughput and Percentages for Different Sizes and Situations Glass Spheres)	94
H.4	Summary of Throughput and Percentages for Different Sizes and Situations (POM Spheres)	96
H.5	Summary of Blockages for Different Situations at Various Concentration (POM Spheres)	96

Nomenclature

Abbreviations

Abbreviation	Definition
CFD	Computational Fluid Dynamics
CCZ	Clarion-Clipperton Zone
DEM	Discrete Element Method
DNC	Deep-Sea Nodule Collection
ESP	Electrical Submersible Pump
FDM	Fused Deposition Modeling
ISA	International Seabed Authority
OMI	Ocean Mining Inc.
PD	Positive Displacement
PLA	Polylactic Acid
PSD	Particle Size Distribution
POM	Polyoxymethylene
RPM	Revolutions Per Minute
SCV	Seabed Collection Vehicle
SMS	Seafloor Massive Sulfides
VHS	Vertical Hydraulic System
VIV	Vortex-Induced Vibrations
VTS	Vertical Transport System

Symbols

Symbol	Definition	Unit
A	Projected area of the particle perpendicular to the flow	[m ²]
B	Cross-sectional area at the shaft in pump geometry	[m ²]
C_D	Drag coefficient	[-]
C_f	Friction coefficient	[-]
C_{avg}	Average concentration	[-] Or [%]
$C_{arrival}$	Arrival concentration	[-] Or [%]
C_i	Initial batch concentration	[-] Or [%]
C_v	Volume concentration	[-] Or [%]
D	Pipe diameter	[m]
D_{in}	Inner pipe diameter	[m]
D_{out}	Outer pipe diameter	[m]
d	Particle diameter	[m]
d_{solid}	Solid passage diameter	[m]
d_{ball}	Ball passage diameter	[m]
Fr	Froude number	[-]
g	Gravitational acceleration	[m/s ²]
H	Head generated by the pump	[m]
h_b	Batch height	[m]
h_f	Head loss due to friction	[m]
I	Moment of inertia	[kg·m ²]
k	Scaling factor	[-]
L	Length	[m]
m	Mass	[kg]
n	Empirical exponent	[-]

Symbol	Definition	Unit
N	Rotational speed of the pump	[rpm]
P	Pressure	[kPa]
Q	Cross-sectional averaged volumetric flow rate	[m ³ /s]
Re	Reynolds number	[-]
Re_p	Particle Reynolds number	[-]
St	Stokes number	[-]
t	Time	[s]
t_{thick}	Thickness [m]	
v_{arrival}	Arrival velocity [m/s]	
v_f	Fluid velocity	[m/s]
v_t	Terminal settling velocity	[m/s]
v_{th}	Hindered settling velocity	[m/s]
v'_{th}	Adjusted hindered settling velocity	[m/s]
v''_{th}	Adjusted hindered settling velocity with correction	[m/s]
	term α	
W	Relative velocity	[m/s]
w_s	Weight solids	[g]
$\overline{w_s}$	Measured weight solids	[g]
Z	Number of blades	[-]
ϵ	Pipe roughness	[m]
μ	Dynamic viscosity	[Pa·s]
ν	Kinematic viscosity	[m ² /s]
ω	Angular velocity	[rad/s]
ρ	Density	[kg/m ³]
ρ_f	Fluid density	[kg/m ³]
ρ_s	Solid density	[kg/m ³]
τ_w	Shear stress at the wall	[Pa]

1

Introduction

Deep-sea mining (DSM) refers to the extraction of valuable minerals and metals from the seabed, often at depths exceeding several kilometers. The ocean floor is rich in resources such as polymetallic nodules, cobalt-rich crusts, and massive sulfides, which contain metals like nickel, cobalt, and other rare minerals. These resources are increasingly viewed as crucial for supporting the global transition to green technologies[28].

In 1960, DSM was already considered an interesting opportunity due to the high abundance, large quantities, and high concentrations of metals, which are often of higher grade than those found on land, making them economically more attractive. Between 1960 and 1980, researchers conducted a wide range of studies into DSM [58]. However, interest in DSM faded around 1980 due to falling commodity prices, changes in international maritime law marking the ocean floor beyond national jurisdiction as the common heritage of mankind, and the easing of tensions between the global North and South. These factors led companies and states to lose interest in DSM [54]. Now, with the rise of decarbonization and the global 'green shift,' there is renewed interest in DSM, driven by the demand for metals like nickel and cobalt, which are essential for green technologies [28]. According to the World Bank, demand for these resources is expected to increase by 500 percent by 2050 compared to 2018 levels [47]. Although there are still enough land-based resources, extraction is expensive due to low ore grades and overburden, and it often involves high social and environmental costs. As a result, an increasing number of countries are hesitant to open new mines [61].

Companies and research institutions are working to address the challenges of developing viable DSM systems. Achieving viability in this context requires balancing three critical aspects: technological feasibility, economic profitability, and minimizing environmental impacts. Key priorities include creating efficient, cost-effective extraction technologies, promoting environmentally sustainable mining practices, and establishing strong regulatory frameworks.

While advancements in technology and regulatory frameworks are helping to pave the way for DSM, the industry faces significant opposition due to environmental and social concerns. The potential impacts on marine ecosystems could be substantial, including releasing toxic substances and creating sediment plumes that may disrupt marine life if not handled carefully[43, 34]. Additionally, social concerns include inequitable profit distribution, where the benefits may disproportionately favor a few companies or nations rather than benefiting humanity as a whole, as intended under the "common heritage of mankind" principle. This could worsen economic inequality, leaving developing countries without fair compensation while they face environmental risks [60]. Another potential social disruption of DSM is that countries which heavily rely on revenues from land-based mines could face declining income, as mineral prices may drop due to an increased and potentially cheaper supply from deep-sea sources, disrupting traditional mining markets [29].

The International Seabed Authority (ISA) is responsible for regulating and managing activities in the international seabed area beyond national jurisdiction. Currently, the ISA only permits exploration, and obtaining an exploration license does not guarantee approval. Companies are now awaiting the ISA's decision on new regulations that could potentially allow resource exploitation [26]. The ISA plays a central role in shaping the future of DSM. Its responsibilities include granting exploration licenses, addressing environmental concerns, developing mining codes, monitoring compliance, and ensuring that

the benefits of seabed resource exploitation are distributed equitably worldwide. Deep-sea mining will only proceed if the ISA determines that its environmental, social, and economic impacts are acceptable [40, 2]. The ISA's decisions will be crucial in defining the trajectory of DSM, ensuring alignment with global sustainability goals and the responsible utilization of seabed resources.

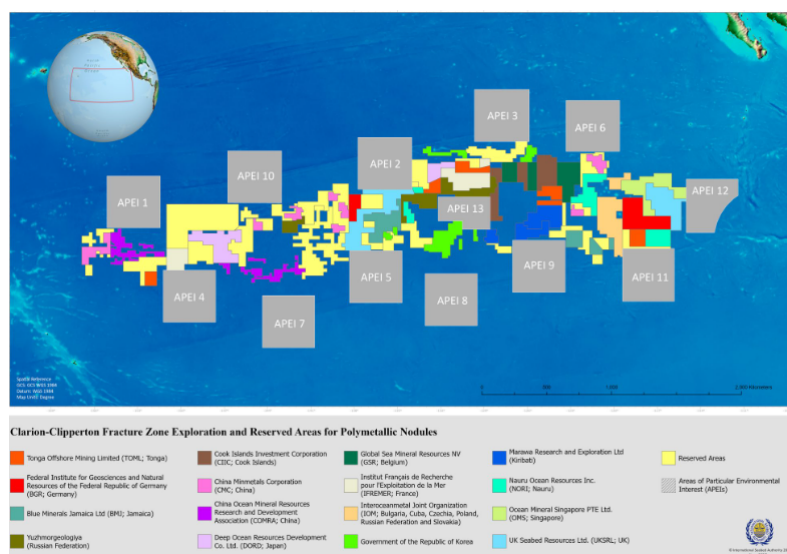


Figure 1.1: Overview of Clarion Clipperton [41]

In the previous section, DSM was discussed generally, highlighting its renewed interest due to the increasing demand for critical metals driven by decarbonization efforts. However, DSM refers to several types of mining, targeting different types of deposits found in various oceanic environments. These include polymetallic nodules, seafloor massive sulfides, and cobalt-rich ferromanganese crusts [3, 46, 8].

- **Polymetallic nodules:** potato-sized mineral/rock formations, rich in metals such as nickel, copper, cobalt, and manganese, Typically found at depths of 4,000 to 6,000 meters and notable for being free of sediment, resting atop the ocean floor.
- **Seafloor massive sulfides:** Form near hydrothermal vents along mid-ocean ridges, where mineral-rich fluids are expelled and settle, creating dense deposits of copper, zinc, and other metals. Located in volcanically active regions [52].
- **Cobalt-rich ferromanganese crusts:** Found on the slopes of seamounts, rich in cobalt, manganese, platinum, and rare earth elements. These crusts grow slowly over millions of years, forming hard layers on rocky substrates[52].

Each of these deposits presents specific extraction challenges depending on their environment, depth, and mineral composition, influencing the economic and technological feasibility of the different types of operations[53].

In this thesis, the focus is specifically on the collection of polymetallic nodules, while other types of DSM are excluded. Polymetallic nodules are found in various locations with differing conditions such as depth, abundance, size, and mineral concentrations[15]. Examples of these fields are the Cook Islands in the South Pacific and the Clarion-Clipperton Zone (CCZ) a vast area in international waters between Mexico and Hawaii. [40, 34]. An overview of the Clarion-Clipperton Zone is shown in Figure 1.1.

The polymetallic nodules that are found in the CCZ are potato-sized mineral/rock formations rich in metals such as nickel, copper, cobalt, and manganese, making them valuable for mining[3, 46, 8]. These nodules typically range between 2 to 10 cm in diameter. Nodule fields in this area can generally be classified into two types: areas with small nodules (up to 4 cm in diameter) that have smooth surfaces and high nodule abundance and areas with medium to large nodules (5-8 cm in diameter) that have clustered surfaces and low nodule abundance [34]. See Fig. 1.2 for an overview picture.



Figure 1.2: Overview Nodule Field [41]

1.1. The System

The previous section highlighted the growing interest in DSM and the economic potential of polymetallic nodules. This section shifts focus to the specific systems required for efficient nodule collection. Over the years, several approaches have been developed, including riser-based systems and autonomous mining vehicles [62, 35, 58, 39]. The following discussion will outline the components of these systems that have emerged as the most promising solutions. A potential valid nodule collection system can be divided into three primary components: the Nodule Collector, the Vertical Transport System for bringing nodules to the surface, and the Production Support Vessel responsible for processing and overseeing the operation. Different companies adopt varied approaches for each of these components.

Nodule Collector In most current concepts being developed by companies, the process begins with a Seabed Collection Vehicle (SCV). The SCV moves over the seabed, gathering polymetallic nodules embedded in the sediment. Since these nodules are loosely embedded, excavation is unnecessary [8]. This type of mining is known as deep-sea nodule collection (DNC). Within the SCV, initial sediment separation from the mixture of nodules, sediment, and water occurs [52, 11]. SCVs can either operate autonomously, functioning like shuttles, or remain connected to the vessel via an umbilical. An umbilical is a flexible cable that supplies power and communication between the production support vessel and the SCV.

Autonomous SCVs, such as those developed by Impossible Metals, are in the early stages of development and testing. They have been successfully demonstrated in controlled environments, placing them at a Technology Readiness Levels (TRL) of 6 [39]. Traditional mechanical collectors, connected to riser-based systems, have been tested in relevant deep-sea conditions, achieving a TRL of 7 [25].

Vertical Transport System For the Vertical Transport System (VTS) used to transport the nodules to the surface, there are two main options:

Riser-Based System In this system, the mining vessel is connected to an active nodule collector via a riser, a vertical pipeline used to efficiently transport nodules from the seabed to the surface. Various options are available for powering the riser system, such as airlift pumps and multi-stage centrifugal pumps [58]. A flexible section of the riser, the jumper, connects the rigid pipeline to the nodule collector, allowing for necessary movement [7, 14, 59]. Riser-based systems have been tested by companies such as Allseas in relevant and operational environments, placing them at a TRL of 7 [25].

Autonomous SCVs These SCVs operate as shuttles, traveling to and from the deep seabed to collect nodules and returning them to the mining vessel. However, this method faces challenges such as high operational costs, significant energy consumption, and the risk of losing shuttles [35, 58]. Companies like Impossible Metals are actively developing this system and claim that it can be made commercially viable [39]. These various systems are illustrated in Figure 1.3.

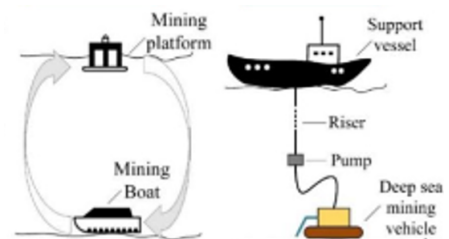


Figure 1.3: Autonomous SCV's and Riser-Based [62]

Production Support Vessel After being transported 4500 meters from the seabed, the mixture of nodules, water, and sediment reaches the mining vessel, where the nodules are separated from the mixture. The remaining water and sediment are typically returned to the ocean via a discharge pipeline at a designated water depth, usually chosen to minimize disruption to surface ecosystems. Regulating the discharge is crucial for minimizing the operation's environmental impact [1, 5]. In systems employing autonomous SCVs, discharge near the seabed could be feasible, as the sediment and water do not need to be transported to the surface.

1.2. Problem Definition

This research focuses on flow assurance challenges within a multi-stage centrifugal pump, a promising technology for vertical transport systems in Deep Sea Mining (DSM). However, the risk of blockages and system interruptions presents a significant challenge. By studying the impact of different mixture compositions, such as variations in nodule size, concentration, and density, as well as the effect of geometry on flow assurance, valuable insights can be gained. These insights can improve the pump's reliability, optimize its design, and enhance its effectiveness for DSM operations.

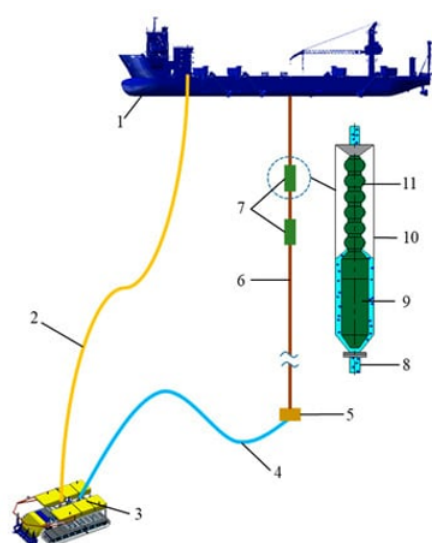


Figure 1.4: Overview of System: 1- Production Support Vessel, 2- Umbilical cable, 3- Nodule collector, 4- Jumper hose, 5- Riser base, 6- Riser, 7- Multi-stage centrifugal pump, 8- Riser, 9- Motor, 10- Pump housing, 11- Pump stage. [17]

1.3. Research Objectives

The objective of this study is:

- *To identify and analyze the key design vulnerabilities of multi-stage centrifugal pumps that could lead to flow assurance issues in DSM operations, focusing on the interplay between design factors and operational variables under conditions prone to clogging or reduced performance.*

1.4. Research Questions

To achieve the objective, the following research questions have been formulated:

1. *What are the potential benefits and drawbacks of using multi-stage centrifugal pump versus other types of pumps in terms of internal flow properties in deep-sea nodule collecting systems?*
2. *What are the critical physical phenomena and engineering limits in multi-stage centrifugal pump designs that affect the flow assurance for the hydraulic transport of particles of various diameters in DSM applications?*
3. *How do operational variables, such as mixture concentration and particle size distribution, influence the flow assurance and performance of multi-stage centrifugal pumps in DSM applications?*
4. *How can the reflux and flow assurance be effectively investigated in an experimental setup for multi-stage centrifugal pumps?*

1.5. Research Approach

This research is divided into a theoretical and an experimental phase, each tailored to systematically address the research objective.

In the theoretical phase, a comprehensive literature review is conducted to develop an understanding of the multi-stage centrifugal pump within the context of DSM operations. This stage aims to answer the first research question by exploring the potential benefits and drawbacks of using multi-stage centrifugal pumps compared to other pump types, as discussed in Section 2.2.

The second part of the theoretical phase focuses on identifying key design aspects and internal flow dynamics of the pump that could contribute to flow assurance issues. This aspect is detailed in Section 2.4, addressing the second and third research questions. Particular attention is given to the interaction between the pump's geometry and operational variables, such as mixture concentration and particle size distribution. The theoretical phase concludes with a conclusion in section 2.5.

The findings from the theoretical phase are analyzed in the experimental phase. A test setup is designed to replicate the critical conditions identified during the literature review under controlled conditions. The setup is specifically designed to evaluate the effects of various operational variables. Details of the setup and the testing program are discussed in Chapter 3.

A: Fallpipe Experiment

The experimental phase begins with a simple fallpipe experiment in Chapter 4.

- **Series A1: Terminal Velocity Tests**

This series (Section 4.2) determines the terminal settling velocity of single solids ranging from 5 mm to 30 mm in size.

- **Series A2: Settling behavior**

In this series (Section 4.3), The settling behavior of solid batches with varying solid sizes, densities, initial batch heights, and concentrations.

B: Pump Without Blades Experiment

The second experiment examines the pump without blades in Chapter 5. This chapter investigates the spacing within the pump and its relationship to solid size.

- **Series B1: Test Matrix** Identifies key variables affecting flow assurance in the pump through systematic testing (Section 5.2).

- **Series B2: In-Depth Analysis** Investigates the specific impact of the blockage-inducing variables identified in Series B1 (Section 5.3).

- **Series B3: Shortened Fallpipe** Analyzes the effect of higher arrival concentrations by reducing the fallpipe length (Section 5.4).

C: Pump With Blades Experiment

The final experiment investigates the pump with blades in Chapter 6. Two complete stages, including blades, are analyzed to create a comprehensive model. The primary research goal is to evaluate the impact on reflux.

- **Series C1: Initial Evaluation** Focuses on isolating individual variables affecting reflux performance in the pump with blades (Section 6.2).

- **Series C2: Performance Analysis** Investigates the main factors influencing flow assurance and blockage formation (Section 6.3).

- **Series C3: Adjusted Blades** Implements and tests design modifications to address identified flow assurance issues (Section 6.4).

Chapter 7 discusses findings and observations from the research that could have broader implications in real-world scenarios, especially in areas that received less attention in this study.

Finally, the conclusions and recommendations derived from the theoretical and experimental stages are summarized in Chapter 8.

2

Literature

2.1. Introduction

This chapter presents the literature review. Section 2.2 describes the working principle of the vertical hydraulic transport system, including the associated flow regimes and the various driving forces for hydraulic lifting. In Section 2.3, the pump selected for this research is analyzed in greater detail. Section 2.4 examines the challenges related to flow assurance. Finally, Section 2.5 summarizes the conclusions and addresses the research questions based on the findings of the literature review.

2.2. Vertical Hydraulic Transport

This section focuses on the Vertical Hydraulic Transport system. The first part explores hydraulic lifting and the various flow regimes that occur during the process. The second part examines different driving forces necessary for hydraulic lifting, including airlift, centrifugal volute pumps, positive displacement pumps, and multi-stage centrifugal pumps.

2.2.1. Hydraulic Lifting

During standard operation, the nodules are first transported through the jumper hose to the riser base, which connects the riser and the jumper. From the riser base, the nodules are then transported via the riser to the production support vessel, as illustrated in Figure 2.1. Throughout the various stages of the system, differing conditions present unique flow characteristics that must be carefully controlled to ensure optimal performance and reliability of the overall system.

In the event of system failure, a valve at the riser base opens, allowing the nodules to exit the system here and preventing blockages in the jumper.

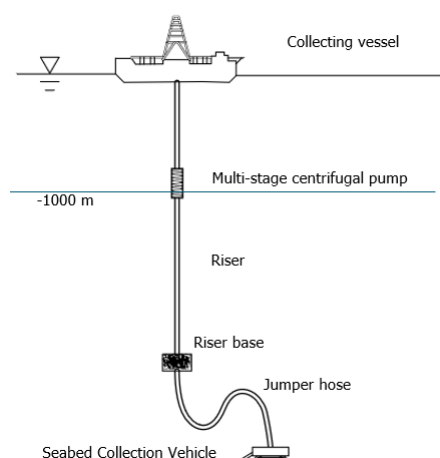


Figure 2.1: Overview hydraulic lifting [9]

The jumper's s-shape design leads to a stratified slurry, where nodules and sediments slide along the inclined and horizontal sections, creating a shear layer above this sliding bed [57, 19]. The formation of density waves within the jumper will be further elaborated in Section 2.4.2.

For vertical transport in the riser, research has been conducted into the different flow regimes and how hydraulic lifting of manganese nodules works in the riser system. [21, 38] These studies also provide insights into various mechanisms that can potentially lead to blockages in the riser. Van Wijk [59] states that one of the important mechanisms is the merging and overtaking process of batches with different transport velocities. In his research, he also examines the formation of wall-attached clusters as seen for flat particles and the occurrence of density waves that could develop into solid plugs.

The VHS under consideration for this research will feature a riser with an inner diameter of 300 mm, designed to transport nodules with a median particle diameter (d_{50}) of 30 mm. The nodules have a density of 2000 kg/m³, while the mixture density is designed at 1200 kg/m³.

Terminal Settling Velocity and Hindered Settling

The different flow regimes discussed in the previous section depend on terminal settling velocity and hindered settling. Using the hindered settling velocity, the particle Reynolds number can be calculated. Section 2.4.3 explains the relevance of this calculation, and in Appendix.A, the Python script for this calculation can be found.

Terminal Settling Velocity

The terminal settling velocity (v_t) of a particle is achieved when the forces of gravity, buoyancy, and drag are in balance. Gravity (F_g) acts downward, buoyancy (F_b) opposes it due to fluid displacement, and drag (F_d) resists the motion. The drag force depends on the fluid density, the particle's surface area (A), and the drag coefficient (C_D).

The forces can be expressed as:

$$\sum F = F_g + F_b + F_d$$

The equation for the terminal settling velocity is:

$$v_t = \sqrt{\frac{4g(\rho_s - \rho_f)d}{3\rho_f C_D}}$$

Where:

- v_t = Terminal Settling Velocity of a single particle
- g = acceleration due to gravity
- ρ_s = density of the solid particle
- ρ_f = density of the fluid
- d = diameter of the particle
- C_D = drag coefficient

Hindered settling

The hindered settling velocity (v_{th}) is described by the following formula according to Richardson and Zaki:

$$v_{th} = v_t(1 - \phi)^n \cdot 10^{-\frac{d}{D}}$$

Where:

- v_{th} = hindered settling velocity of the particle
- v_t = terminal settling velocity in an infinite fluid
- ϕ = volume fraction of the solid (solid fraction)
- n = empirical exponent, depending on the Reynolds number and particle shape
- d = particle diameter
- D = pipe or container diameter

The hindered settling velocity (v_{th}) is determined by two factors. The first factor is the terminal settling velocity (v_t), which is the velocity a particle reaches when settling in an infinite fluid without interference from other particles or boundaries. The second factor is a correction term, $(1 - \phi)^n \cdot 10^{-\frac{d}{D}}$, which adjusts for the effects of particle concentration and pipe size. Here ϕ represents the volume fraction of particles. The ratio $\frac{d}{D}$ accounts for the influence of particle interactions and wall effects, especially when the particle diameter is large relative to the pipe diameter[59].

The exponent n is a function of the particle Reynolds number (Re_p). The original equations for n as provided by Richardson and Zaki (1954) are as follows [59]:

$$\begin{aligned} n &= 4.65, & \text{for } Re_p \leq 0.2, \\ n &= 4.35 \cdot Re_p^{-0.03}, & \text{for } 0.2 < Re_p \leq 1, \\ n &= 4.45 \cdot Re_p^{-0.1}, & \text{for } 1 < Re_p \leq 200, \\ n &= 2.36, & \text{for } Re_p > 200. \end{aligned}$$

2.2.2. Pumping Mechanisms

As mentioned in Section 1.1, this thesis focuses exclusively on systems that employ a riser. This system has different configurations, each with a unique pumping source. These different configurations have been tested in various experiments. The following section will discuss the multi-stage centrifugal, airlift, positive displacement, and centrifugal volute pumps. These different pumps are discussed to provide a clear understanding of the advantages and disadvantages of a multi-stage centrifugal pump. Various companies and governments conducted tests for these configurations, as is seen in Table 2.1

Year	Company/Organization	System Tested	Results/Notes
1978	Ocean Mining Inc. (OMI)	Static riser with two 6-stage centrifugal pumps	Demonstrated feasibility of multi-stage centrifugal pumps [43]
2010	India	Positive displacement pump in Arabian Sea	Successful lifting trial [14]
2023	The Metals Company (TMC)	Riser with airlift system	Successfully lifted 3000 tons of nodules [56]
N/A	Dredging Industry	Centrifugal volute pumps	Early trials show potential for deep-sea mining

Table 2.1: Overview of some Riser System Tests and Results in Deep-Sea Mining

Centrifugal Pump Volute type Centrifugal pumps consist of two main parts: the rotating assembly, which includes a shaft fitted with an impeller that has blades to move fluid effectively, and the stationary assembly, which consists of a casing that houses the impeller and includes essential seals and bearings to support the shaft and keep the fluid contained [44, 49].

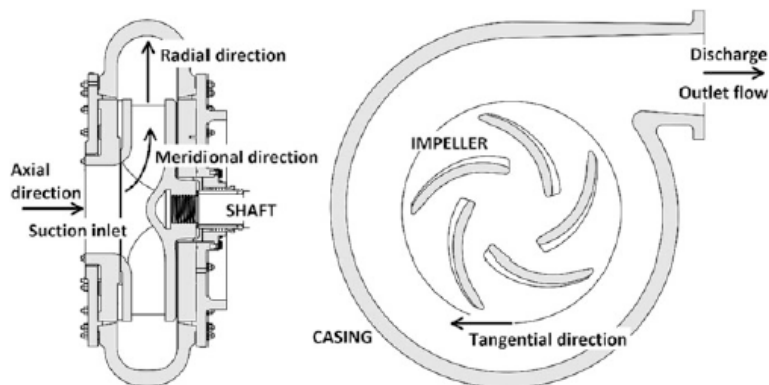


Figure 2.2: Sections of a representative slurry pump [33]

In a centrifugal pump, fluid enters the pump impeller along or near the rotating axis. It is accelerated by the impeller, flowing radially outward into the volute, where the velocity is transformed into pressure

primarily due to the centrifugal force. The rotating impeller transfers kinetic energy to the fluid, which is then converted to pressure energy as the fluid leaves the impeller and decelerates in the expanding volute, designed to efficiently convert velocity into pressure by providing a gradually expanding flow path [33]. When designing a centrifugal pump, the focus is on carefully selecting the appropriate sizes for the impeller and casing to achieve the desired performance. The impeller diameter, shape, and the number of blades directly influence how fluid is accelerated, while the specific volute design determines how effectively velocity is converted into pressure. For example, a larger impeller not only increases the pressure generated but also interacts with the volute design to ensure efficient energy conversion. A well-designed volute further minimizes energy losses by enabling smooth deceleration of the fluid, making these design elements critical for tailoring the pump to specific operational requirements and overcoming physical or hydraulic limitations [49].

Centrifugal pumps face additional challenges in dredging operations, where the handling of slurry is common. These include processing large solid particles, ensuring the durability of the rotating assembly due to the heavier slurry compared to water, and reinforcing parts of the pump to resist wear and tear. This approach helps ensure that the pump performs efficiently and lasts longer in demanding dredging conditions, making these properties and knowledge applicable in DSM applications.

However, there are also some downsides to using centrifugal pumps in DSM applications. The significant pressure losses over the vertical length of the riser necessitate the installation of multiple pumps at various depths to maintain a sufficiently high flow rate, ensuring the pump can generate enough pressure. While this staged approach provides a more even distribution of pressure and flow throughout the system, a major drawback is that any failure in one of the pumps requires retrieving the entire riser system to the surface for maintenance or repairs. Additionally, the flow enters the pump at a different angle than it exits, making integration into the riser more complex.

Positive Displacement Pump

Positive displacement (PD) pumps move a fixed amount of fluid in discrete volume increments by trapping a set volume of fluid and forcing (displacing) that fluid into the discharge pipe. In this way, the speed of the pump determines the discharge rate of the liquid pumped [51]. PD pumps can be rotary, such as gear or lobe pumps, or reciprocating, such as diaphragm or piston pumps. The mechanism involves creating an underpressure at the pump inlet that draws fluid into the pump, sealing off the inlet, and displacing the fluid out of the discharge. This type of pumping action makes them especially effective against high resistance and for handling viscous fluids or fluids containing suspended solids [45]. However, using positive displacement (PD) pumps in deep-sea mining comes with certain challenges, particularly the need for an external actuator to drive the pump. This actuator is essential for converting energy into the mechanical motion required to operate the pump. The actuator must be housed onboard the mining vessel, adding to the system's complexity. This setup not only requires additional space and infrastructure but also increases maintenance demands [27]. Additionally, handling large solids in PD pumps can present problems, as these solids may cause blockages or damage to the valves. An example of a positive displacement pump is shown in Fig. 2.3.



Figure 2.3: Positive Displacement Pump [27]

Multi-stage Centrifugal Pump Multi-stage centrifugal pumps consist of multiple impellers arranged in series on a single shaft, enclosed within a sealed, oil or water-filled housing. Each stage consists of an impeller and a diffuser. A diffuser is designed to convert the high velocity of the fluid leaving the impeller into pressure by slowing down the fluid in a series of stationary vanes. As the velocity decreases, the pressure increases, allowing the pump to raise the pressure progressively. Multiple stages allow these pumps to achieve higher pressures, which is essential for lifting fluids containing solids from deep wells or underwater mining applications.

The motor that drives the multiple impellers is integrated into the same axis as the riser. This inline configuration of the motor with the riser reduces its profile, minimizing exposure to external forces such as water currents [43]. In deep-sea mining applications, a single multi-stage centrifugal pump is often insufficient to compensate for the pressure losses over the full length of the riser. Therefore, multiple pumps, typically three to four, are installed in series directly behind one another within the riser. Figure 2.4 shows how this setup appears within a riser.

The term "multi-stage centrifugal pump" can be a point of debate. Some may argue that because the fluid mixture exits the pump in an axial direction, it should be classified as an axial flow pump. However, in this thesis, the term "centrifugal" has been chosen because, within each stage of the pump, the fluid is primarily accelerated radially by the impeller before being redirected axially to enter the next stage. This terminology is widely used in industry and scientific literature on this topic [32, 58].

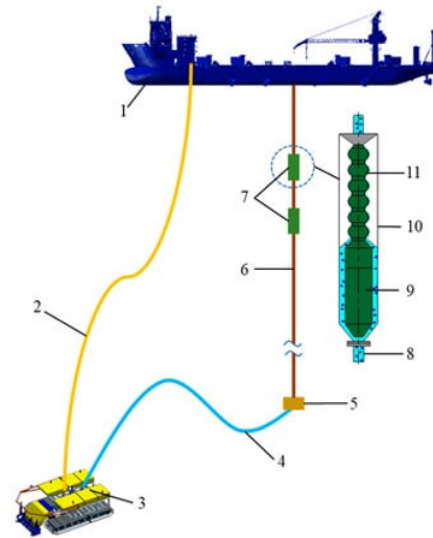


Figure 2.4: Overview of System: 1- Production Vessel, 2- Umbilical cable, 3- Nodule collector, 4- Jumper hose, 5- Riser base, 6- Riser, 7- Multi-stage centrifugal pump, 8- Riser, 9- Motor, 10- Pump housing, 11- Pump stage. [17]

Airlift An airlift pump operates on the principle of reducing fluid density inside a riser by injecting compressed air at a specific depth. This injection creates an air-water mixture with a lower density compared to the surrounding liquid. The difference in hydrostatic pressure between the denser surrounding liquid and the less dense mixture inside the riser drives the fluid upwards through the riser. A schematic overview of this concept is shown in Fig. 2.5. The effectiveness of an airlift pump depends on the depth at which the air is injected and the airflow rate, as these factors determine the lifting capability and efficiency of the pump [30]. The capacity and energy consumption depend on the main factors: pipe diameter, inlet depth of compressed air, and particle size [14].

A significant advantage of using this type of pump in deep-sea mining operations is that no pump is placed in the riser. As a result, the riser is free from obstructions, reducing the risk of blockages and abrasion issues that typically occur with mechanical pumps [30]. Additionally, the airlift system benefits from a minimal number of moving components subsea, which enhances its reliability. Furthermore, the absence of hydraulic fluids or lubricants and reduced subsea noise due to compressors being located on the deck lead to fewer environmental risks. These factors make airlift pumps an interesting option for deep-sea mining.

The most significant disadvantages of the airlift system are its energy-intensive nature, with an efficiency of approximately 20%, which is significantly lower than that of hydraulic lifting systems, which exceed 50% [6]. Additionally, maintaining stable and continuous operation is challenging due to the inability to directly control the liquid and solid outputs [18].

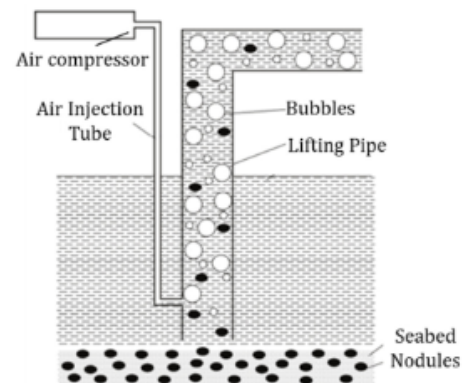


Figure 2.5: Schematic diagram of airlifting system [14]

Selection of pump The selection of an appropriate pumping mechanism is crucial for ensuring reliable operation in deep-sea mining systems. Various options, including airlift pumps, positive displacement pumps, and centrifugal pumps, each present unique strengths and limitations. For this research, a multi-stage centrifugal pump was chosen due to its promising potential to address the specific challenges of deep-sea mining.

An inline configuration, as employed in multi-stage centrifugal pumps, offers significant advantages. Unlike external configurations, it is less affected by external flow disturbances. Furthermore, multi-stage centrifugal pumps are highly efficient in generating the high pressures required to lift mixtures from great depths. In comparison, airlift systems are energy-intensive and less controllable, while positive displacement pumps face difficulties in handling large solids. This makes the multi-stage centrifugal pump a balanced and effective solution.

However, a thorough evaluation of pumping mechanisms necessitates a deeper understanding of the performance of multi-stage centrifugal pumps, particularly their ability to maintain consistent flow and prevent blockages when handling solids. These knowledge gaps underline the need for further research. This thesis seeks to address these uncertainties, evaluate the feasibility, and optimize the design of multi-stage centrifugal pumps as a reliable and efficient driving force for deep-sea mining operations.

2.3. Multi-stage Centrifugal Pump

The previous section provided an overview of the various pump types. Given the research objective, the following section will present an in-depth analysis of the multi-stage centrifugal pump.

Overview

In Fig. 2.6, the structure of a multi-stage centrifugal pump is shown. The mixture from the previous stage enters the impeller axially at a relatively low velocity at point eleven but quickly accelerates due to the high rotational speed of the impeller's blades. This results in the torque provided by the driving shaft being converted into kinetic energy by the blades. The rapidly moving mixture, now discharged at a horizontal angle, flows into the blade channels of the diffuser, which is the stationary component of the pump. Here, the kinetic energy is transformed into pressure energy. Consequently, the mixture exits the pump stage at the diffuser's discharge at a higher pressure than it was at the impeller's inlet, thus elevating the overall flow pressure. As the discharge from one stage feeds directly into the intake of the next stage, this cycle repeats, gradually increasing the pressure of the pumped mixture [55, 42].

The energy transformations within the centrifugal pump involve the conversion of mechanical energy from the prime mover into fluid energy, primarily as pressure energy. As the fluid passes through the impeller, its velocity (and therefore its kinetic energy) increases. In the diffuser, this kinetic energy is partially converted into pressure energy, leading to an overall increase in the fluid's pressure. Therefore, the energy input from the prime mover is effectively transformed into an increase in fluid pressure, while the pump ensures a steady flow rate [55].

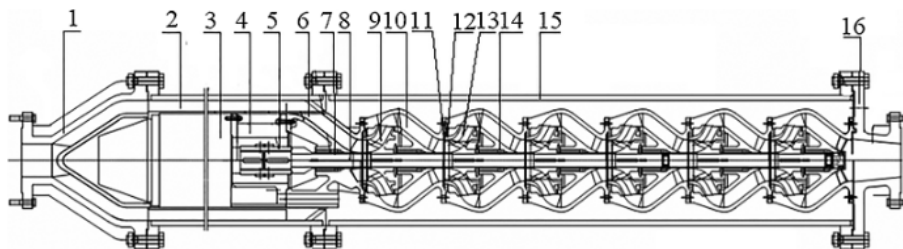


Figure 2.6: Over-all structure of six-stage lifting motor pump. 1-Inlet flange, 2- Motor barrel, 3-Motor, 4 Connection section, 5- Coupling, 6- Suction housing, 7-Slide bearing, 8- Pump shaft, 9- Impeller 1 , 10- Space guide, 11- Pump body seal ring, 12- Impeller port ring, 13 Impeller 2, 14- Damper disc, 15 - Pump cylinder body, 16 - Outlet flange. [23]

Hydraulic Specification The geometry and design of the pump's interior depend on the required head, concentration, and flow rate. For the highest possible production, a high concentration is desirable. However, the system must handle this concentration without affecting the flow assurance.

$$C_v = \frac{\rho_{\text{mix}} - \rho}{\rho_s - \rho} \quad (2.1)$$

The system needs a specific head to overcome the resistance. The head produced by the pump is mainly determined by the shape of the pump bowl, making it an essential factor in the hydraulic design.

Impeller and Diffuser Design

For flow assurance within the multi-stage pump, it is crucial to look at the different parts of the pump. The impeller is the driving force of a multi-stage pump, playing an important role in converting mechanical energy into fluid energy. Its design significantly impacts the pump's performance, especially when handling fluids that carry solids. Key parameters in impeller design include the blade angles, number of blades, flow path optimization, and entry and exit widths.

Number of Blades, Inlet and Outlet Widths The number of blades, Z , affects the flow pattern and the hydraulic efficiency. A higher number of blades generally reduces the relative velocity and the incidence angle, minimizing hydraulic losses. However, too many blades can increase friction and blockage especially in fluids with particles. The increase in friction occurs due to a larger wetted surface area [42, 23]. The impeller and diffuser passages of a multi-stage centrifugal pump used in deep-sea applications must be larger than those in standard applications to ensure the safe and unobstructed passage of solids [23].

Gulich [36] proposes that the spaces in the pump must have a minimum width of dk , where $dk > d_{\text{solid}}$. The inlet diameter of the impeller (d_1) and the outlet width of the impeller (b_2) must all satisfy $dk > d_{\text{solid}}$. An overview of the spaces within the impeller can be seen in Figure 2.7.

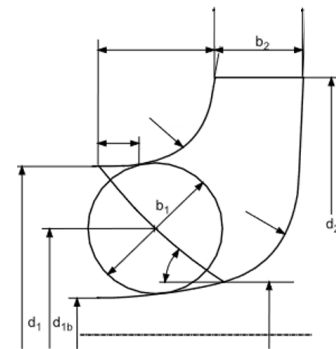


Figure 2.7: Design parameters for the impeller [36]

This requirement is supported by experimental findings from OMI [43]. In their tests, the pump was designed to handle nodules with a maximum diameter of 60 mm. To prevent blockages, the minimum width of the pump spaces was set to 75 mm, approximately 125% of the maximum nodule size. This design proved effective, as no blockages occurred during the tests. Even when the pump was turned off, nodules flowed back down through the pump without issue, demonstrating the importance of maintaining sufficient clearance within the impeller design.

Blade Angles, Inlet, and Outlet Blade angles are critical in determining the flow dynamics within the pump. The inlet blade angle, β_1 , and the outlet blade angle, β_2 , are designed to ensure smooth entry and exit of the fluid, minimizing shock losses and optimizing energy transfer. The inlet blade angle, β_1 , is designed to align the fluid flow direction with the rotational speed of the blades, as can be seen in Fig. 2.8. This alignment helps to minimize energy loss due to turbulence as the fluid enters the impeller [42]. The outlet blade angle, β_2 , is essential for ensuring that the pump delivers the intended head. This angle helps determine the efficiency of energy transfer as the fluid exits the impeller. Properly setting β_2 minimizes energy loss due to flow deviations near the exit, ensuring more effective energy transfer from the blades to the fluid [33, 42]. As C. Han [37] found in his research on the impact of outlet blade angle, optimizing this angle can greatly improve the efficiency of submersible pumps. It reduces power losses and boosts performance under different flow conditions.

Blade Thickness Particles in the fluid can lead to blockage and clogging, especially in narrow passages of the impeller and diffuser. This can reduce the pump's efficiency and increase wear. Solid particles cause wear and erosion, particularly at the leading edges of the blades and in high-velocity regions. Materials with high wear resistance and coatings can mitigate these effects. Increasing the thickness of the blades and other components that frequently come into contact with the nodules can extend the lifespan of these parts [36].

Impeller Torque, Power, Head

To understand how the power of the shaft is transferred to the impeller torque and fluid angular momentum in centrifugal pumps through Newton's second law for moments of forces and Euler's Pump Equation, this section provides a breakdown of the concepts and their application to centrifugal pumps.

Impeller Speed The nodules should be in contact with the impellers as little as possible. Each impact can break the nodules into smaller pieces and damage the impellers. The consequence of the nodules breaking up is that these smaller pieces and the debris released are harder to separate from the mixture. This can result in lower overall production. Damage to the impeller must always be prevented. A lower impeller speed creates less collision between the impeller and the nodules.

Velocity Diagram Fluid velocities at both the inlet and outlet of an impeller significantly influence the performance and efficiency of centrifugal pumps. When considering the fluid movement along the blades of a rotating impeller (with an angular velocity Ω), the relative velocity W is observed within the rotating frame of reference of the impeller. To obtain the absolute velocity V , one must vectorially combine the relative velocity W with the impeller blade speed $U = \Omega r$, as depicted in the impeller velocity diagrams in Figure 2.8 [42].

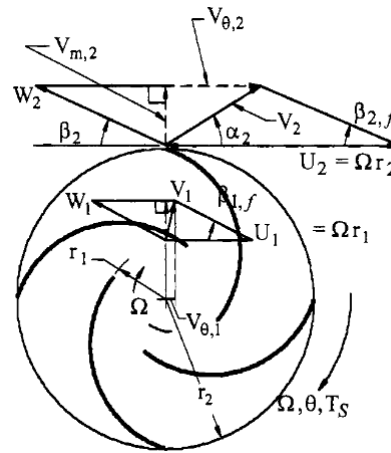


Figure 2.8: Impeller velocity diagrams (1 = inlet, 2 = outlet) [42]

Newton's Second Law for Moments of Forces and Euler's Pump Equation

Newton's second law for moments of force (torques) states that the sum of external torques acting on a system equals the rate of change of angular momentum of the system. This principle forms the foundation for analyzing rotational systems, including fluid dynamics within pumps. Euler's Pump Equation extends this understanding to centrifugal pumps by relating the torque exerted by the impeller to the change in angular momentum of the fluid.

In the context of deep-sea mining, the application of Euler's Pump Equation highlights critical design considerations that improve pump performance and reliability. Specifically, the use of a low number of blades and reduced rotational speed (RPM) offers significant advantages. Fewer blades create larger flow passages, facilitating the smooth passage of large solids and minimizing the risk of blockages. Additionally, operating at a lower RPM reduces mechanical stress on the solids, preventing them from being damaged or fragmented.

However, to maintain the desired hydraulic performance under these constraints, an increased impeller radius r is necessary. A larger radius not only compensates for the reduced blade count and RPM but also aligns with the need for wider flow passages, enhancing the pump's capability to handle large solids effectively. This combination of design strategies—fewer blades, lower RPM, and a larger radius makes multi-stage centrifugal pumps highly suitable for deep-sea mining applications, where flow assurance and reliability are paramount [42].

Description of Pressure Calculations In this section, the required pump pressure is analyzed to ensure that the system operates reliably. The total pressure drop in the riser ($\Delta P_{\text{tot}} = 94.63 \text{ bar}$) is the pressure the pump must generate to transport the mixture to the surface. This includes the hydrostatic pressure due to the mixture density, the deck height, and the frictional losses in the riser pipeline. The detailed calculations for ΔP_{tot} can be found in Appendix B.

To avoid creating a vacuum or underpressure within the riser, the pump must be positioned at a depth where the external hydrostatic pressure exceeds the pressure it needs to generate. At a depth of $H_{\text{pump}} = 1000 \text{ m}$, the external hydrostatic pressure is calculated as:

$$P_{\text{outside}} = \rho_{\text{water}} \cdot g \cdot H_{\text{pump}} = 1025 \cdot 9.81 \cdot 1000 = 100.55 \text{ bar.}$$

The difference between the external hydrostatic pressure and the total pressure drop is:

$$P_{\text{margin}} = P_{\text{outside}} - \Delta P_{\text{tot}} = 100.55 - 94.63 = 5.92 \text{ bar.}$$

This margin of 5.92 bar ensures that the pump can operate without the risk of underpressure, even with fluctuations in the mixture's density. Positioning the pump at this depth provides sufficient buffer to maintain stable operation and prevent system failure.

Conclusion

Designing impellers and diffusers for multi-stage pumps in deep-sea mining requires optimizing key factors such as blade angles, the number of blades, flow path geometry, and entry and exit widths. These design choices are essential for handling mixtures, minimizing blockages and wear, and ensuring reliable performance under extreme conditions.

Combining the principles outlined in sections 2.3 clarifies the relationship between the required pump pressure and design parameters. The total pressure drop (ΔP_{tot}) in the riser is approximately 94.63 bar, which the pump must generate to transport the mixture to the surface.

With this value of H_{total} , the appropriate pump design can be determined using Euler's Pump Equation. The torque and power imparted to the fluid, governed by the impeller's geometry and operating parameters (such as r , V_{θ} , and ω), can be optimized to generate the required head. This involves selecting the correct number of stages, impeller blade design, and RPM necessary to achieve the total head while maintaining reliable operation under deep-sea conditions. By adjusting these design factors, such as the number of blades, RPM, and impeller radius, the multi-stage centrifugal pump can be designed to provide the necessary head to overcome the system's pressure drop.

2.4. Particle Dynamics in Multi-Stage Centrifugal Pumps

This section examines flow assurance challenges, focusing on regular operation, reflux, and pump design, highlighting key factors that impact performance.

2.4.1. Flow Assurance in Pumps

It is essential to keep the system's downtime as low as possible. One of the main potential issues for this system is flow assurance in the multi-stage pump. Problems can occur in various ways during the upward transport, but they are particularly problematic during reflux. Reflux occurs when the flow of the mixture inside the riser system reverses direction or stagnates, causing the material to flow back down toward the seabed instead of continuing upward to the mining vessel. This can happen due to a sudden drop in pressure, a pump failure, or other disruptions in the flow system. Reflux can lead to blockages, increased wear on the pump components, and potential damage to the riser system, ultimately resulting in increased downtime and reduced operational efficiency.

Normal Operation In 1978, OMI was the first to conduct a fully integrated nodule collection test with a multi-stage centrifugal pump. They successfully transported 800 tons of nodules to the water surface [43]. However, they estimated that a 3 to 5 times higher production rate would be necessary for the operation to become commercially viable.

Effective control of slurry transport is essential to ensure consistent flow. Studies using CFD-DEM simulations have shown particle agglomeration occurring in various cases and at different locations. L. Deng demonstrated that upon reaching the pump, due to the slower velocity of the fluid in the pipeline, the first impeller creates a rotating backflow. Particles rotate close to the pipe wall before the first impeller stage due to the centrifugal force, potentially causing particle agglomeration. Increasing flow rates can reduce this risk[32]. In his later research, L. Deng proposed the placement of splitters at the lower inlet of the pump, as shown in Figure 2.9a, to address the accumulation problem and enhance safety. Figure 2.9b provides a closer view of the splitter plate [31].

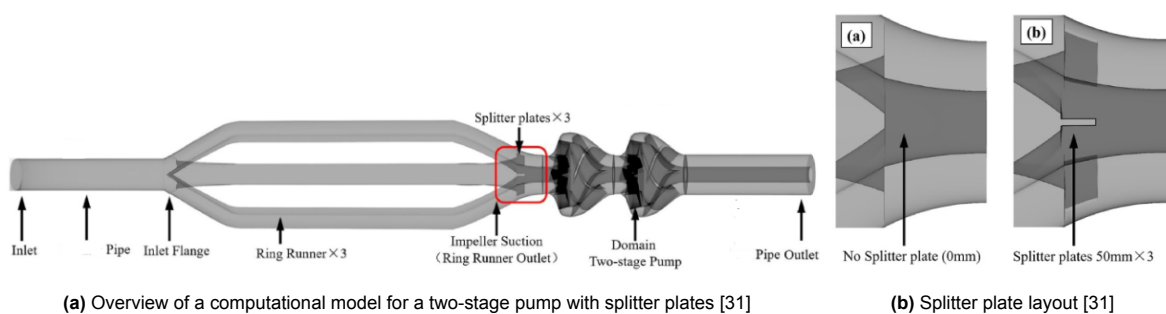


Figure 2.9: (a) Computational model overview for a two-stage pump, and (b) splitter plate layout.

CFD studies also revealed critical insight into the local backflow along the diffuser created by the balance holes. Balance holes are small openings in the impeller that allow fluid to pass from the high-pressure side to the low-pressure side, helping to reduce axial thrust on the impeller. However, these holes can also lead to unwanted flow paths, contributing to backflow along the diffuser [24]. These studies highlight that flow restrictions often occur at the diffuser-impeller interface due to reverse flow structures. These flows can impede the upward transport of the solids, making it essential to optimize these backflows [20, 32]. Large, non-spherical particles can potentially pose a risk for flow assurance within the pump. Numerical studies combining CFD and DEM techniques indicate that particles with lower sphericity experience higher drag forces, leading to blockages [22].

Understanding particle movement and interactions within the pump enables better design strategies to prevent blockages and ensure steady upward flow. Innovations in multi-stage pump designs, like widening the flow passage, enhance performance with coarse particles and maintain smooth, uninterrupted flow [22, 23, 32, 58].

Reflux When the pump stops working, regardless of the cause, a reflux of solids will occur. When this reflux happens, the solid particles should be able to pass through the pump without any obstruction. In various experiments, this reflux caused blockages inside the pump. "Changsha Mining and Metallurgical Institute Co., Ltd" conducted tests with a two-stage lifting pump, and no flow issues emerged during the operation. However, blockages formed in the internal flow channel, which refers to the passages within the pump where the fluid and solid particles move during operation when the pump was turned off, and reflux occurred [13]. Not all experiments have resulted in clogging due to reflux. For example, shutting down the pumps during the scale test by OMI did not lead to any clogging [43]. The occurrence of these reflux-induced blockages stimulated Hu [13] to study this phenomenon using CFD-DEM before conducting further experiments. The CFD-DEM analysis by Hu provides insights into how and where blockages occur during reflux. The analysis identifies two critical points in the flow field: when the pipeline transitions into the pump and when passing from the first stage to the second stage (see Figure 2.10). Yuanwen describes a third critical point, the junction of the impeller with the diffuser (also shown in Figure 2.10) [10]. Particle accumulation behavior was observed at these points, which is a crucial factor limiting the reflux capacity of the pump. The numerical simulation of the reflux provided several key insights. Both Hu and Yuanwen validated their simulations with experiments.

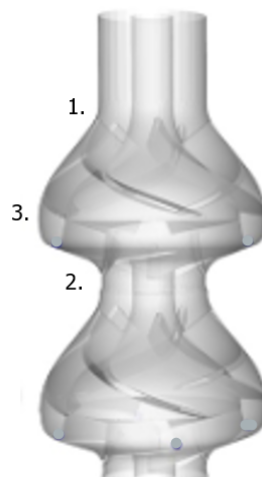


Figure 2.10: 1. Transition of the pipeline into the pump. 2. Transition from the first to the second stage. 3. Junction between the impeller and the diffuser. [13]

Particle size distribution significantly impacts blockage severity, with a polydisperse particle distribution causing more severe blockages than a narrow particle size distribution or monodisperse particles. Consequently, effective backflow is possible with smaller particle sizes, while larger particles tend to cause severe blockages. Even though the size of these large particles was not an issue during the regular operation of the pump [13, 10]. The mechanism of blockage formation involves large particles restricting each other's movement within the flow channel, with smaller particles filling the gaps and intensifying the blockage [13], or small particles agglomerating into larger ones that obstruct the channel [10].

When studying the pressure on the guide vanes from two groups of particles, it was found that the collisions of the group with larger-diameter particles on the guide vane channels are much more significant than those of the group with smaller-diameter particles. As seen in fig. 2.11 and fig. 2.12, this higher pressure is caused by the larger-diameter particles colliding with each other more frequently, exerting greater force on the vane channels. Additionally, because the larger particles are spaced closer together due to their size, there is less room between them, which increases the risk of clogging [13]. It is important to notice that this pump has more blades due to the particles being crushed in this configuration.

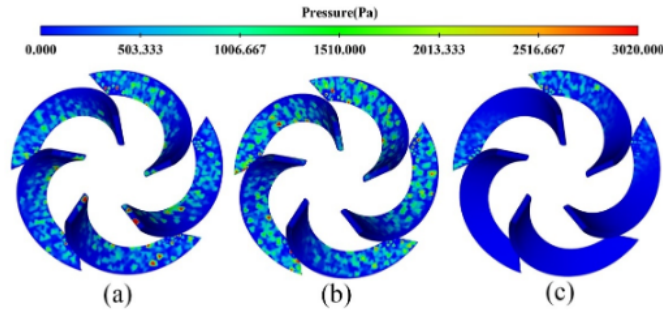


Figure 2.11: Pressure cloud on the guide vane after being collided with 10–20 mm particles: (a) pressure cloud graph at 2 s; (b) pressure cloud graph at 10 s; (c) pressure cloud graph at 15s [13]

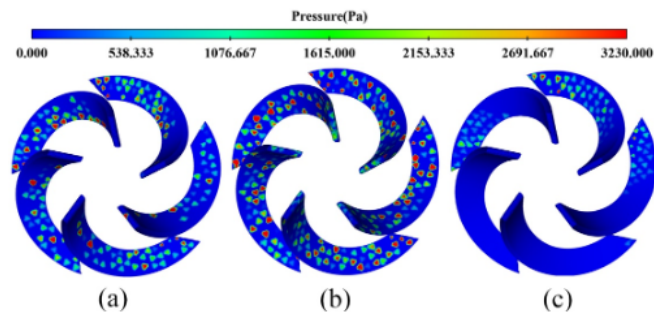


Figure 2.12: Pressure cloud on the guide vane after being collided with 20–30 mm particles: (a) pressure cloud graph at 2 s; (b) pressure cloud graph at 10 s; (c) pressure cloud graph at 15s [13]

Geometry When looking at the 2D model of a cross-section of a bowl from the SMP, the different flow patterns become clear. Figure 2.13 shows a sketch of one of the pump bowls.

When looking downstream, the solids first fall through a vertical straight pipe with a cross-sectional area of A . Upon arriving at the first pump, the total cross-sectional area of the pipe gradually decreases to area B due to the pump shaft. This reduction means the same cross-section of solids must pass through a smaller cross-section of vertical pipe. Upon reaching the first impeller, the straight pipe converges into a bend, where the total cross-sectional area increases due to the larger radial distance from the axis while maintaining the same spacing. Arriving at point D , the ratio of the pipe’s cross-sectional area to the solids is the largest. From D , the flow returns to C and then to B . This sequence repeats through each stage of the pump.

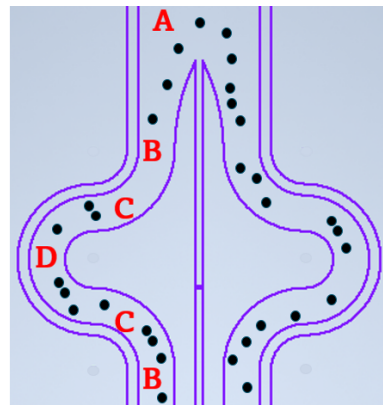


Figure 2.13: 2D cross-sectional visualization of pump with solids highlighted in black to illustrate internal flow channels.

2.4.2. Particle Transport

The design of pump-pipeline systems for transporting slurries has traditionally been based on steady-state principles. This approach assumes that the particle quantity and their transport speed remain constant over time and in their location within the pipeline. This allows designers to evaluate maximum load scenarios of the system [38].

E. Hoog classifies three different types of density waves that can form in systems with both vertical and horizontal pipelines:

- **Erosion-driven density waves:** These arise from the erosion of particle deposits when mixture velocities are too low.
- **Sliding bed-driven density waves:** These occur when particles accumulate and form a sliding bed.
- **Transient accumulation waves:** These form in pipeline systems with horizontal and vertical sections due to significant differences in particle velocities between these sections.

The first two types occur in horizontal pipelines, while the third occurs in a combination of horizontal and vertical sections.

The third type mainly applies to the jumper hose or the transport system. The formation of density waves in the jumper hose can impact the flow assurance of the multi-stage centrifugal pump. The question then arises as to how the multi-stage centrifugal pump processes these density waves and what influence the pump has on them. Specifically, whether the density waves are amplified or whether the pump helps create a more uniform flow as they pass through it. This effect is interesting when considering reflux, as it determines the nature of the mixture above the multi-stage centrifugal pump. It is important to understand what the pump will likely receive during reflux, whether it will be density waves or a more evenly distributed mixture.

Hoog's third type may also be applicable for examining the formation of density waves in pumps, as described in Section 2.4.1, where vertical and declining sections alternate in the pump housings.

Typical input parameters for designing these systems include particle concentration, particle size and density, pipe roughness, diameter, and length. Considering a 2D model of a cross-section of a bowl from the multi-stage centrifugal pump, various flow patterns become evident:

1. **Vertical Pipe to the Pump:** Solids first fall through a vertical straight pipe with a cross-sectional area A .
2. **Reduction of Cross-Section:** Upon reaching the first pump, the total cross-sectional area gradually decreases to B due to the pump shaft, meaning the same cross-section of solids must pass through a smaller opening.
3. **Converging Pipe to the Impeller:** The straight pipe converges into a bend where the total cross-sectional area increases due to the larger radial distance from the axis while maintaining the same spacing.
4. **Variation in Cross-Section:** At point D , the ratio of the pipe's cross-sectional area to the solids is the largest. From D , the flow returns to C and then to B , repeating through each stage of the pump.

In this specific situation, several points need attention:

- **Changing Cross-Sections:** The varying cross-sections in the pump will affect particle movement and can cause local density waves due to changes in velocity.
- **Vertical and Inclined Sections:** The system contains both vertical and declining pipe sections, increasing the likelihood of transient accumulation waves, especially with significant differences in particle velocities between these sections.
- **Frictional Losses:** In vertical pipe sections, frictional losses due to particle contact with the pipe wall are lower than in declining pipe sections. This means particles move faster in vertical than in declining sections, leading to differences in particle velocities.
- **Slip Ratio:** The slip ratio R_s , defined as the ratio between the average particle velocity and the mixture velocity, is higher in vertical pipe sections than in declining pipe sections at the same concentration, particle size, and pipe diameter.

E. de Hoog suggests that a narrowing of the pipe diameter should be applied to prevent density waves in the bends of S-waves. This creates a higher flow velocity. In the situation mentioned above, the opposite is true. The more space the solids have, the higher the settling velocity. Therefore, a larger total cross-sectional area at point D is desirable because friction losses are high due to the declining pipe sections.

2.4.3. Dimensionless Flow Parameters

Scaling particle transport in a vertical pipe requires maintaining dynamic similarity between the original and scaled systems. This involves ensuring that key dimensionless numbers remain in their range. The relevant dimensionless numbers in this context include the Reynolds number (Re), Froude number (Fr), and the dimensionless particle diameter $\frac{d}{D}$.

Dimensionless Groups of Interest

Using the Buckingham π theorem, the relevant dimensionless groups for the system are:

1. **Reynolds Number (Re):** Ratio of inertial forces to viscous forces.

$$Re = \frac{\rho v D}{\mu}$$

2. **Dimensionless Particle Diameter:** Ratio of particle diameter to pipe diameter.

$$\frac{d}{D}$$

Solid phase Reynolds number Based on the dimensionless Reynolds number, the regime in which the flow is located can be determined. In the situation of solids in a riser, the solid phase Reynolds number is considered. This considers the difference between v_f and v_{th} . A Reynolds number above 3500 indicates a turbulent regime. In the system considered in this thesis, the number is well above 3500. When scaling to a test setup, remaining in the same regime is important.

$$Re_p = \frac{|v_f - v_{th}| \rho d}{\mu} \quad (2.2)$$

Stokes Number The Stokes number (St) characterizes the behavior of particles in a fluid flow. If $St \ll 1$, particles follow the fluid well, and if $St \gg 1$, particles detach from the flow. Van Wijk gives a suggested method to compute the Stokes number for large particles:

$$St = \frac{4(\rho_s - \rho_f) d u_m}{3 \rho_f D v_t C_D} \quad (2.3)$$

where ρ_s is the particle density, ρ_f is the fluid density, d is the particle diameter, u_m is the mixture velocity, D is the pipe diameter, v_t is the terminal settling velocity, and C_D is the drag coefficient of a particle. [59]

Scaling Factor Define the scaling factor for the diameter of the pipe as k :

$$k = \frac{D}{D_m} \quad (2.4)$$

$$k = \frac{d}{d_m} \quad (2.5)$$

2.5. Conclusion

In this conclusion, the key findings of the research are summarized, addressing the research questions and discussing the implications for deep-sea mining systems. The focus is on the performance and challenges of multi-stage centrifugal pumps in the hydraulic transport of polymetallic slurries from the seabed. Preliminary answers to the research questions are provided, with each response being based on the literature review.

- *What are the potential benefits and drawbacks of using multi-stage centrifugal pump versus other types of pumps in terms of internal flow properties in deep-sea nodule collecting systems?*

Multi-stage centrifugal pumps are specifically designed to handle the high-pressure requirements of deep-sea mining operations. They achieve significant heads using multiple impellers arranged in series on a single shaft, allowing them to overcome substantial vertical distances. This makes them highly effective for transporting slurries containing polymetallic nodules from the seabed to the surface. The multi-impeller design ensures effective energy transfer to the mixture, resulting in higher overall efficiency compared to single-stage pumps or airlift systems.

However, these pumps present several technical challenges. Their design and construction are more complex than those of single-stage pumps and airlift systems. Each stage includes an impeller and a diffuser, requiring precise alignment and assembly for optimal performance. Additionally, maintenance and repair of submersible pumps are challenging due to their inaccessibility when deployed at depths of 1000 meters or more. Although designed for minimal maintenance, any necessary repairs require retrieval to the surface, which is both time-consuming and costly.

Compared to single-stage pumps with simpler designs and are easier to maintain, multi-stage centrifugal pumps offer higher efficiency and better performance in handling high-pressure and long-distance slurry transport. In contrast, airlift systems, while less complex, have several disadvantages. First, they are generally less efficient. Second, they exhibit poor control when the flow becomes unstable, due to the system's slow reaction time. Third, the behavior of an air-water-solids flow within the riser is complex, making it difficult to accurately predict and design for in such systems.

In conclusion, while multi-stage centrifugal pumps provide significant advantages in terms of efficiency and high-pressure handling, their complexity and maintenance challenges must be carefully considered in deep-sea mining applications.

- *What are the key physical phenomena and engineering limits in multi-stage centrifugal pump designs that affect the flow assurance for the hydraulic transport of particles of various diameters in deep-sea mining applications?*

In multi-stage centrifugal pump designs for deep-sea mining, several key physical phenomena and engineering limits significantly impact flow assurance for particle hydraulic transport. These phenomena and limits include density waves, wear and erosion, flow passage design, axial thrust management, and risks related to reflux-induced blockages.

Density waves can form due to erosion-driven or sliding bed-driven mechanisms. These waves occur when mixture velocities are too low or when particles accumulate and form a sliding bed. Additionally, transient accumulation waves can arise in systems with both horizontal and vertical sections due to significant differences in particle velocities between these sections.

Flow instabilities can occur due to sudden changes in the flow path, particularly at the interfaces between the impeller and the diffuser. These instabilities cause localized high-pressure and high-velocity areas, leading to increased wear and potential mechanical failures.

When reflux of solids occurs after the pump stops working, the particles should pass freely through the pump to avoid blockages. However, critical locations where blockages are most likely to form include the pipeline transition into the pump, the transition between the first and second pump stages, and the junction between the impeller and the diffuser. These areas are prone to particle accumulation, limiting the reflux capacity of the pump.

To ensure the reliable hydraulic transport of particles, it is essential to account for wear caused by particle impacts on pump components such as impellers and diffusers. Larger particles increase the wear rate, while fine particles may lead to clogging and higher frictional losses. Sufficiently wide flow passages are required to minimize these risks and maintain performance.

- *How do operational variables, such as mixture concentration and particle size distribution, influence the flow assurance and performance of multi-stage centrifugal pumps in DSM applications?*

Operational variables such as mixture concentration and particle size distribution significantly influence the flow assurance and performance of multi-stage centrifugal pumps in deep-sea mining (DSM) applications. Higher mixture concentrations increase the density and viscosity of the slurry, leading to greater frictional losses. This reduces the pump's efficiency and raises the risk of agglomeration and blockages, particularly at critical points like the diffuser-impeller junction or balance holes.

Particle size distribution plays a crucial role in flow assurance. Polydisperse mixtures, where smaller particles fill gaps between larger ones, are more prone to forming severe blockages, particularly during reflux events. Monodisperse particles, by contrast, typically cause fewer blockages. Within a polydisperse system, larger particles can sometimes facilitate the reflux of smaller particles, mitigating blockage risks. However, when the size of particles exceeds a certain threshold, blockages become more severe. Additionally, the shape or sphericity of particles is critical, as less spherical particles experience greater resistance and are more prone to clustering, further disrupting flow. Combined with these variables, the density of solids affects the slip ratio between the particle and mixture velocities, influencing frictional interactions in both vertical and declining pipe sections.

3

Methodology

3.1. Introduction

Building upon the insights from Chapter 2, this experimental research aims to address the primary risks to flow assurance. The literature review examined flow assurance issues during both normal operation and reflux. Based on the testing facilities and their associated limitations, it was decided to focus on reflux. This choice is supported by findings in the literature, which indicate that flow assurance during reflux is often observed as a more significant issue.

Therefore, the experimental phase will focus entirely on investigating flow assurance issues during reflux. The results of these experiments should provide insights into the following aspects:

- **Blockage Mechanisms:** Identify the mechanisms that lead to blockages in the pump model.
- **Assessment of Pump Geometry:** Evaluate the influence of key geometrical parameters, including the spacing within the pump, the shape of the impeller and diffuser blades, and the design of the diffuser support.
- **Impact of Blockages:** Analyze the effects of variables such as solid density, mixture concentration, particle size distribution, and total volumetric flow on flow assurance.

To address these aspects, a test setup must be designed in which sections of the pump can be tested. L. Yuanwan et al. conducted research on reflux using Computational Fluid Dynamics (CFD) models and validated their findings with a test setup [10]. The results obtained from their CFD model corresponded closely with the blockages observed in the real-life pump during the experiments. This setup consisted of a 30-meter-high flow loop with a two-stage centrifugal pump, in which spherical solids were pumped. At a certain point, the pump was switched off to study the effects of reflux.

For this thesis, specific requirements were established that needed to be considered when designing the test setup:

- The setup must closely resemble a multistage centrifugal pump in design and function.
- The setup must fit within the designated location and be appropriately scaled to match the intended experimental conditions.
- Blockages must be both visible and measurable within the setup.
- The setup must operate as an open loop, as this configuration is desired to intentionally induce blockages for testing purposes.
- The setup must be operable by a single individual and executable within the time framework of this thesis.

Due to these requirements, the setup designed by L. Yuanwan was not replicated. However, it served as inspiration, particularly for using a two-stage pump and spherical solids. The results are intended to serve as a preliminary framework for further research into the feasibility of using multistage centrifugal pumps in the riser of a Deep Sea Mining (DSM) system.

The tests are divided into three experiments, each designed to investigate the mechanisms that influence blockages in the system. These experiments progress from focusing on 1D (axial) effects to 3D (axial, radial, and tangential) effects. Understanding the conditions under which specific mechanisms occur is essential to optimize the design of the pump and reduce the risk of blockages. By identifying when and why these mechanisms arise, it becomes clear which variables need to be adjusted to prevent blockages effectively. The three experiments are:

- **Fallpipe Experiments:** The settling behavior of batches with different variables is recorded. Variables such as initial concentration of the batch, height of the batch, solid size, and solid density are varied. These experiments focus on axial effects as the batches settle and provide insight into the composition of the batches as they arrive at the pump inlet. The results of these experiments are presented and discussed in Chapter 4.
- **Pump Without Blades Experiments:** In this experiment, the focus is on both axial and radial effects within the pump. The pump core will not be fitted with blades, allowing an assessment of whether the solid size relative to the spacing is sufficient and whether the specifications from previous studies are accurate. The results of this experiment are presented and discussed in Chapter 5.
- **Pump With Blades Experiments:** This experiment incorporates a complete pump stage, including impeller and diffuser blades, to study axial, radial, and tangential effects. Different combinations of batches are used to analyze the impact of the variables, providing a detailed understanding of the factors contributing to blockages. The results of this experiment are presented and discussed in Chapter 6.

3.2. Design Phase

The design phase of the pump model focuses on developing and creating a scaled prototype intended for testing and analysis. This section outlines the key design considerations, including the specifications, materials, and manufacturing processes used to construct the model pump. The model pump features a two-stage configuration consisting of impellers and diffusers, with a housing that accommodates interchangeable cores.

3.2.1. 3D Model Pump

This section examines the design of the model pump used in the setup. It briefly discusses the pump's specifications and how it was designed and manufactured.

Overview:

A model pump consisting of two stages is created for the test setup. The model pump consists of two impellers and two diffusers, collectively referred to as the core of the pump. The outer part of the model pump is referred to as the pump housing. Figure 3.1 shows an overview drawing of the model pump.

Pump Specifications:

Allseas provided the required pump specifications for the real-life pump. These specifications are partially based on the pump developed by OMI [43]. This provided a solid foundation, as the tests conducted by OMI demonstrated effective operation and reflux without any blockages. The specifications have been scaled to align with the configuration used by Allseas, with any missing data supplemented where necessary. The full specifications are presented in Table 3.1, with the corresponding locations illustrated in Figure 3.2.



Figure 3.1: Model pump

Table 3.1: Specifications of the Real-Life Pump and Model Pump

#	Component	Real-Life Pump	Model Pump
General Specifications			
1	Minimum Shaft Diameter	100 mm	32.0 mm
2	Incl. Key, Hub Diameter	125 mm	40.0 mm
3	Solid Passage Diameter	75 mm	24.0 mm
4	Ball Passage Diameter	95 mm	30.4 mm
5	Impeller Eye Diameter	315 mm	100.8 mm
6	Diffuser Support Thickness	16.63 mm	5 mm
7	Blade Thickness	15 mm	4.8 mm
Impeller Specifications			
	Number of Blades	3	3
8	Impeller Outlet Diameter	530 mm	169.6 mm
9	Impeller Outlet Width	95 mm	30.4 mm
10	Impeller Hub-to-Shroud Distance	95 mm	30.4 mm
Diffuser Specifications			
	Number of Blades	4	4
11	Diffuser Inlet Diameter	530 mm	169.6 mm

Spacing within the Pump:

The spacing between the impeller/diffuser and the pump housing remains consistent throughout the design, as shown in the middle image of Figure 3.2. This spacing, combined with the ball passage diameter (d_{bp}), is a critical specification, as it determines the maximum solid passage diameter (d_{sp}) of 24 mm that can pass through the pump, as described in Section 2. The ball passage diameter of 30.4 mm ensures that the impeller, diffuser outlets, and hub-to-shroud distance cannot be smaller than 30.4 mm.

Three diffuser supports connect the pump axis to the pump housing; one of these supports is shown in the left image of Figure 3.2. These diffuser supports have a scaled thickness of $t_{thick} = 5$ mm, which corresponds to an actual thickness of $t_{thick} = 16.63$ mm in the real pump.

The distance between the vanes varies across the impeller and diffuser due to differences in inlet and outlet width, as shown in the right image of Figure 3.2. As previously described, the spacing throughout the pump should not become less than 30.4 mm. This requirement is not met everywhere in the model pump provided by the supplier. At the location indicated with the * in Figure 3.2, the minimum spacing is only 25.8 mm. This critical distance is located between the vanes of the diffuser.

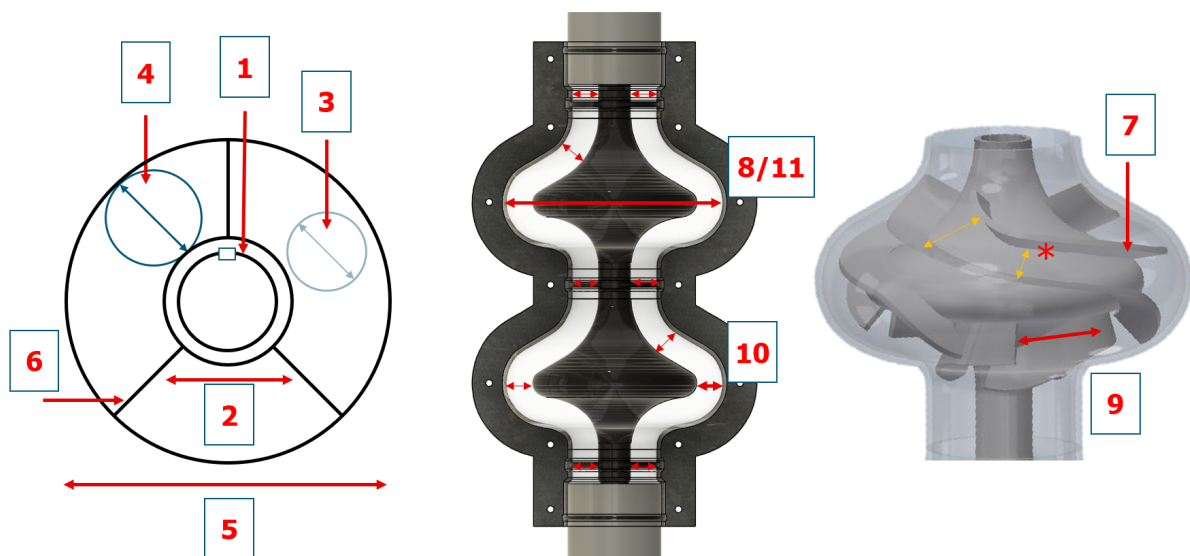


Figure 3.2: Overview of the pump specifications used for experimental tests. The key components are labeled as follows: (1) Minimum Shaft Diameter, (2) Incl. Key, Hub Diameter, (3) Solid Passage Diameter, (4) Ball Passage Diameter, (5) Impeller Eye Diameter, (6) Diffuser Support Thickness, (7) Blade Thickness, (8) Impeller Outlet Diameter, (9) Impeller Outlet Width, (10) Impeller Hub-to-Shroud Distance, (11) Diffuser Inlet Diameter.

Manufacturing

The pump model was designed with an interchangeable core, allowing the pump housing to be reused while only replacing the core. This feature reduces testing costs and enhances flexibility. The various core designs are discussed in Section 3.3.1.

Pump Housing:

The pump housing needed to be transparent, waterproof, strong, and capable of being opened to change the core for different versions while also allowing access in the case of blockages. These requirements were met using vacuum forming with transparent PET-G, a wall thickness ($t_{\text{thick}} = 5 \text{ mm}$). The material is impact-resistant due to its glycol content. First, a mold of the cross-section of the pump model was created. Then, through vacuum forming, the transparent PET-G was stretched over the mold, reproducing the previously designed 3D model with an accuracy of at least 1 mm. The two halves of the housing are secured together using a flange connection, rubber packing, and bolts.

Pump Core:

3D printing was employed for the core using the Fused Deposition Modeling (FDM) technique. Polylactic Acid (PLA) was used to print the core in multiple sections, which were manually assembled and glued together. These sections were connected via a central shaft. After assembly, the material underwent a brief post-processing treatment to achieve a smooth and uniform surface. Two cores were fabricated: one without blades and one with blades, which will be further discussed in Section 3.3.1.

3.3. Experimental Setup

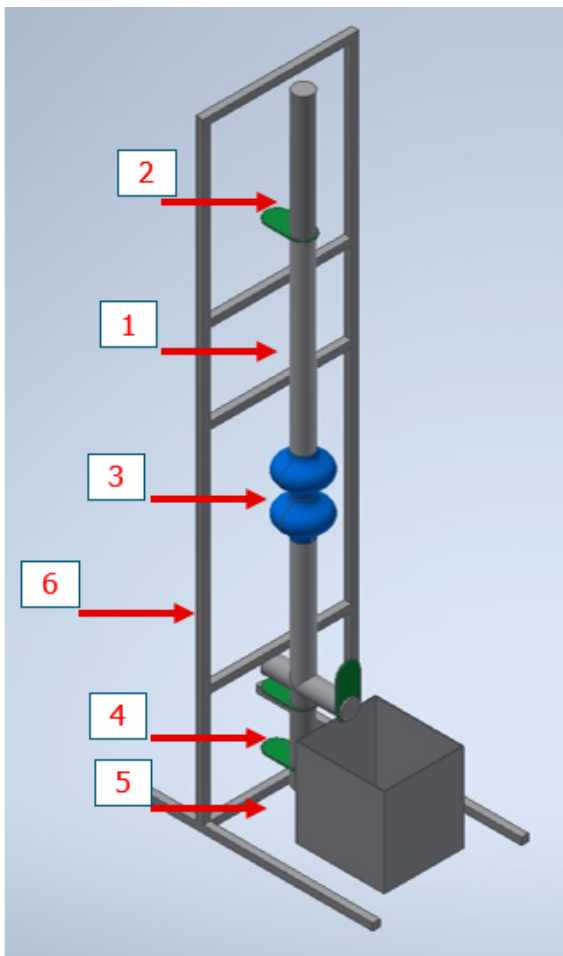
This chapter provides an overview of the experimental setup used to test the model pump. The setup includes key components such as the fallpipe, solid dispenser, and solid collection system. Each component and its role in the testing process are explained in detail. The aim is to understand the functionality and performance of the pump and related systems.

3.3.1. Overview Setup

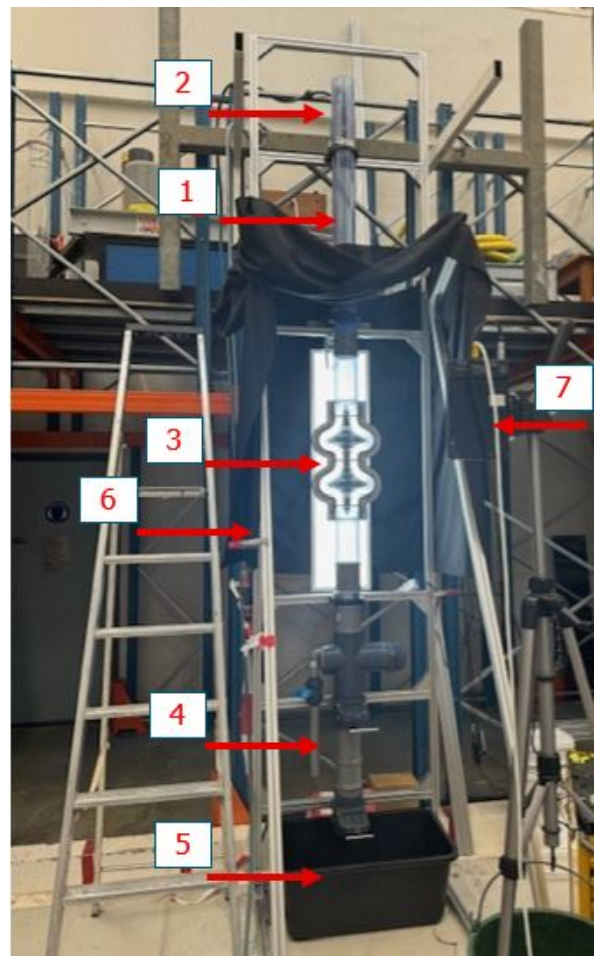
The side view of the experimental setup drawing is shown in Fig. 3.3a, while the as-built version is presented in Fig. 3.3b. The main components of the setup are listed below:

- **1. Fallpipe:** The central component of the setup where the experiments are conducted.
- **2. Solid Dispenser:** Positioned above the fallpipe, the dispensers are used for releasing the nodules into the system.
- **3. Model Pump:** Installed inside the fallpipe to replicate the pump behavior in the experimental conditions.
- **4. Solid Collector:** Located at the bottom of the fallpipe, connected to several valves for controlling the flow and collection of solids.
- **5. Water Collection Tank:** Positioned beneath the solid collector to gather the water from the experiments.
- **6. Frame:** A strong structure that securely supports the entire setup.
- **7. High-Speed Camera:** Positioned in front of the setup to capture detailed footage of the experiments.

In the following sections, each component of the setup will be explained and discussed in detail.



(a) Overview of Test Setup (Model)



(b) Overview of Test Setup (Real)

Figure 3.3: Comparison of the test setup

Fallpipe

The fallpipe configuration varies depending on the experiment, as shown in Fig. 3.4. In the initial experiment, the fallpipe consists of a single transparent PVC section totaling 2 meters, with an outer diameter ($D_{out} = 110$ mm), a wall thickness ($t_{thick} = 5.3$ mm), and an inner diameter ($D_{in} = 99.4$ mm). For the experiments involving the pump, a new configuration is used, consisting of three sections: a 27 cm pipe at the bottom, the model pump occupying a 60 cm section in the middle, and a 1.25 m pipe at the top. This modular design allows for the integration of the model pump while maintaining a similar overall configuration to the original fallpipe.

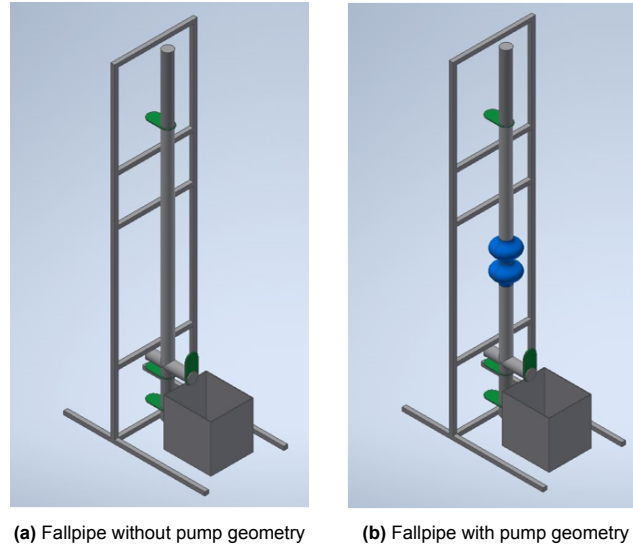


Figure 3.4: Configurations of the fallpipe

Solid dispenser

The solid dispenser, positioned on top of the fallpipe, is equipped with a gate valve for sealing. The dispenser has a total height of 30 cm. The term initial batch concentration (C_i) refers to the volume fraction of solids contained within the dispenser, commonly set at 26% or 55%. Standard batch heights (h_b) are defined as either 10 cm or 20 cm. This configuration is designed to reliably reproduce the initial test conditions rather than to establish a specific concentration at the pump. A detailed description of the dispenser's operation, along with confirmation tests for the initial concentration, is provided in Appendix C. Figure 3.5 schematically represents the initial concentration batches of 55% and 26%.

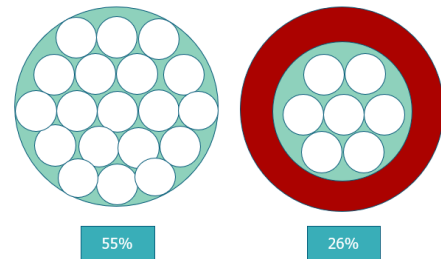


Figure 3.5: Influence of installed tube on initial concentration batch

Under normal operation, the average concentration (C_{avg}) in the riser is estimated to be 15%. However, due to phenomena such as density waves, as described by Van Wijk [59], the concentration can increase locally. During reflux, the concentration differences caused by these density waves are expected to become even more pronounced.

To account for these scenarios, an initial concentration of 26% and 55% were chosen to simulate worst-case conditions. These concentrations, combined with specific particle size distributions (PSD), allow for representation of the most challenging situations the pump may encounter.

Solid Collection Chamber

The solid collection chamber is located at the bottom of the fallpipe and is equipped with three valves for functionality. Valve 1 allows particles to fall into the chamber during the experiment, while valve 2 is used to remove particles after the test. Valve 3 is positioned above valve 1 and is used to drain water from the system into the collection tank, which has a capacity of 55 liters. The system also includes an opening with a screw cap on the left side for easy access to the pipe in case of blockages. Figure 3.6 highlights all components with colored boxes.

Model Pump

The model pump is described in Section 3.2.1. According to these specifications, two different pump cores were created: one without blades, specifically designed to examine the spacing between the core and pump housing, and one with blades, intended to evaluate the complete design. The modeled appearances of these pump cores are shown in Figures 3.7a and 3.7c, with the built versions displayed in Figures 3.7b and 3.7d. A drawing illustrating how the pump is mounted in the fallpipe is included in Appendix D.

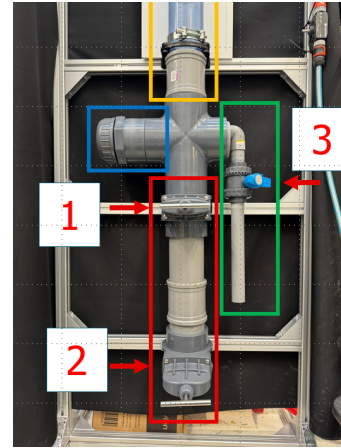


Figure 3.6: Overview lower part setup. (Green box: water outlet valve, Red box: Solid collector, Blue box: Screw cap, Yellow box: Fallpipe)

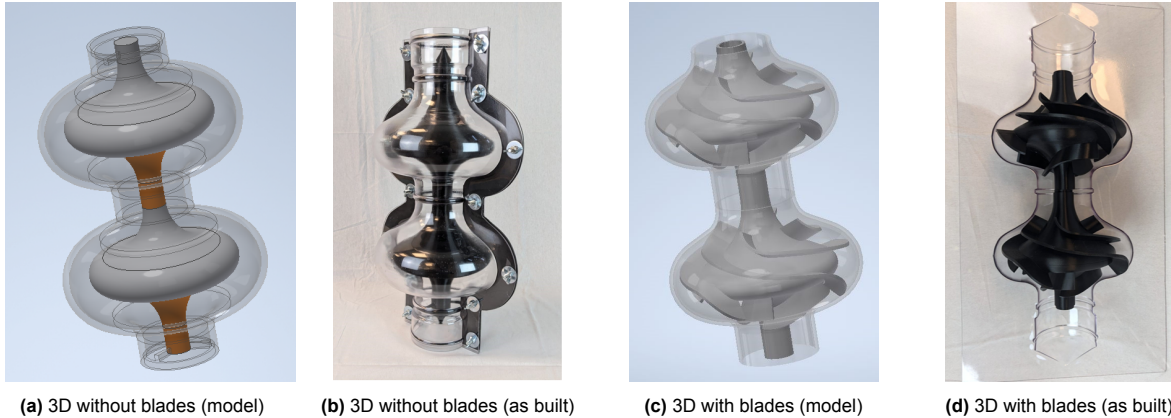


Figure 3.7: Comparison of 3D printed pump models: (a) and (b) without blades, (c) and (d) with blades.

Frame

The test setup is connected to the frame made of modular aluminum profiles. These are widely used in industrial and technical applications due to their strength, lightweight properties, and ease of assembly using standard fastening elements. The frame is 4 meters high, 0.8 meters wide, and 2.5 meters deep, reinforced by two cross-braces.

Nodule/solid

The tests used two types of solids to study the effects of density variations: glass spheres ($\rho_s = 2400 \text{ kg/m}^3$, solid density) and Polyoxymethylene (POM) spheres ($\rho_s = 1400 \text{ kg/m}^3$). Both types were ordered in diameters (d) ranging from 5 to 30 mm and were manufactured by Bell Balls with an initial tolerance of 0.1 mm.

POM spheres, selected for their lower density, were used in subsequent tests to evaluate the impact of density differences, while the higher-density glass spheres were used to represent denser materials. Because the sizes available from the supplier varied between the two materials, there is some variation in the sizes used in the tests. POM was ordered in sizes 5, 10, 15, 20, 24, and 30 mm, while glass spheres were ordered in sizes 5, 10, 14, 20, 25, and 30 mm. For this reason, size references in this report are written as 5, 10, 14/15, 20, 24/25, and 30 mm to account for these differences.

After testing, it was found that the size tolerance deviated for both materials, with POM spheres measuring up to $\pm 0.3 \text{ mm}$ and glass spheres up to $\pm 0.5 \text{ mm}$. Additionally, the density of the 20 mm glass spheres deviated from specifications, measuring $\rho_s = 2860 \text{ kg/m}^3$ instead of $\rho_s = 2400 \text{ kg/m}^3$.

3.3.2. Experimental Measurement

Image Capturing

The experimental setup includes a Fastec IL5 high-speed camera equipped with a Navitar 25 mm F0.95 lens. The wide aperture of the lens enhances light sensitivity, making it suitable for high-speed imaging with minimal motion blur.



Figure 3.8: Fastec IL5

Mass Measuring

The particle batch is measured using a Kern precision scale with an accuracy of 0.001 g and a suitable range, ensuring accurate mass measurements for determining the solids placed in the dispenser and retained in the pump.

3.4. Experiments as planned

The experimental program is divided into three categories: Fallpipe Experiments, Pump Without Blades, and Pump With Blades. Each experiment consists of multiple series designed to investigate key parameters, with the series building upon each other. Figure 3.18 provides a structured overview of the experimental setup. The categories are further elaborated in the sections on A: Fallpipe Experiments (3.4.1), B: Pump without Blades Experiments (3.4.2), and C: Pump with Blades Experiments (3.4.3).

This structured approach provides a consistent reference system throughout the report, making tracking each experiment, series, and objective easier.

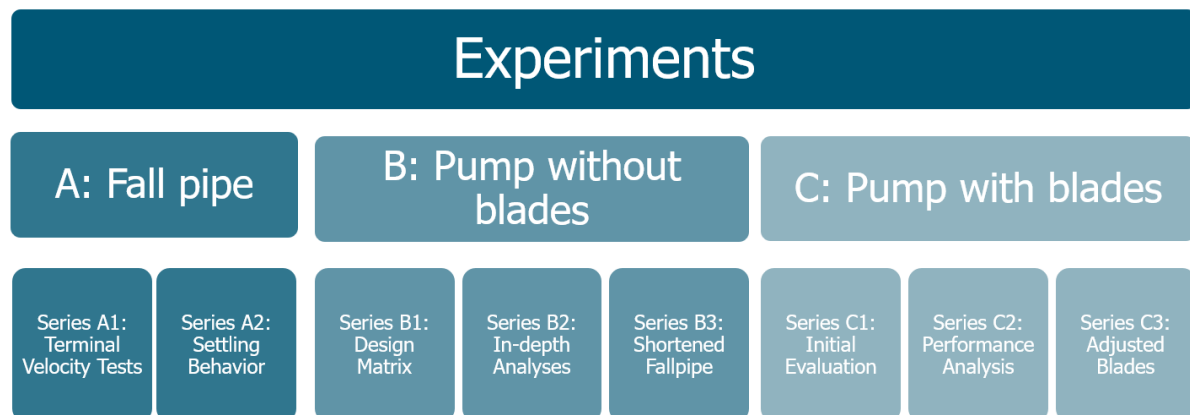


Figure 3.9: Overview Experimental tests

3.4.1. A: Fallpipe Experiments

As mentioned in Section 3.3.1, the first experiment consists of a fallpipe without obstructions. This experiment is split into two series: the first series involves individual solids, while the second involves batches of solids. The primary objective of the first series is to determine the terminal settling velocities (v_t) of different particles. The second series is focused on visualizing how the solids move as a batch through the pipe, rather than on determining exact arrival concentrations. This series aims to provide insight into the behavior and appearance of the solids as they approach the pump intake in later tests. See Appendix J for an overview of all these tests.

Series A1: Terminal Settling Velocity This test series aims to determine the terminal velocity of a single particle. In each trial, the particle is released using a solid dispenser, initiating its descent within a transparent tube. Two markers are placed 50 cm apart along the tube to accurately measure the particle's velocity. A high-speed camera captures the particle's movement, enabling the calculation of the time at which it crosses each marker. The time difference and the known distance allow for calculating the particle's terminal settling velocity. For each test, ten random particles are selected from the set to ensure consistent results. The variations in the tests include solid density (glass spheres and POM spheres) and diameter (5, 10, 14/15, 20, 24/25, and 30 mm).

The test procedure can be found in Appendix C.

Series A2: Settling behavior of batch The second series objective is to observe particle batches' hindered settling velocity (v_h) before they reach the pump intake. In this series, batches of particles are introduced and monitored as they descend, allowing for an assessment of their settling behavior over time and distance. High-speed imaging is used to capture the behavior of each batch, providing data on settling patterns under controlled conditions. For this test, glass spheres and POM spheres are used, in sizes 10 mm and 20 mm. The particle batches vary in height (10 cm and 20 cm) and initial batch concentration, with 26% or 55%. These variations allow for a comparison of settling behavior under different conditions.

The procedure for Series A2 is the same as in Series A1. A step-by-step document is filled in during the tests to ensure no mistakes are made. This is shown in Appendix C.

3.4.2. B: Pump without Blades Experiments

After the fallpipe test, the first model pump configuration tested is the one without blades. This experiment is divided into three series.

Series B1: Test Matrix After establishing how the solids behave in a standard pipe without obstructions, the study shifts focus to the pump, which is the primary interest of this research. This series begins with examining the pump without blades, as outlined in Section 3.3.1, to identify variables most likely to cause blockages. By pinpointing these critical factors, further testing can focus on those, including repeat tests for deeper insights.

A test matrix is used to systematically test combinations of variables such as solid density, size, initial concentration batch, and batch height, observing where blockages tend to occur. This method reveals patterns and key factors contributing to clogging, which can then be analyzed in more detail to understand their impact on pump performance.

For this series, particle batches are tested with glass spheres and POM spheres, particle sizes of 10, 20, 24/25, and 30 mm, initial batch concentration of 26%, 46%, and 55%, and batch heights of 10 and 20 cm. This results in a total of 48 tests needed to evaluate the impact of these variable combinations on potential pump blockages. In the next series, further testing will focus on the identified critical variables to assess their specific impact on pump performance.

Series B2: In Depth Analysis After Series B1 has determined the key variables contributing to blockages, Series B2 will investigate the likelihood and frequency of blockages under varying conditions. For example, if Series B1 indicates that blockages are more likely with a particle diameter of 25 mm and a batch height of 20 cm, further testing in Series B2 will concentrate on these specific conditions to gather detailed insights.

The specific sequence of tests for Series B2 is intentionally left flexible until the conclusions of Series B1 are available, allowing for an adaptive approach that focuses on the most critical blockage-inducing factors.

Series B3: Shortened Fallpipe In Series B1 and B2, a 1.25 m fallpipe is used before the solids

reach the pump intake. This length allows the particle batch sufficient time to settle, leading to a lower effective arrival concentration due to rarefaction. Shortening the fallpipe to 0.45 m reduces settling time, resulting in less rarefaction and causing a higher arrival concentration at the pump inlet.

A step-by-step document is filled in during the tests to ensure no mistakes are made. This is shown in Appendix C.

3.4.3. C: Pump with Blades Experiments

In this series, the pump core will be replaced with a core equipped with blades.

Series C1: Initial Evaluation This series investigates the reflux performance of the pump with monodisperse batches consisting of different solid sizes, initial batch concentrations, and batch heights, using both glass and POM spheres. The primary objective is to systematically isolate and understand the influence of individual variables on reflux and blockage formation. This controlled approach allows for a more fundamental understanding of the pump's behavior during reflux and the mechanisms driving blockage formation. Each test is conducted once to provide an initial assessment of these variables and to identify where and why blockages occur.

Series C2: Performance Analysis In Series C2, repeated tests are conducted with polydisperse batches, focusing on three distinct batch types. This series examines the influence of different particle size distributions on reflux dynamics and blockage formation. By studying the interaction between particles of varying sizes and densities, the experiments aim to map out the processes causing blockages and to identify critical factors that limit reflux performance in the pump setup.

Series C3: Adjusted Blades Following Series C2, the main bottlenecks for flow assurance during reflux are identified. This series implements minor adjustments to the pump core design to address the identified issues. Tests are then conducted to evaluate the effectiveness of these modifications in improving reflux performance.

A step-by-step document is filled in during the tests to ensure accuracy and consistency. This is shown in Appendix C.

4

Fallpipe Experiment

4.1. Introduction

This chapter presents the results of the Fallpipe experiments, divided into two series: **Series A1: Terminal Settling Velocity** and **Series A2: Settling Behavior of Batches**.

Series A1 examines the terminal settling velocity of individual solids and the impact of particle properties in confined spaces. **Series A2** investigates the settling dynamics of particle batches, highlighting the influence of initial batch concentration and solid size.

The analysis in this chapter focuses on axial processes, providing insights into particle behavior along the vertical axis of the fallpipe. These findings serve as a basis for further analyses of model pump performance.

4.2. Series A1: Terminal Settling Velocity

This section presents the results of the fallpipe experiments conducted with individual solids. The primary aim was to determine the terminal settling velocity and the behavior of solids with varying densities and sizes during their descent. Detailed descriptions of the experimental setup are provided in Section 3.4.1. The section begins by introducing the theoretical formula and outlines the adjustments needed to compare the theoretical predictions with the experimental results. It then presents the findings and corresponding observations, concluding with a discussion of the outcomes.

For this series, a confirmation test was first conducted. The solid must have already reached its maximum velocity, the terminal settling velocity. A verification was performed to ensure that the 1.5-meter drop pipe is sufficiently long before the measurement point. This verification is detailed in Appendix I. The results indicate that the velocity is achieved after just 0.30 meters, confirming that the 1.5-meter length is more than adequate.

Terminal Settling Velocity

To compare the experimental results, they will be evaluated against the theoretical equation. The theoretical equation for terminal settling velocity, as described in Section 2.2, is expressed as:

$$v_t = \sqrt{\frac{4 \cdot g \cdot (\rho_{\text{solid}} - \rho_{\text{fluid}}) \cdot d_{\text{solid}}}{3 \cdot \rho_{\text{fluid}} \cdot C_d}} \quad (4.1)$$

To account for the confined environment in which the solids settle, an additional term must be introduced to the equation. This term should account for the d/D ratio, which significantly influences the terminal settling velocity, primarily due to the drag acting on the solids.

In Section 2.2, Equation 2.2.1 provides the hindered settling velocity for batches within a pipe, as described by Richardson and Zaki [50]. However, to accurately represent the behavior of individual solids, rather than a batch, this equation requires some modification. The term, $(1 - c_v)^n$, which accounts for mixture concentration, is removed, resulting in the following formula:

$$v'_{th} = \sqrt{\frac{4 \cdot g \cdot (\rho_{solid} - \rho_{fluid}) \cdot d_{solid}}{3 \cdot \rho_{fluid} \cdot C_d}} \cdot 10^{-d/D} \quad (4.2)$$

Results and Observations

The results of all individual tests are presented in Appendix E. The data has been plotted for each solid size and density to illustrate key trends. The graphs show the terminal settling velocity for glass and POM spheres across the test series. The cumulative mean terminal settling velocity is also included, representing the progressively calculated mean velocity up to each point in the series.

To provide a comprehensive overview of the results, Tables 4.1 and 4.2 present the mean mass of the solids along with the corresponding mean terminal settling velocity for each tested solid size.

Table 4.1: Summary of Mean Mass and Mean Terminal Settling Velocity for Glass Spheres

Test Range	Density (kg/m ³)	Solid Size (mm)	Mean mass of Solid (g)	Mean Terminal Settling Velocity (m/s)
2001–2010	2400	5	0.162	0.437 ± 0.057
2011–2020	2400	10	1.36	0.495 ± 0.019
2021–2030	2400	14	3.44	0.641 ± 0.078
2031–2040	2860	20	12.0	0.845 ± 0.068
2041–2050	2400	25	19.6	0.814 ± 0.065
2051–2060	2400	30	32.9	0.838 ± 0.048

The table shows a different density for the glass spheres with a diameter of 20 mm. This is due to an error in the supplier's delivery.

Table 4.2: Summary of Mean Mass and Mean Terminal Settling Velocity for POM Spheres

Test Range	Density (kg/m ³)	Solid Size (mm)	Mean Mass of Solid (g)	Mean Terminal Settling Velocity (m/s)
3001–3010	1400	5	0.0913	0.225 ± 0.008
3011–3020	1400	10	0.714	0.310 ± 0.049
3021–3030	1400	15	2.39	0.373 ± 0.042
3031–3040	1400	20	5.63	0.389 ± 0.051
3041–3050	1400	24	9.81	0.383 ± 0.052
3051–3060	1400	30	18.9	0.384 ± 0.028

Key observations from Tables:

- Terminal settling velocity increases with solid size up to 20 mm.
- Deviation remains minimal across all solid sizes, with the highest recorded deviation being 16% for POM solids of 10 mm, indicating consistent measurement precision.
- Mean terminal settling velocities of POM spheres are lower compared to the glass spheres due to the reduced mass of the solids, as expected.

Visual observations from the footage reveal that in some tests, the solids made contact with the wall of the pipe. Comparing the footage data with the individual test results shows that solids making wall contact exhibit a lower settling velocity. This phenomenon was also noted during testing and is documented in Appendix E. Figure 4.1 provides a visualization of this wall contact.

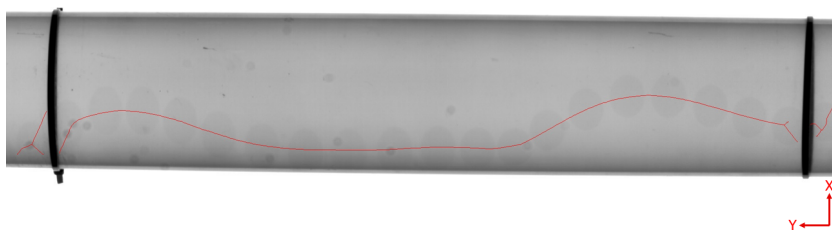


Figure 4.1: Wall friction

Discussion Series A1 To visualize the overall trends in mean terminal settling velocity as a function of solid size, Figure 4.2 combines the data from all tests. This figure provides a clear overview of the relationship between solid size and mean terminal settling velocity.

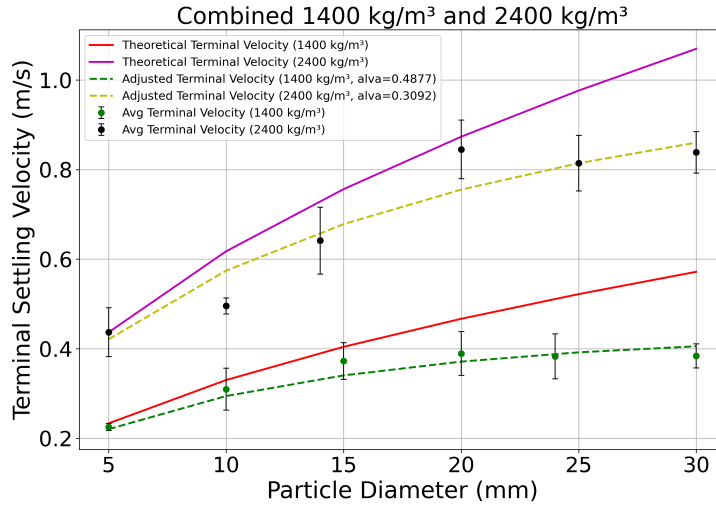


Figure 4.2: Comparison of measured and theoretical terminal settling velocities for Glass and POM spheres

The equation 4.2 tends to underestimate the velocity for a single solid, likely due to the drag coefficient, which is set at 0.46. Research, as elaborated in Appendix G, indicates that this coefficient should be higher in confined spaces. To address this, a correction factor is introduced to emphasize the influence of the d/D ratio. Incorporating this correction factor results in the following modified equation:

$$v''_{th} = \sqrt{\frac{4 \cdot g \cdot (\rho_{\text{solid}} - \rho_{\text{fluid}}) \cdot d_{\text{solid}}}{3 \cdot \rho_{\text{fluid}} \cdot C_d}} \cdot 10^{-(\alpha) \cdot d/D} \quad (4.3)$$

The parameter alpha (α) in this formula was determined by optimizing for the best fit between the predicted velocities and the experimental data. This was achieved by minimizing the difference between the adjusted terminal hindered settling velocity (v''_{th}) and the measured average terminal settling velocity for various particle sizes. The resulting α values provided the best match to the observed data, as indicated by the highest R^2 value.

For the 1400 kg/m³ dataset, the optimized α is 0.4, with an R^2 value of 0.90, indicating a strong correlation. For the 2400 kg/m³ dataset, the optimized α is 0.31, with an R^2 value of 0.90, which also reflects an accurate fit.

These optimized α values reveal that the correction factor adjusts not only for the d/D ratio but also for density-related effects. The difference in α between the two densities highlights the significant influence of solid density on the system's behavior. In conclusion, the correction factor improves the prediction of terminal velocity while accounting for the d/D ratio and density in confined systems.

A reasonable correlation is observed when comparing the experimental results with equation 4.3. The terminal settling velocity increases with solid size up to 20 mm, after which it stabilizes or slightly decreases. This trend is observed for both densities, with the 20 mm glass sphere positioned higher due to its higher specific density. For the 10 mm glass spheres, the measured velocity was lower than expected. This deviation is hypothetically caused by contact with the pipe wall, as observed in several tests. To address this, a second analysis was performed, excluding tests with wall contact. While this resulted in slightly higher mean velocities for all solid sizes, the 10 mm solid still deviated from the trend. The optimized α and R^2 values for the filtered dataset were also determined, but the fit was less accurate, indicating that filtering in this manner is not a reliable solution. The results and corresponding figure can be found in Appendix. E. A repeat of the 10 mm test would be required to verify the observed discrepancy, but this was deemed outside the scope of this study.

4.3. Series A2: Settling Behavior of Batch

This section presents the results of the second series of the fallpipe experiment, which investigates the settling behavior of particle batches. Particle batches composed of glass and POM spheres were tested, using solids with sizes of 10 mm and 20 mm. The batches varied in height (10 cm and 20 cm) and initial batch concentrations of 26% and 55%. First, the results are visualized, and observations are described. The tests are divided into the two materials. After analyzing the results, a discussion is provided.

Results Glass Spheres

Three tests were conducted for each combination of variables for glass spheres. This repetition was performed to assess whether the settling behaviors are generally consistent under identical conditions. An overview of all these test conducted is provided in Appendix. J.

For each test group, an overview of one representative test has been created, which can be found in Appendix E. Figures 4.3 and 4.4 provide examples of these overviews. The overview was created by capturing frames at consistent time intervals. A time step of 0.297 seconds was chosen for this purpose. This approach ensures that the settling behavior can be analyzed uniformly across all tests.

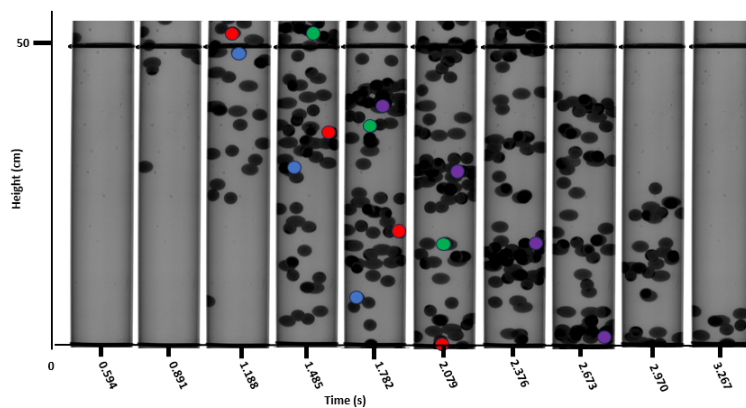


Figure 4.3: Overview of Settling behavior Test Glass Spheres, 20 mm, Initial Concentration 46%, Batch Height 20 cm, Timestamp 0.297 s)

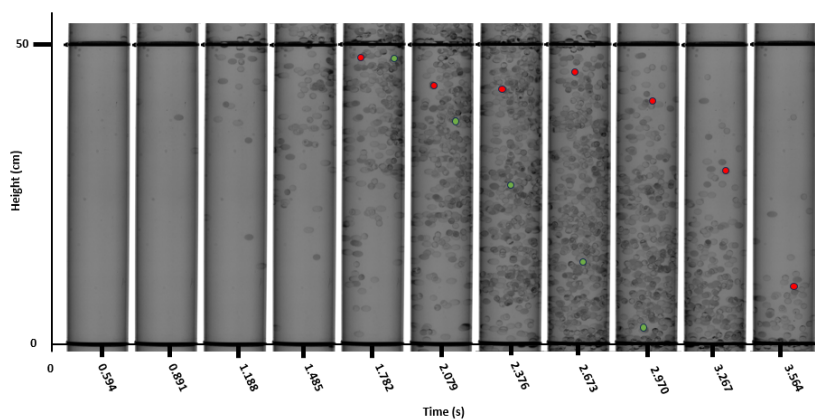


Figure 4.4: Overview of Settling behavior Test (Glass Spheres, 10 mm, Initial Concentration 26%, Batch Height 20 cm, Timestamp: 0.297 s)

Key observations

From analyzing the video material, several key observations can be made:

- When the valve is opened, the batch is initially dense and behaves like a plug.
- Almost immediately, the batch spreads over a larger distance, and a rarefaction wave forms due to differences in particle velocities caused by interactions with the surrounding medium and gravity. This phenomenon is visible in the initial frames of Figure 4.3.

- Due to the distance between the valve and the first measurement point, the solids arrive in a dispersed state.
- **Size 20 mm** small groups of solids hinder each other, resulting in a more substantial hindrance effect. Solids moving independently exhibit significantly higher velocities. This is evident in Figure 4.3, where the solids marked in blue and red demonstrate this behavior. The red solid is part of a cluster, while the blue solid moves independently.
- **Size 10 mm** no cluster forming is shown.
- **Size 10 mm**, particularly in batches with a higher volume, some solids near the wall remain at a stable level or even move upward against gravity. This is caused by the upward flow generated by the larger volume occupied by the solids.

Results POM spheres

After completing the first 15 tests of the series for POM spheres, as described in Appendix J, it was decided to reduce the number of tests. The tests showed significant agreement with the glass spheres series results. By reducing the number of tests, time was saved, allowing for a more detailed analysis in later tests.

The settling behavior of POM spheres closely resembles that of glass spheres under comparable conditions. Figures illustrating these tests can be found in Appendix E, but they are omitted here to avoid redundancy. Due to their lower density (1400 kg/m^3), POM spheres settled more slowly than glass spheres. The time step between frames was adjusted to 0.509 seconds to capture the slower settling process effectively and to create the figures in the appendix.

Discussion Series A2 Before opening the valve of the solid dispenser, the batch of solids can be observed as a cluster. Upon opening the valve, a rarefaction wave propagates through the system. For larger solids, some particles remain in cluster formation or form new clusters after descending for a certain distance. This clustering leads to significantly reduced settling velocities within these clusters compared to the individual particles in the dispersed "particle rain." This behavior highlights that the settling velocity of solids within the dense batch is substantially lower than the terminal settling velocity defined in Section 4.2, consistent with the principles of hindered settling.

Moreover, the volume occupied by the settling solids induces a counterflow in the surrounding fluid. This counterflow is particularly pronounced near the walls for solids with a diameter of 10 mm, generating upward fluid velocities. Consequently, some particles near the wall are entrained in the upward flow, rising against gravity. This observation provides valuable insights into the dynamics of solid movement and could inform the interpretation of results in subsequent tests. The implication of this upward flow within the pump system is significant, as similar conditions may arise. The interaction between upward fluid movement and solid settling within the pump could affect particle behavior and operational performance, making this phenomenon an essential area for further investigation.

4.4. Take Away: Fallpipe

Series A1: Terminal Settling Velocity Series A1 provides a clear understanding of the terminal settling velocity of individual solids. The results highlight the significant influence of the d/D ratio and the density of the solid on terminal settling velocities within the pipe. This effect becomes more pronounced with larger solids, emphasizing the importance of accounting for both confinement effects and density when designing systems for transporting solids through pipes or pumps.

Series A2: Settling behavior of Batches Series A2 demonstrates the settling behavior of particle batches, offering insights for future experiments. The results highlight how batches arrive at the model pump, providing valuable information on their behavior during transport. A notable observation is the upward fluid flow generated counter to the settling direction of the solids. This flow reduces the settling velocity of particles and, in some cases, even causes them to move upward with the flow. This phenomenon could significantly impact particle movement and distribution within the model pump.

Additionally, clusters frequently formed within the settling batches, significantly increasing the local concentration. This increase in concentration could pose operational challenges upon entering the model pump, potentially causing blockages or flow disruptions. The findings from both series provide a foundational understanding of single-particle settling and batch dynamics under confined conditions. The results underscore the importance of considering hindered settling, counterflow effects, and cluster formation when analyzing particle transport in the model pumps. These insights will play a pivotal role in analyzing the model pump's performance and reliability in subsequent experiments.

5

Pump Without Blades Experiment

5.1. Introduction

This chapter presents the results of experiments with the pump without blades, organized into three sections corresponding to the research series: **Series B1: Test Matrix**, **Series B2: In-depth Analysis**, and **Series B3: Shortened Fallpipe**. The analysis in this chapter focuses primarily on the axial and radial components of the physical processes. Each section includes an analysis of experimental results, focusing on key variables influencing solids behavior and the reflux performance of the model pump. A comprehensive discussion integrates the findings from all three series.

Series B1 applies a test matrix to identify critical variables affecting the occurrence of blockages. These insights form the foundation for the subsequent in-depth investigation in Series B2.

Building on Series B1, **Series B2** examines the probability and frequency of blockages under varying conditions. This series focuses on the most influential factors to gain deeper insights into potential disruptions to model pump performance.

In **Series B3**, the effect of a shortened fallpipe is analyzed. By reducing the fallpipe length, solids are introduced to the model pump intake with a higher arrival concentration ($C_{arrival}$), allowing for an assessment of its impact on performance.

Finally, the discussion at the end of this chapter integrates the findings from all three series, providing a detailed understanding of solids' behavior and their impact on the model pump.

5.2. Series B1: Test Matrix

The first series aimed to identify the key variables on which the subsequent two series should focus. To select these variables, 20 tests were conducted, as described in Section 3.4.2. A detailed overview of these tests can be found in Appendix F. It is important to note that the total weight varied between tests due to differences in the composition of the batches.

Results and Observations

This series primarily tested POM spheres. Glass spheres were also tested but passed through the pump without retention or blockage and are not further analyzed, as they offer no additional insights into retention behavior under current conditions.

The results of the tests with POM spheres are summarized in Table 5.1, indicating the number of solids retained in the model pump. A ✓ denotes no retention, while x indicates retention. Figure 5.1 shows an example from a test with 30 mm solids with photographic documentation.

Table 5.1: Summary of Results for POM Spheres by Size, Concentration, and Batch Height.

Size (mm)	26% (Initial Concentration)		46% (Initial Concentration)		55% (Initial Concentration)	
	Height: 10 cm	Height: 20 cm	Height: 10 cm	Height: 20 cm	Height: 10 cm	Height: 20 cm
10	✓	✓	✓	✓	✓	✓
20	✓	✓	✓	✓	✓	✓
25	✓	✓	✓	✓	✓	✓
30	x	x	-	-	x	x

Due to the design of this series, the results presented in Table 5.1 provide an immediate and clear understanding of the observed outcomes. Specifically, it becomes evident that only solids with a size of 30 mm are retained in the model pump, while no retention occurs for other solid sizes.

Table 5.2 presents the number of solids introduced into the model pump for each test to facilitate a clear comparison. It is important to note that in the test with 55% initial concentration and a height of 20 cm, the batch should theoretically consist of 1198 g of solids. However, this test was conducted with 1016 g due to a shortage of solids. Further details are in Appendix F.

Table 5.2: Weight and Approximate Number of Spheres for Different Initial Concentrations and Batch Heights.

Initial Concentration (%)	Height (cm)	Weight Solids (g)	Approx. Number of Solids (-)
26%	10	284	15
26%	20	569	30
46%	10	503	27
46%	20	1006	53
55%	10	599	32
55%	20	1198 (1016g)	63

**(a)** View from the left side showing solids retained.**(b)** View from the right side showing solids retained.**Figure 5.1:** Comparison of Left and Right Views: Test Results with 30 mm Solid Showing Solids Retained at Different Locations.

Figure 5.2 presents the results from the tests conducted with 30 mm solids. The Y-axis represents the number of solids (approximate and retained), while the X-axis displays the concentration and batch height. The graph indicates consistent profiles for retained solids across all test conditions. The influence of batch height and initial concentration remains minimal, as variations in the results are limited to small differences. These findings make it difficult to draw definitive conclusions about the impact of these parameters.

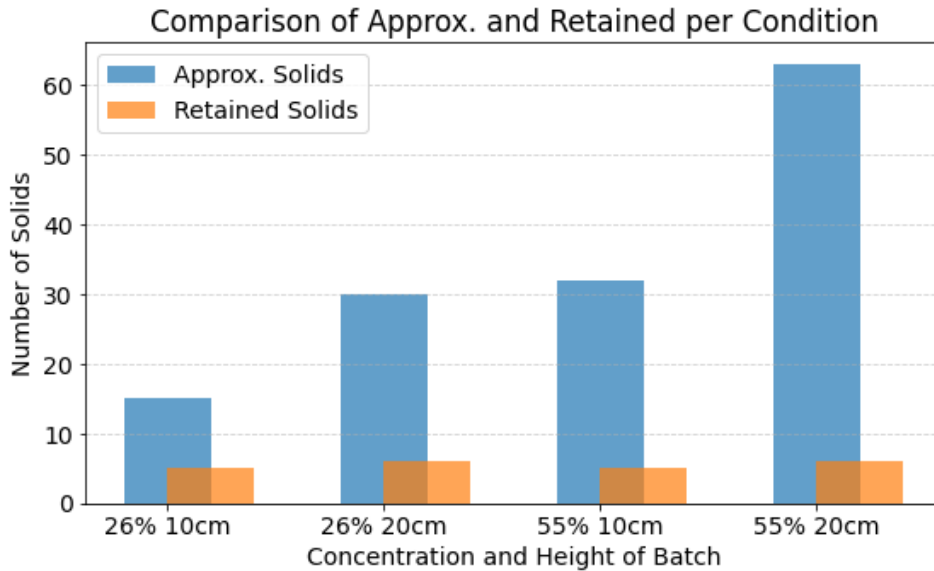


Figure 5.2: Results for 30 mm POM spheres under varying batch heights and concentrations.

Discussion Series B1

The pump specifications, as described in Section 2.4.1, establish a minimum passage size of 24 mm, and tests demonstrate that monodisperse solids up to 25 mm pass through without issues. Observations for 30 mm solids reveal some retention, making this size a useful reference point for further investigation. Additional analysis of factors such as batch height and initial concentration is necessary to better understand the conditions contributing to blockages.

5.3. Series B2: In-Depth Analyses

Series B2 focuses on the effects of initial batch concentration and batch height for 30 mm solids. Following the analysis of monodisperse batches, tests with polydisperse batches will explore the impact of a distribution of solids within the pump.

Results and Observations

Monodisperse Batch

Four combinations of variables were tested, each repeated 10 times. The variables include a solid size of 30 mm, initial batch concentration (26% or 55%), and initial batch height (10 cm or 20 cm). Consequently, the batch weight varied across test types, which should be considered when interpreting the results.

Details of the individual tests are provided in Appendix F. The summarized results of these tests are presented in Figure 5.3 using a stock chart. The results of the 30 mm POM sphere tests do not indicate a clear trend. As shown in 5.3, a batch height of 10 cm does not consistently result in a higher or lower number of retained solids for either density. Similarly, an initial batch concentration of 55% does not consistently lead to more solids being stuck across both batch heights. These findings suggest that the influence of these variables on retention behavior is inconclusive within the tested range.

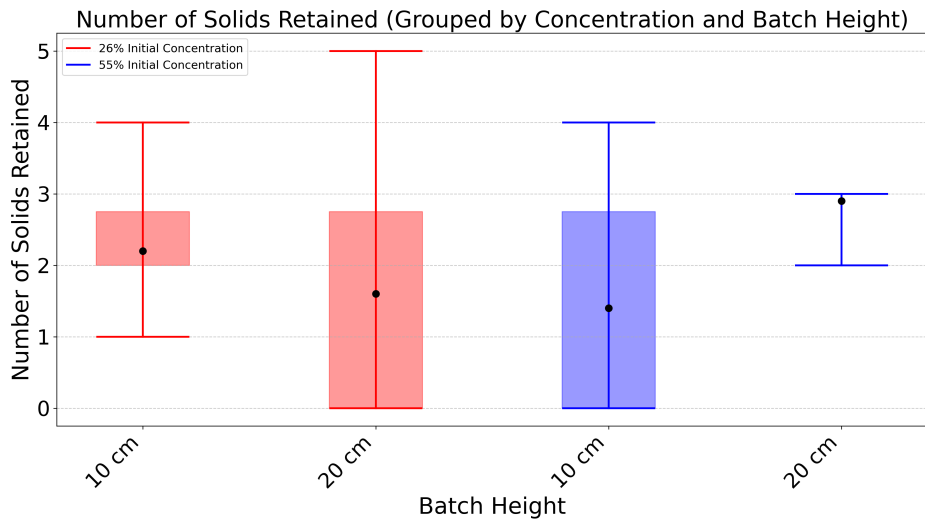


Figure 5.3: Test results for Pump One with 30 mm POM spheres.

To better understand the observed retention behavior, a heatmap was created by analyzing video data to identify entrapment locations, focusing on the Y-coordinate due to the pump's 360-degree symmetry. The heatmap results, shown in Figure 5.4, reveal three distinct heights: $Y_1 = 9$, $Y_2 = 7.5$, and $Y_3 = 3.5$.

The first location, at height 9, corresponds to the diffuser support and indicates a distinct retention mechanism. As discussed in Chapter 2.4, this location is identified as a potential blockage point. Interestingly, retention occurs solely at the upper diffuser support and not at the lower diffuser supports. A plausible explanation is that the solids arrive at the upper diffuser support in concentrated clusters, resulting in a higher arrival concentration, whereas the solids are more uniformly distributed at the lower diffuser supports. This hypothesis is substantiated by video footage. This distribution likely explains the reduced retention observed at these lower supports.

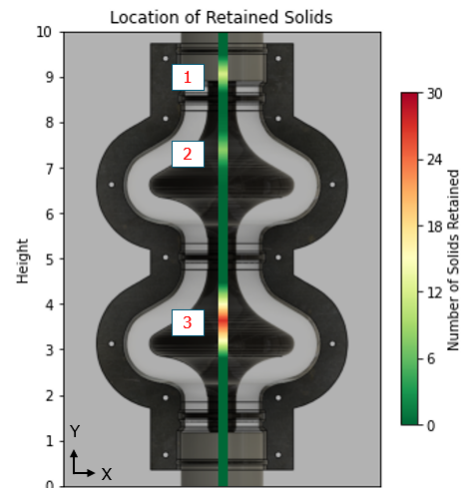


Figure 5.4: Solid entrapment locations from tests, summarizing results from a total of 40 tests.

Focusing on locations 2 and 3, these heights correspond to diffuser 1 and 2, where the geometry of the pump is identical. This uniformity makes similar blockages at these locations predictable. However, since the spacing in the pump is designed to be consistent throughout the model pump, spacing alone cannot fully explain why solids become stuck specifically at these points and not at others. This suggests that additional factors are influencing the outcome.

Spacing

Entrapment could be caused by inconsistent spacing between the solids and the pump core. While the pump is designed for uniform spacing of 30.4 mm, localized deviations may occur due to minor misalignments or variations in the solid size. The PET-G pump housing has a maximum tolerance of 1 mm, meaning the actual spacing can vary slightly from the design specifications. Additionally, it cannot be ensured that the pump core is perfectly centered and suspended within the housing.

Analysis of the video recordings and test notes reveals solids became stuck due to incorrect spacing. This indicates that the spacing in certain areas of the pump housing does not meet the design specifications. These inconsistencies in spacing likely contribute to the entrapment, as they create regions where the solids cannot pass through freely.

Friction

Following the blockage, it was investigated whether the solids at the location were sliding or rolling before becoming trapped. The angle relative to the horizontal at this point was identified as the smallest within the pump geometry. To isolate the effect of the friction coefficient between the solids and the pump core on the entrapment process, a calculation was performed under controlled assumptions. Detailed information about this calculation, including parameters and methodology, is provided in Appendix I.

The results showed that the net force along the surface remained positive, indicating that solids slide along the pump wall rather than coming to rest due to friction. Video footage further confirmed that solids initially slide and then become trapped due to insufficient spacing in the geometry.

Velocity

This explanation does not fully clarify why fewer solids become trapped in Stage one compared to Stage two. One possible explanation is the particle velocity. At higher velocities, the momentum may allow particles to overcome narrowing sections, but the pump geometry likely causes deceleration, making passage through these restrictions more difficult.

The velocity was analyzed by tracking the movement of solids through both stages using video footage. The results show that the velocity in Stage two is lower than in Stage one, which supports the hypothesis that reduced velocity contributes to the increased entrapment in Stage two. This reduced velocity can be attributed to two primary physical mechanisms: the complex pump geometry, which includes multiple bends that cause momentum loss, and the d_{solid}/D_{gap} ratio.

When solids enter the pump at the inlet, they typically have the highest velocity, referred to as the arrival velocity ($v_{arrival}$), driven by their descent through the fallpipe. Upon entering Stage one, this velocity begins to decrease. The deceleration is caused by frequent interactions between the solids and the pump surfaces, as well as the resistance induced by the pump geometry, particularly in sections with bends. These features cause significant momentum loss through friction. Collisions between moving and lodged particles were observed. When a moving particle dislodges a lodged particle, it often becomes lodged itself in the same location.

The second major factor is the d_{solid}/D_{gap} ratio, which represents the relationship between the particle diameter and the internal spacing of the model pump. When the d_{solid}/D_{gap} ratio is close to one, the particles experience a more substantial influence from the surrounding fluid flow. This increases the drag force acting on the particles, leading to a more rapid loss of momentum and further reducing their velocity. Research, as detailed in Appendix G, indicates that this can have a significant effect.

These mechanisms collectively cause a lower particle velocity in Stage two, which impacts the pump's ability to transport solids efficiently and increases the risk of entrapment. While friction does not appear to be a primary factor, spacing inconsistencies and reduced velocity, caused by momentum loss, play significant roles in solids becoming trapped. In a full system with 21 stages, the cumulative effects of these mechanisms could exacerbate entrapment further.

Polydisperse Batch

The second part of this series focuses on investigating whether blockages also occur in a polydisperse batch. According to Section 2.4, polydisperse batches are expected to result in a higher likelihood of blockages compared to monodisperse batches.

However, it is also possible that the presence of smaller solids could help improve flow by dislodging stuck 30 mm solids through collisions. In monodisperse 30 mm batches, similar collisions were observed, but the dislodged solids often became stuck again as the energy from the collision was transferred to the previously lodged solids. This phenomenon does not apply to smaller solids, which cannot geometrically lodge independently.

Of the 26 tests conducted with polydisperse batches, solids became stuck in only three cases, representing a significant improvement compared to the monodisperse tests. Video analysis confirms that collisions between the 30 mm particle and smaller particles help dislodge stuck particles, improving the overall flow. Notably, blockages caused by overtaking between solids of different sizes did not occur. The individual results of these tests can be found in Appendix F, and a summary is presented in table 5.3. The table shows control tests with 3000 (g) solids were also conducted to determine if significant differences would arise, but no notable changes were observed.

Table 5.3: Summary of results showing blockages for different solid sizes under layered and mixed conditions

Solid Sizes (mm)	1500 g		3000 g	
	Layered	Mixed	Layered	Mixed
10, 20, 30	1\5*	1\5	0\1	-
10, 14, 20, 25, 30	1\5	0\5	0\5	-

Note: * Indicates results with significant deviations or observations requiring further analysis.

Discussion Series B2

Retention behavior in the model pump is primarily influenced by particle size. Tests with 30 mm solids revealed consistent blockages at specific locations, particularly near diffusers one and two. Analysis identified reduced spacing and lower particle velocities at these points as key contributors to entrapment, while friction was not found to play a significant role.

Polydisperse batch tests showed an improvement in flow behavior. Collisions between smaller particles and retained 30 mm solids effectively reduced blockages, with retention observed in only three of 26 tests. These findings suggest that incorporating smaller particles into the flow can enhance pump performance by facilitating the release of larger solids.

The main objective of ensuring that solids up to the solid passage diameter pass through the pump without blockages has been achieved, as solids up to 25 mm were successfully handled. The model pump has proven suitable for handling the minimum nodule size, and tests with 30 mm solids provided valuable insights for optimizing flow dynamics under more challenging conditions.

5.4. Series B3: Shortened Fallpipe

In this series, the fallpipe above the model pump was shortened to create a less dispersed batch of solids, resulting in a higher arrival concentration upon reaching the pump. This modification aimed to investigate the effect of increased arrival concentration on the system performance. The higher arrival concentration led to a reduced settling velocity due to the increased hindered settling effect, and thus also to a lower arrival velocity. For 30 mm POM spheres, three tests were conducted with a monodisperse batch (55% initial concentration, 10 cm height) and a 45 cm distance from the solid dispenser to the pump inlet.

The results showed a significant increase in the mean number of retained solids, rising from 1.4 solids per test with the original fallpipe to 8.3 solids per test with the shortened fallpipe. This suggests that a higher arrival concentration and lower arrival velocity at the pump inlet significantly impact retention.

Test footage revealed a higher frequency of blockages at the diffuser supports. These blockages were no longer confined to the upper diffuser support but were also observed at the middle and lower diffuser supports. This change is attributed to the increased number of solids attempting to pass through the diffuser supports simultaneously, as the solids are now more concentrated and less effectively dispersed. A visual representation of how the cluster arrives at the second diffuser support is shown in Figure 5.5a, and the resulting blockages are illustrated in Figure 5.5b.

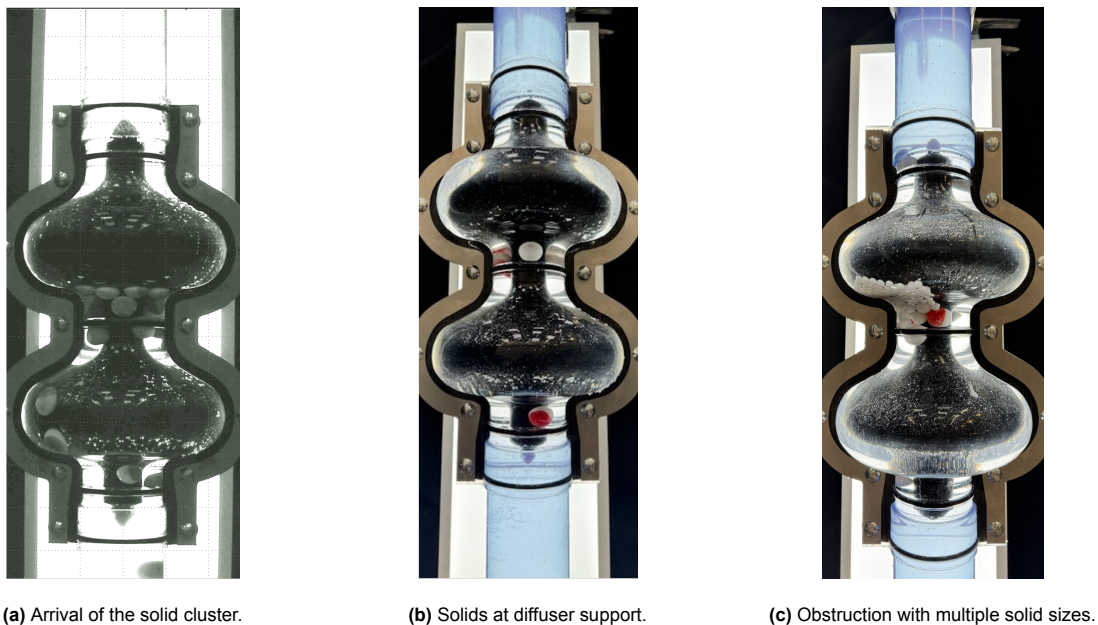


Figure 5.5: Results showing various issues: (a) Arrival of the solid cluster, (b) Solids retained at diffuser support, and (c) Obstruction with multiple solid sizes.

Given this significant increase, additional checks were performed to ensure that 20 mm and 25 mm solids continued to pass through the model pump without issues. Two control tests for each diameter confirmed that these smaller solids could easily pass through. A summary of the test results can be found in Table 5.4.

Table 5.4: Summary of retained data for POM spheres, categorized by size, density, and initial concentration, including the amount retained in grams and percentage.

Size (mm)	Density Solid (kg/m ³)	Repetitions (-)	Initial Concentration (%)	Amount (g)	Retained (g/#)	Retained (%)
30	1400	3	55	599	157.58 / 8.33	26.31
25	1400	2	55	599	0.00 / 0.00	0.00
20	1400	1	55	1200	0.00 / 0.00	0.00
30	2400	5	55	1019	105.31 / 3.20	10.33
30	2400	5	26	478	26.33 / 0.80	5.51

In the second series, tests with polydisperse batches demonstrated improved throughput. For comparison, three tests were conducted using the same batch but with the shortened fallpipe configuration. The higher arrival concentration of the mixture led to the formation of obstructions. Previously, only 30 mm solids became retained; however, with the now increased arrival concentration, smaller solids also became entangled with lodged 30 mm solids, contributing to partial blockages. Figure 5.5c shows an example of this obstruction. Unfortunately, the weight of the obstruction was not recorded, resulting in incomplete data.

In Series B2, only 3 out of 26 tests with polydisperse solids resulted in obstructions, involving no more than three large solids. In contrast, all three tests with the shortened fallpipe resulted in significant obstructions involving at least four large solids and numerous smaller ones. This marked the first instance in this test series where an actual obstruction formed within the pump, aligning with predictions from 2.4, where smaller solids were expected to lodge between larger solids, eventually creating a blockage.

Glass spheres were excluded in Series B2, as previous tests indicated these solids did not remain in the model pump. However, based on the shortened fallpipe results, a series of tests with glass spheres was conducted. Table 5.4 presents the outcomes, showing that glass spheres now remain in the model pump, confirming the effect of increased arrival concentration. To verify this, a repeat test with an initial batch concentration of 26% was conducted, showing fewer solids became lodged under these conditions. These results confirm that arrival concentration plays a critical role in solid retention.

Discussion Series B3

The Series B3 results highlight the critical role the arrival concentration for retention. Shortening the fallpipe increased the average number of retained 30 mm POM spheres from 1.4 to 8.3 solids (Table 5.4). This rise is attributed to the higher arrival concentration of solids at the pump.

Blockages were observed not only at the upper diffuser support but also at the middle and lower supports, caused by the increased number of solids passing through simultaneously. Additionally, glass spheres, previously not retained, were now lodged in the pump. Repeat tests with a lower initial batch concentration confirmed that retention decreases with reduced inlet concentration, emphasizing its significance in retention behavior.

5.5. Conclusion: Pump Without Blades

The experiments with Pump One, without blades, revealed insights into the behavior of solids and flow assurance challenges.

In **Series B1**, the key variable identified was solid size, which emerged as the primary factor influencing retention. Solids with sizes up to 25 mm passed through the pump without blockages, whereas solids measuring 30 mm consistently caused retention, particularly in regions with inadequate spacing.

Series B2 provided an in-depth analysis of the retention behavior of 30 mm solids. Key findings included identifying specific retention locations, such as diffuser one and diffuser two, influenced by geometric factors and velocity reduction. Polydisperse batches showed improved throughput compared to monodisperse batches, as smaller solids dislodged larger retained particles.

In **Series B3**, the shortened fallpipe configuration increased the arrival concentration of solids at the pump, leading to significantly higher retention rates. This series demonstrated the critical role of arrival concentration in retention and blockages, particularly at the diffuser supports. The advantages of polydisperse batches observed in series B2 diminished under these high-concentration conditions.

6

Pump With Blades Experiment

6.1. Introduction

This chapter focuses on testing the geometry of a complete pump model, including the blades, by examining the three-dimensional dynamics of the physical processes occurring within the pump. The objective is to investigate how blade geometry influences reflux, identify conditions that lead to blockages, and explore potential design improvements to enhance flow assurance during reflux.

In the previous chapter, blockages were documented by counting the number of solids that became obstructed, as the quantities were relatively small. However, in this chapter, throughput is measured instead, as this method is more reliable and appropriate for documenting larger quantities. It is important to note that the ball passage diameter of the pump with blades is 25.83 mm, smaller than the 30.4 mm ball passage of the pump without blades. This discrepancy is not due to a specific reason but rather due to limitations in the provided 3D model. As a result, the solid passage diameter is 20.5 mm.

This chapter presents the results of the experiments, structured into three research series: **Series C1: Initial Evaluation**, **Series C2: Performance Analysis**, and **Series C3: Adjusted Blades**.

Series C1 investigates the reflux performance of the pump with monodisperse batches, isolating the influence of solid size, concentration, and batch height. These initial insights establish a foundation for understanding blockage mechanisms.

Building on these findings, **Series C2** examines the influence of polydisperse batch compositions, focusing on size distribution. This series maps the processes causing blockages and identifies critical performance limitations.

In **Series C3**, adjustments to the impeller blades are tested to address the identified bottlenecks and improve reflux performance.

The chapter concludes with an integrated discussion of the results, providing a comprehensive understanding of solids behavior and their impact on the pump's performance.

6.2. Series C1: Initial Evaluation

This first series is used to examine how key variables, particle density, particle size, initial batch concentration, and batch height, affect clogging. This systematic approach aims to identify the factors influencing flow assurance and provides valuable insights into the underlying mechanisms of clogging. Tests were conducted with monodisperse solid batches of glass and POM spheres, with initial concentrations of 26% and 55%, batch heights of 10 cm and 20 cm, and particle sizes of 10 mm, 14/15 mm, 20 mm, and 24/25 mm.

Each variable combination was tested once for both solid densities, except for the combination of glass spheres, 25 mm, 55% initial batch concentration, and 20 cm height, which was omitted due to insufficient material availability. An overview of all tests conducted is found in Table 6.1

Table 6.1: Overview of Tests Conducted in Series C1

Test Matrix			
Density	Solid Concentration	Batch Height	Solid Diameters
2400 kg/m ³	26%	10 cm	10 mm, 14 mm, 20 mm, 25 mm
		20 cm	10 mm, 14 mm, 20 mm, 25 mm
	55%	10 cm	10 mm, 14 mm, 20 mm, 25 mm
		20 cm	10 mm, 14 mm, 20 mm
1400 kg/m ³	26%	10 cm	10 mm, 15 mm, 20 mm, 24 mm
		20 cm	10 mm, 15 mm, 20 mm, 24 mm
	55%	10 cm	10 mm, 15 mm, 20 mm, 24 mm
		20 cm	10 mm, 15 mm, 20 mm, 24 mm

Results and Observations

Figure 6.1 provides a visualization of the test outcomes, with 100% throughput set as the target. This visualization highlights the variable combinations that have the most significant impact on pump performance. Appendix H contains the results and final input data for each test.

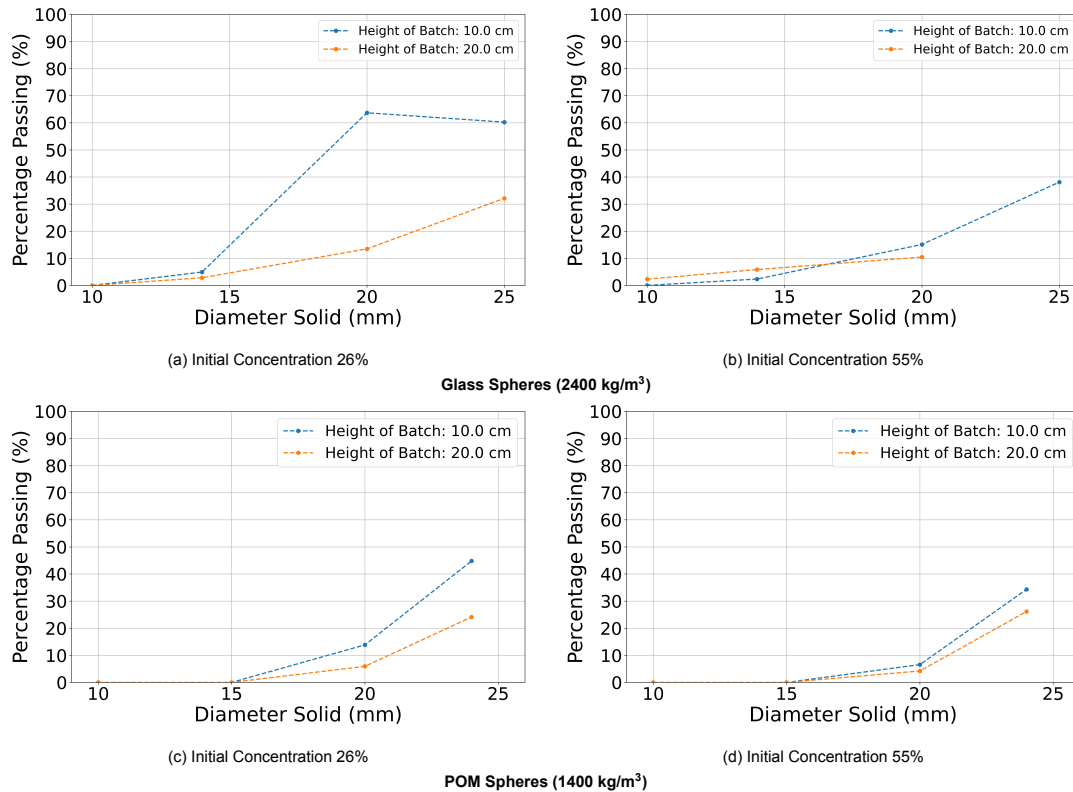


Figure 6.1: Comparison of throughput at initial batch concentrations. The results are shown for glass spheres and POM spheres.

- **Effect of Batch concentration:** An initial batch concentration of 26% consistently outperformed 55%, enabling smoother flow by reducing particle interactions and collisions.
- **Influence of Batch Height:** A batch height of 10 cm generally resulted in a higher throughput compared to 20 cm.
- **Performance of Smaller Solids:** Solids with a size of 15 mm or smaller showed minimal to no throughput under all test conditions.
- **Impact of Solid Size:** Throughput percentage increased significantly with larger particle sizes.

For both materials, blockages are observed at the end of the impeller blades, where solids accumulate along the edge, forming a compacted build-up of material. This is the critical accumulation point, particularly for solids up to 15 mm. Significant blockages occur in the first stage, with minimal progression beyond this point. Figure 6.2 shows these blockage locations for glass solids, with similar patterns observed for POM solids. For solids measuring 20 mm and larger, flow shows slight improvement, with more solids progressing through the stages. However, significant blockages remain at the end of the impeller blades, and in some cases, these extend further into the diffuser.

A second type of blockage is only observed with POM solids, where obstructions occur within the diffuser vanes. These blockages are characterized by jamming of smaller particles, as shown in Figure 6.3. This blockage is not seen for glass spheres and no longer occurs for POM solids measuring 20 mm and larger. These types of blockages will be discussed one by one after examining the processes that lead to their formation.

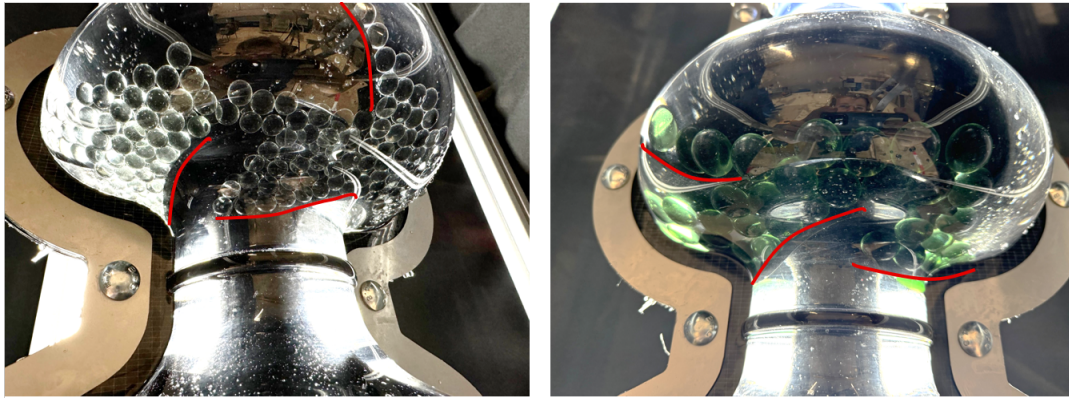
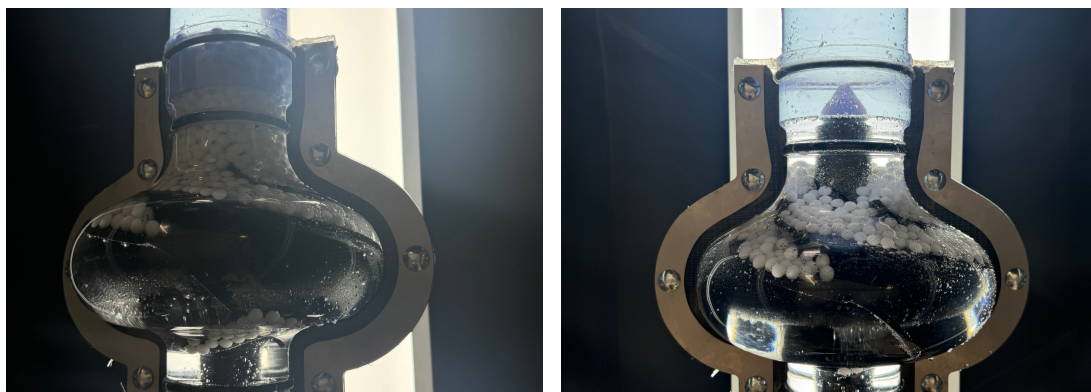


Figure 6.2: Comparison between 10 mm and 20 mm solid obstruction



(a) Obstructions at Diffuser Vanes and Impeller

(b) Close-up of Diffuser Vane Obstruction

Figure 6.3: Diffuser Vanes Obstructions.

Discussion Series C1

In the following sections, the specific blockage mechanisms, including impeller and diffuser obstructions, and the effects of particle size, batch configuration, and friction, will be discussed in detail.

Pump Arrival Concentration For both densities, the best test results were achieved with the lowest arrival concentration upon entering the pump: a batch height of 10 cm and an initial batch concentration of 26%. This outcome can partially be explained by examining the flow regimes and how they are influenced by increased volume concentration.

When the solids settle in the fallpipe, a two-way interaction regime is observed, where the particles and the fluid flow mutually influence each other. Upon reaching the pump, the flow becomes restricted due to the geometry, leading to increased particle-particle collisions. This marks the transition to a particle-collision-dominated regime, where the number of collisions increases as the particles move further through the vanes and the available space decreases.

As the arrival concentration increases, frequent interactions, including collisions and wall contacts, progressively dissipate momentum. This dissipation is primarily caused by friction, which reduces the momentum of solids. Friction arises from:

- **Particle-particle friction:** When particles collide or remain in contact, frictional forces are generated between their surfaces. These forces resist motion and reduce the momentum of the particles.
- **Particle-wall friction:** Particles in contact with the walls of the system experience resistance due to the surface roughness and material properties of the boundary. This effect becomes more significant in confined flows, such as risers, where particles often accumulate near the walls.

As momentum is dissipated through frictional interactions, the batch transitions into a contact-dominated regime. In this regime, frequent, short-lived collisions give way to prolonged interactions between particles and the surrounding walls, with friction becoming the primary factor governing particle dynamics.

Solid Size The size of particles plays a critical role in surface contact and resistance during transport. Smaller particles, with a higher surface-to-volume ratio, generate more friction due to increased particle-particle collisions and particle-wall contact. Larger particles experience reduced friction but generate higher impact forces during collisions due to their greater mass. At higher arrival concentrations, these interactions intensify as more particles attempt to pass through the pump, increasing resistance and transitioning the system into a contact-dominated regime. At lower arrival concentrations, the reduced number of interactions allows for a more uniform flow through the pump. This minimizes frictional losses and prevents the system from transitioning into a contact-dominated regime.

When scaling the system to nodules, the surface area becomes an even more critical factor. Irregular shapes significantly increase the contact area compared to spherical particles, amplifying frictional interactions and flow resistance.

Role of Friction and Slope As observed in Chapter 5, the angle at which the solids propagate significantly influences their behavior. In the diffuser, reduced slopes (as low as 10%) increased friction force and lower the gravitational component of the driving force. This uneven distribution of forces lowers the momentum of the solids. The reduced momentum of the solids increases the likelihood of jamming, as the lower force is insufficient to overcome frictional resistance. The prolonged interaction between solids and the blade surface further amplifies the effects of static and dynamic friction.

Impeller Barrier Blockage The first type of blockage occurs at the end of the impeller blades. Analysis of the test footage reveals a backward accumulation of solids, schematically depicted in Figure 6.4, with the blade highlighted in red and the solids in green. The curvature of the blade creates a "barrier effect" at the end of the impeller blade. This accumulation leads to the formation of an upward-growing obstruction.

When single solid batches are used, the solids do not become retained at this location. This is because single solids lose significantly less momentum while passing through the pump compared to solids in a batch, where particle-particle interactions result in additional momentum dissipation. These interactions, combined with the frictional effects discussed earlier, exacerbate the barrier effect and increase the likelihood of blockage. A minimum amount of momentum is required for solids to overcome friction at critical points, such as at the tip.

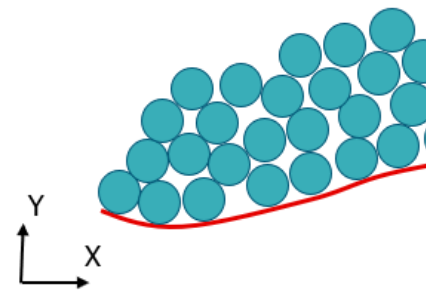


Figure 6.4: Impeller barrier blockages.

Vanes of the Diffuser Obstruction The second type of blockage occurs within the diffuser vanes and is observed only for POM spheres. This obstruction exemplifies how flow regime, particle interactions, friction, drag, slope, and the narrow vane geometry combine to create jamming of the solids.

As illustrated in Figure 6.5, the process begins with solids slowing down due to interactions with one another and the blade and house surface. This reduction in movement causes particles to move over each other, increasing friction against the wall. The schematic uses dark blue to indicate solid accumulation, while light blue highlights the slowing effect of particle interactions on their movement. Smaller particles near the wall face more resistance than those at the center, causing overtaking and influencing particle distribution and interactions.

The obstruction is observed exclusively with particles of 10 mm and 14/15 mm. Larger solids (greater than 20 mm) cannot align side-by-side within the narrow vanes, preventing jamming and enabling them to pass through in a single-file manner. Glass spheres are believed to retain sufficient momentum to overcome frictional forces in this series of the diffuser.

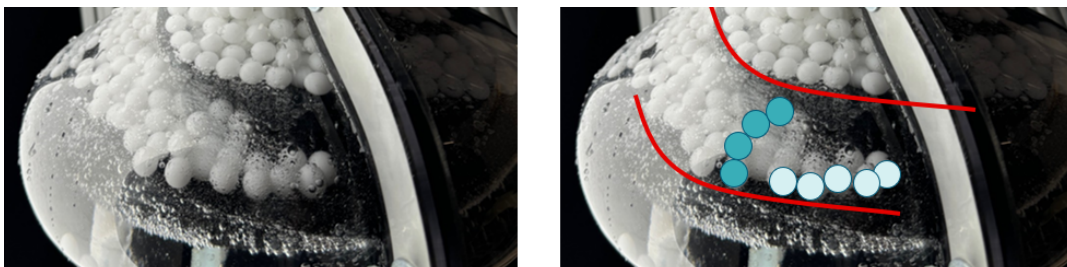


Figure 6.5: Diffuser vanes blockages.

6.3. Series C2: Performance Analysis

During this series, three different types of solid size combinations will be tested to evaluate the impact of solid size distribution on performance.

- **Type 1:** 10 mm, 14/15 mm, and 20 mm, with each size contributing 33% of the total batch weight.
- **Type 2:** 10 mm, 17 mm, and 25 mm, with each size contributing 33% of the total batch weight.
- **Type 3:** 10 mm, 14/15 mm, 17 mm, 20 mm, and 24/25 mm, with each size contributing 20% of the total batch weight.

The first two combinations are designed to evaluate the impact of larger solids within the mixture. The maximum ball passage diameter of the pump blades is 25.83 mm, with a corresponding maximum solid passage diameter of 20.5 mm. It is essential to evaluate whether the pump can reliably handle solids exceeding this size. In this series, tests will be conducted with solids larger than the solid passage diameter, based on the findings from Series C1, which demonstrated that solids up to 24/25 mm could successfully pass through the vanes.

The third combination investigates whether reducing the size differences between solids increases the likelihood of blockages. This hypothesis suggests that smaller solids may settle into the gaps between larger ones, impeding flow and potentially leading to obstructions. An overview of the tests that are conducted in this series is shown in Table 6.2.

Table 6.2: Overview of Tests Conducted in Series C2

In-depth Analysis			
Density	Batch Weight	Configuration	Batch Type (Repetitions)
2400 kg/m ³	1500 g	Mixed	Type 1 (5), Type 2 (5), Type 3 (5)
		Layered	Type 1 (5), Type 2 (5), Type 3 (5)
	3000 g	Mixed	Type 1 (4), Type 3 (3)
1400 kg/m ³	878 g	Mixed	Type 1 (3), Type 2 (3), Type 3 (3)
		Layered	Type 1 (3), Type 2 (3), Type 3 (3)
	1750 g (1)	Mixed	Type 1 (1)

Results and Observations

The averages for the glass and POM spheres are visualized in the stock charts in Figure 6.6, with the y-axis extending to 20% to display the throughput values. For both spheres, throughput remained consistently low, with glass spheres showing the highest averages.

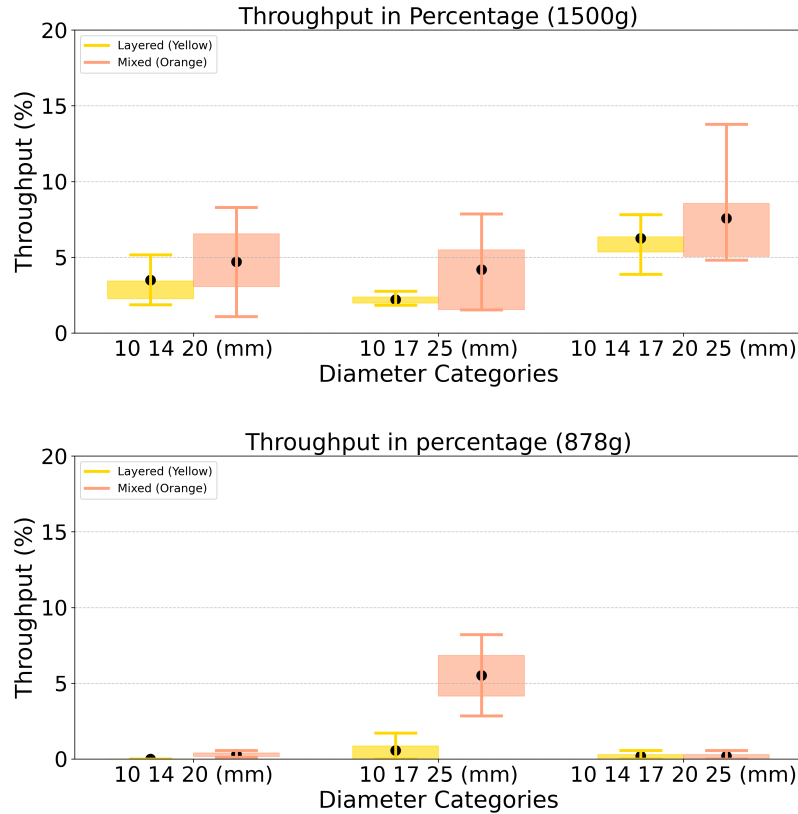


Figure 6.6: Throughput for all batch types: the upper graph represents glass spheres, and the lower graph represents POM spheres.

- **Mixed Batches vs. Layered Batches (Glass):** Mixed batches exhibit a higher average throughput for each size type compared to layered batches.
- **Comparison Between Type 1 and Type 2:** For glass spheres, Type 1 and Type 2 show minimal differences. While Type 1 has slightly higher throughput for both mixed and layered configurations, the maximum difference of 1.7% is negligible and does not indicate a significant trend. In the case of POM spheres, Type 2 (mixed batch) demonstrates slightly better performance compared to the other types.
- **Performance of Type 3 Solids:** For glass spheres, Type 3 has the highest throughput, though it remains very low overall.
- **Formation and Locations of Blockages:** Blockages for glass spheres form at the end of the impeller, where solids accumulate and create obstructions. For POM spheres, blockages occur in two key locations: at the end of the impeller blade and within the diffuser vanes.

A summary of all tests conducted with glass and POM spheres during this series is provided in Appendix H. The Appendix offers a clear and comprehensive overview of all performed tests, including the results of the tests with double the weight. These tests were conducted to investigate whether increased weight exacerbated clogging, which was indeed confirmed.

Series Discussion

The results of the experiments highlight significant challenges in achieving effective throughput with the tested configurations for both glass and POM spheres. Across all tests, throughput remained critically low, with consistent blockages forming at key locations in the pump. For both materials, obstructions commonly occurred at the end of the impeller blade, where solids of various sizes accumulated and prevented further flow. Even relatively small solids lodged in this location prevent larger solids from passing, as shown in Figure 6.7. The obstruction at the end of the impeller blades is particularly concerning, as it consistently caused significant blockages in every test.

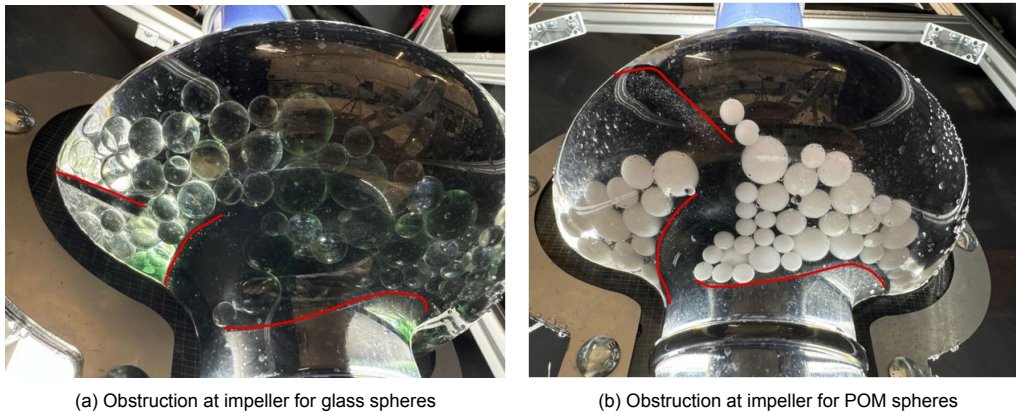


Figure 6.7: Comparison of impeller obstructions for glass spheres and POM spheres.

For glass spheres, mixed batches performed slightly better because larger solids settled at the front. When larger solids were positioned higher in the layered batch, they had to overtake smaller particles, increasing resistance and reducing throughput. Examining the composition of the three Types of batches, types 1 and 2 showed little variation, suggesting that the presence of individual solids larger than the pump's designed solid passage diameter does not significantly affect performance. This finding is important, as it indicates that occasional oversized solids entering the pump are unlikely to cause significant issues.

For POM spheres, throughput was almost negligible across all configurations, with one minor outlier for Type 2 showing a throughput of 5.5%. However, this result does not provide meaningful insights. Blockages for POM spheres formed not only at the impeller blade but also within the diffuser vanes. These blockages were exacerbated by segregation in polydisperse batches, where differences in particle size and density caused solids to separate along the flow path due to variations in drag and momentum. Larger particles migrated toward the front of the batch, while smaller particles accumulated around them, increasing friction and particle interactions. In contrast, monodisperse batches, lacking size variation, resulted in less frequent obstructions. The lower particle inertia of POM spheres likely contributed to the more severe blockages observed in the diffuser, as no such blockages were seen with glass spheres.

The findings underscore the need for modifications to the pump design, particularly at the impeller blade and diffuser vane locations. Minor modifications to the impeller blade design could mitigate blockages. Series Three will focus on design changes to address these issues.

6.4. Series C3: Adjusted Pump

Series C3 investigates the effect of design modifications to the pump blades, focusing on mitigating the bottlenecks identified in the previous series. By implementing targeted adjustments, this series aims to evaluate their effectiveness in reducing blockages and improving flow assurance during reflux. The results and observations from these tests will be discussed after outlining the specific modifications made to the pump.

From the analyses in Series C1 and C2, the impeller entry was identified as the most significant challenge for flow assurance during reflux. To address this, a small portion of the impeller material was grind off, as shown in Figure 6.8. This modification was applied to all impeller blades on both impellers.

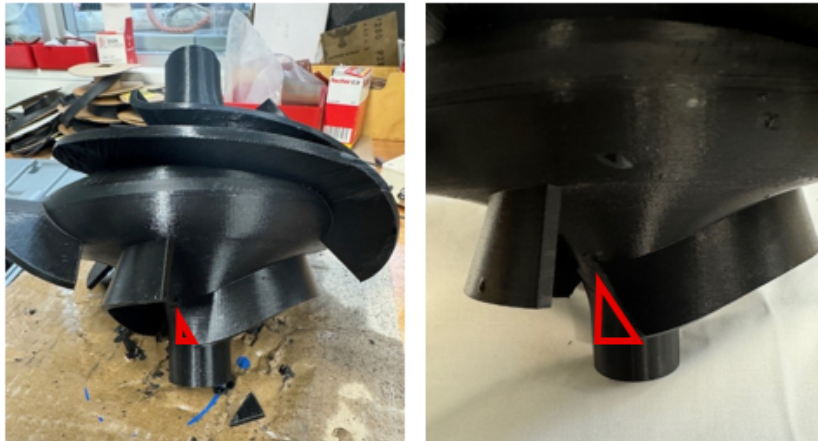


Figure 6.8: Impeller blades adjustment.

By resolving this key issue, the adjustments establish a foundation for a more reliable pump design during reflux. However, the material removed from the impeller blades to mitigate blockages during reflux introduces trade-offs in performance under standard operating conditions. This modification alters key design parameters which can reduce the efficiency of energy transfer and overall pump performance. Future designs should carefully evaluate these parameters, as discussed in Section 2.3, to minimize efficiency losses and ensure the pump meets the required performance under both reflux and normal operation.

In this series, the pump with the adjusted impeller blades will be tested. For POM spheres, the tests will follow the same bed configurations as in Series C2 of the experiment, specifically:

- **Type 1:** 10 mm, 14/15 mm, and 20 mm, with each size contributing 33% of the total batch weight.
- **Type 2:** 10 mm, 17 mm, and 24/25 mm, with each size contributing 33% of the total batch weight.
- **Type 3:** 10 mm, 14/15 mm, 17 mm, 20 mm, and 24/25 mm, with each size contributing 20% of the total batch weight.

For glass spheres, only Type 3 will be tested due to time constraints. Among the three types, this configuration is considered the most promising. An overview of all test configurations can be found in 6.3.

Table 6.3: Overview of Tests Conducted in Series C3

Adjusted Blades			
Density	Batch Weight	Configuration	Batch Type (Repetitions)
2400 kg/m ³	1500 g	Mixed	Type 3 (5)
		Layered	Type 3 (5)
	3000 g	Mixed	Type 3 (3)
1400 kg/m ³	878 g	Mixed	Type 1 (3), Type 2 (3), Type 3 (5)
		Layered	Type 1 (3), Type 2 (3), Type 3 (5)
	1750 g	Mixed	Type 3 (3)

Results and Observation

The individual results for both materials are detailed in Appendix H. The average results for glass spheres are presented in Figure 6.9, while the comparison for POM spheres is shown in Figure 6.10.

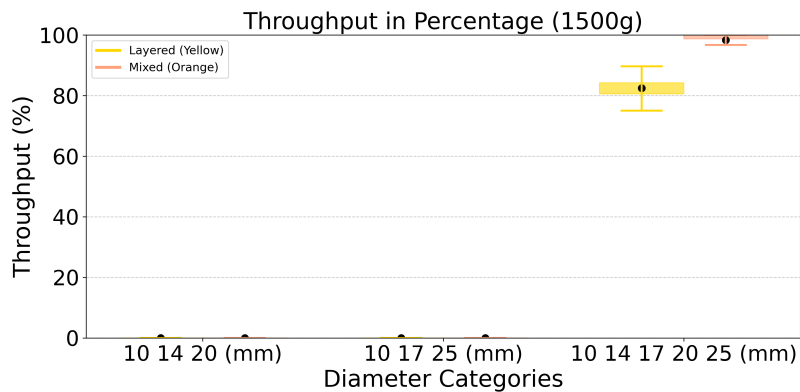


Figure 6.9: Results for Type 3 glass spheres (10, 14, 17, 20, and 25 mm). Only Type 3 is shown as other types were not tested.

For glass spheres, mixed batches achieved a throughput percentage of 98%, reflecting an almost complete reflux of the batch. Imaging confirmed the absence of obstructions, with only a few isolated solids remaining in the pump. These results demonstrate that the adjustment to the impeller blades was highly effective, significantly enhancing the system's performance during reflux. For layered batches, the throughput percentage was slightly lower at 82.5%, with visible obstructions occurring at the transition from the diffuser to the impeller and within the diffuser vanes.

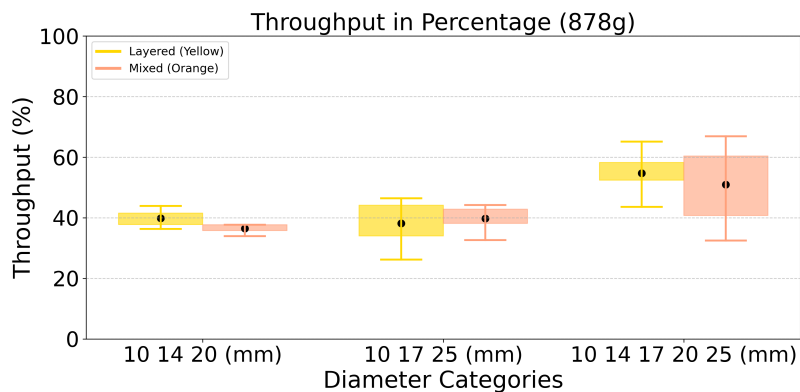


Figure 6.10: Results for all types with POM spheres.

The results for POM spheres show an improvement compared to Series C2 but remain lower than for glass spheres. The highest average throughput, recorded for Type 3 batches, was 59.8%. The following key observations were made:

- **Improvement Compared to Series C2:** Performance improved across all configurations compared to Series C2.
- **Similarity Between Type 1 and Type 2:** Throughput for Types 1 and 2 showed minimal differences, indicating similar performance.
- **Mixed vs. Layered for Type 1:** For Type 1, layered batches outperformed mixed batches for the first time, deviating from previous trends.
- **Slightly Better Performance of Type 3:** Type 3 consistently achieved slightly higher throughput compared to the other types.

Observed Blockages

- **Impeller Blade Entry:** Blockages at the impeller entry were significantly reduced, occurring in only two cases. This demonstrates the effectiveness of the modifications made to the pump.
- **Diffuser Vanes:** New blockages were identified in the diffuser vanes for glass spheres. Although these occurred infrequently, they represent a notable new observation compared to previous series.
- **Transition Between Diffuser and Impeller:** A new blockage point was observed at the transition between the diffuser and the impeller. This type of obstruction occurred frequently during this series, as shown in Fig.6.11(a).
- **Pump Housing Connection:** Blockages were also identified at the connection between the two halves of the pump. These blockages, illustrated in Fig.6.11(b), were linked to the internal edges at the joint.

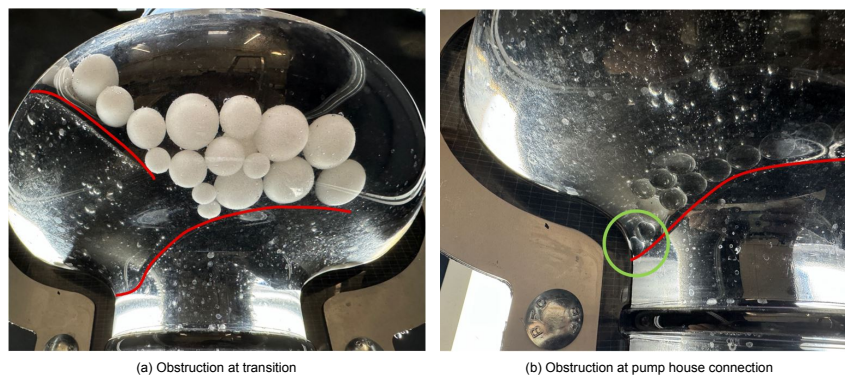


Figure 6.11: Visualization of obstructions: (a) Transition between diffuser and impeller and (b) Connection between pump halves.

Series Discussion

Obstructions Series C3 testing has revealed four distinct blockage locations within the pump system. These findings expand on earlier observations and highlight new areas where solids accumulate, now that previous issues at the impeller entry have been mitigated. The identified blockage points are discussed in detail below.

Impeller Blade The adjustment to the entry of the impeller blade resulted in a significant improvement in throughput for the solids, especially for the glass spheres, where a 98% passing rate was achieved in some tests. In just two cases, a blockage at the impeller blade was observed.

Vanes of Diffuser Obstruction This type of obstruction was already discussed in Series C1 and C2. In Series C1, the obstruction occurred only with solids of the same size, as the batch was monodisperse. In Series C2, obstructions also occurred with solids of different sizes as the batch composition was mixed. In addition, during Series C2, blockages were observed exclusively for POM spheres. However, in this series, blockages in the vanes of the diffuser also occur for glass spheres. A clear explanation for the absence of obstruction for glass spheres during Series C2 is not available, and the blockages occur irregularly.

Transition Obstruction

The transition blockage from the diffuser to the impeller was not identified as a blockage location in the previous series because solids consistently accumulated on the impeller, covering this transition area. In this series, this location was observed as a new blockage point. Figure 6.11a provides an overview image of an obstruction at this location, while Figure 6.12 illustrates how this blockage extends upward along the diffuser blade.

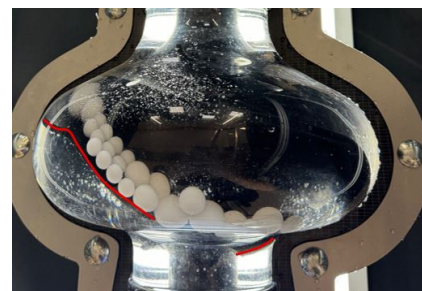


Figure 6.12: Extension of the blockage upward along the diffuser blade.

Figure 6.13 illustrates an animation sequence showing how this blockage develops. The steps are described as follows:

- **Step 1: Initial Movement** In the first step (left image), solids roll off the diffuser blade. Due to this momentum, some solids partially roll up the impeller blade, where they lose speed. They then change direction due to the angle of the impeller blade and roll off the blade again.
- **Step 2: Collision** In the second step, a solid rolling off the diffuser blade collides with another solid moving in the opposite direction from the impeller blade. This collision causes the solids to become jammed.
- **Step 3: Bridge Formation** In the third step, the jammed solids form a bridge, creating a stationary obstruction. No further movement of solids occurs, and the blockage extends into the diffuser blades.

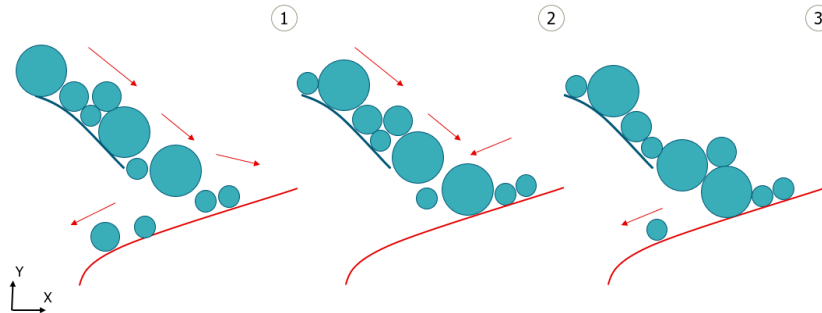


Figure 6.13: Transition Blockage Animation.

Blockage at Connection of Pump Housing The pump housing consists of two parts, which create two internal edges at the points where these sections are joined. This design introduces a potential imperfection in the pump model, as small solids were observed in a few tests to become lodged at these edges. On rare occasions, this led to blockages. To minimize the risk of such issues in real-life, it is important to account for these edges during the design series by ensuring proper tolerances are specified for the joints.

Number of Blockages for POM: Stage One Compared to Stage Two In Chapter 5, it was observed that the velocity of the solids significantly influenced the number of retained particles in each stage. Notably, in the second stage, solids were retained more frequently than in the first stage due to the lower solid velocities.

To further investigate the distribution of blockages in the pump with blades, the number of obstructions at various locations was systematically recorded to determine the most frequent blockage points. These test-specific observations are documented in Appendix H, while the average number of obstructions per type is summarized in Table 6.4. Interestingly, for the pump with blades, the majority of blockages occurred in Stage one, particularly within Diffuser One.

Table 6.4: Summary of average number of blockages for POM spheres at different locations under various configurations.

Situation (-)	Diameter (mm)	Density (kg/m ³)	# Diffuser 1 Vanes	# Transition 1	# Diffuser 2 Vanes	# Transition 2
Avg. Layered	10 15 20	1400	2.2	2.2	0.0	0.8
Avg. Mixed	10 15 20	1400	2.0	1.6	0.2	0.4
Avg. Layered	10 17 24	1400	4.0	0.0	0.0	0.0
Avg. Mixed	10 17 24	1400	2.5	1.3	0.0	0.8
Avg. Layered	10 15 17 20 24	1400	2.2	2.2	1.0	0.0
Avg. Mixed	10 15 17 20 24	1400	2.0	1.7	1.0	1.0

In this case, velocity was not the primary factor influencing the variation in the number of blockages between the stages. Instead, the mixture concentration emerged as the dominant parameter. Upon arriving at Stage one, the mixture arrival concentration is high, which increases the likelihood of blockages. As the solids pass through Stage one, they become more dispersed in the flow. With more space between the solids. As discussed in Section 6.2, this reduction in concentration decreases the likelihood of blockages in Stage two.

Comparison Between Batch Types Based on Size Distribution For POM spheres, a comparison was made between batch types 1 and 2. The throughput percentages showed very similar results. For mixed batches, the maximum average difference was just 3.3%. This initially suggested that the inclusion of larger solids in the batch did not significantly affect throughput. The numbers and locations of blockages recorded in table 6.4 show differences between the two types. This suggests that using batches with larger solids may be less acceptable than what the throughput percentages indicate.

The results indicate that batches with larger solids experienced more blockages in the first diffuser and transition, while few to no blockages occurred in the second transition and diffuser. This suggests that obstructions tend to form early in the process, specifically in the first diffuser, and are more severe when larger solids are present. These findings demonstrate that using batches with larger solids has a greater impact than suggested by the throughput percentages.

When examining Type 3, an improvement in throughput is observed, along with fewer blockages in the first stage compared to Type 2. The number of blockages in the first stage is very similar to that of the Type 1 mixture. This contradicts the assumption that larger solids always have a negative effect on throughput. Two factors should be considered here. First, the more significant variation in particle sizes in the Type 3 batch results in a lower total number of 24 mm solids compared to the Type 2 batch. Second, it is possible that the narrower distribution of solid sizes contributes to a smoother flow, as observed in earlier tests. To rule this out, an additional test should be conducted using a narrower size distribution between 10 and 20 mm to compare the results.

6.5. Take Away: Pump With Blades

Leading up to Blockages

The geometry of the pump causes flow restriction, leading to a transition from a two-way interaction regime to a particle-collision-dominated regime. As the spacing in the vanes decreases, the number of particle-particle and particle-wall collisions increases. These collisions progressively dissipate the momentum of the particles.

A higher arrival concentration of particles leads to more frequent collisions, further accelerating momentum loss. This dissipation occurs primarily due to friction, which, along with drag forces, plays a significant role in reducing the momentum of the solids.

As momentum is dissipated through these frictional interactions, the batch transitions into a contact-dominated regime. Segregation further exacerbates this process by causing particles of different sizes to overtake one another, disrupting the flow. Particle size plays a critical role in surface contact, as smaller particles have a higher surface-to-volume ratio and lower inertia due to their smaller mass.

The angle at which solids propagate significantly influences their momentum. With smaller angles, the gravitational force is reduced. As momentum decreases, the force becomes insufficient to overcome frictional resistance, increasing the likelihood of jamming and bridging.

Blockages

- **Jamming in Diffuser Vanes:**
Due to momentum dissipation and friction, smaller particles get trapped in the diffuser vanes.
- **Impeller Blade Blockage:**
Particles with too low momentum cannot overcome the friction at the impeller blade entry and get stuck. Minor adjustments to the impeller blade improved flow at this location.
- **Bridging at Transition:**
Bridging occurs when particles from different directions get stuck together due to friction, causing blockages in the pump.
- **Connection of Pump Housing** Solids with low momentum can become trapped at the connection of the pump housing due to incorrect tolerances.

7

Practical Implications

7.1. Stages

In this experimental research, the number of pump stages is limited to two. Under normal operational conditions, a single pump would typically consist of seven stages, with three pumps operating in series, resulting in a total of 21 stages. While advancements in pump design are expected to reduce the likelihood of blockages significantly, they cannot be entirely eliminated. Consequently, a system with multiple stages inherently increases the risk of blockages, even if the probability of blockages per stage decreases significantly with improved design.

One important observation from this study is that the first stage significantly reduces the risk of blockages in subsequent stages, particularly for the pump with blades. As discussed in 6.4, Stage 1 redistributes solid particles in such a way that the concentration is reduced before entering Stage 2. This reduction in concentration minimizes the likelihood of clogging in downstream stages, especially under optimized flow conditions. Achieving good flow performance in Stage 1 during testing is therefore critical to further reducing the risk of blockages in subsequent stages. However, as discussed in 5.3, the decreasing velocity of solids within the stages increases the likelihood of blockages.

7.2. Hydrostatic Pressure Difference

When the pump stops, the hydrostatic pressure difference between the inside and outside of the riser causes the nodule-water mixture to descend until equilibrium is reached [48]. While this is a simplified description of the process, it captures the key consequence: the mixture level inside the riser can drop below the external water surface level. This phenomenon has two important implications:

Loss of Counterpressure at the Top of the Riser: As the mixture descends, the upper section of the riser becomes empty, removing the internal counterpressure. This loss of pressure must be carefully managed to prevent the riser from collapsing under external pressure. Allowing water to flow back into the riser is essential to maintaining its structural integrity. In the event of a severe blockage within the pump that prevents the mixture from passing, the descending mixture may create a vacuum beneath the pump. This vacuum can result in a significant pressure difference, potentially leading to structural failure.

Downward Flow of the Mixture: The sinking of the mixture generates a downward flow, which can have both positive and negative effects. Not only the solids but also the water moves downward, creating a continuous flow that may be advantageous compared to the current test conditions, where the system relies solely on the movement of solids without water flow. On the other hand, if a blockage occurs, the water flow could exacerbate the situation by compacting the blockage, making it more severe.

7.3. Connection of Pump Housing

The test setup uses a pump housing consisting of two parts, which creates internal edges where solids can become lodged. In a real pump, the housing consists of more parts, and this must be considered in the design to prevent similar issues. Blockages may still occur, particularly with materials like rubber packings or poor-quality metal manufacturing. It is important to specify tight tolerances with the manu-

facturer and select high-quality production methods. Although higher tolerances come at a cost, they are necessary for ensuring pump reliability. Robust Quality Assurance and Control (QAC) processes must verify tolerances before delivery to avoid operational failures.

7.4. Comparison to Previous Research by OMI:

In Chapter 2, reference was made to the research conducted by OMI, which included a successful scale test using a multi-stage centrifugal pump. This study reported no blockages during reflux. These findings differ from the results of this thesis, while glass spheres achieved a transport efficiency of up to 98%, the throughput for POM solids was significantly lower, reaching only about 58%. This discrepancy necessitates a comparison between the two studies. The OMI paper, published in 1980, provides limited details about the pump, restricting the depth of analysis.

Advantages of the OMI Test Compared to This Thesis:

- **Lower mixture concentration:** The OMI study utilized a significantly lower mixture concentration of 5%. This minimized the risk of blockages and ensured smoother pump operation. In contrast, the higher concentrations considered in this thesis reached up to an initial concentration of 55%.
- **Solid Density:** The density of the nodules is higher than that of the POM spheres. The improved throughput of glass compared to POM indicates that higher density offers an advantage.
- **Larger diffuser slope angle:** The pump in the OMI study was designed with a diffuser slope angle of 40° , positively influenced the reflux. This larger angle facilitated smoother transitions within the pump stages, enhancing the transport efficiency. In contrast, the diffuser slope angle used in this thesis is 30° .
- **Solid Size Distribution:** In this thesis, the PSD was limited to maximal five particle sizes, evenly distributed by weight. During the OMI tests, however, natural seabed nodules were used, with a PSD containing more small than large particles. During transport through the pipeline and pump, larger particles degraded into smaller ones due to mechanical interactions, resulting in a PSD with even fewer large solids and more smaller particles.

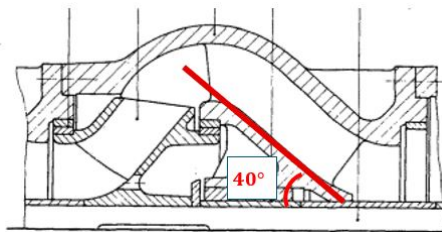


Figure 7.1: Cross-section of the pump stage used by OMI, showing the defined angle as described in [43].

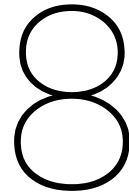
Disadvantages of the OMI Test Compared to This Thesis:

- **Use of irregular nodules:** Unlike the perfect spheres tested in this thesis, the OMI study involved the transport of actual nodules, which are irregularly shaped and more difficult to handle. The irregularity introduces additional friction.

Similarities of the OMI Test Compared to This Thesis:

- **Comparable particle size ratio:** Both the OMI study and this thesis applied a particle size ratio of approximately 1.25.

The OMI paper lacks detailed information regarding critical pump parameters, such as blade angle and stage spacing. This absence of data restricts the ability to conduct a comprehensive comparison of the pump designs and operational settings between the two studies. Insights from other studies, such as those by Q. Hu and L. Yuanwen [13, 10], further emphasize that pump blockages can occur under specific conditions.



Conclusion and Recommendations

8.1. Conclusion

8.1.1. Flow Assurance

The primary objective of this research was to identify and analyze key design vulnerabilities of multi-stage centrifugal pumps that could lead to flow assurance issues in DSM (Deep Sea Mining) operations. The literature review revealed that the highest risks to flow assurance occur during reflux. During reflux, the low velocity of solids, combined with small spacing, the complex geometry of the pump, and the large number of stages, significantly increases the likelihood of blockages.

Experimental investigations identified specific design vulnerabilities within the pump's geometry. At these locations, blockages were observed. By employing batches with varying initial batch concentrations, heights, and size distributions, the influence of batch composition on the occurrence and severity of obstructions was systematically analyzed. Below, the conclusions derived from this analysis are presented.

8.1.2. Blockage Mechanisms

The study identified several distinct blockage mechanisms contributing to obstructions within the pump system. Blockages are typically the result of a combination of mechanisms and variables.

When dealing with single solids, blockages can occur if the solids are too large to pass through the pump's spacing. Furthermore, the associated inertia of the solids plays a crucial role. Smaller solids with low inertia may lack the momentum required to overcome friction at critical locations, such as the impeller blade entry. This can lead to the formation of stationary solids, which act as start point for further blockage. A barrier effect may develop, where a single stationary solid triggers the accumulation of additional particles, resulting in a more significant obstruction.

In systems with higher arrival concentrations, blockage mechanisms occur earlier as the flow transitions between different regimes:

- A two-way interaction regime, where fluid and particle interactions dominate.
- A particle-collision-dominated regime, where particle-particle collisions are significant.
- A contact-dominated regime, where particle contact and friction primarily govern the flow behavior.

Momentum dissipation is a contributing factor. This occurs due to particle-particle and particle-wall interactions as well as drag forces. These interactions reduce particle momentum, and if the momentum falls below the threshold required to overcome friction, solids become immobilized, leading to obstructions.

An insufficient blade angle exacerbates this issue by reducing the gravitational force acting on the solid particles, further lowering their momentum and increasing the likelihood of blockages.

Axial dispersion during solid transport also contributes to blockages. Differences in particle velocities cause solids to overtake one another, resulting in uneven distribution and, ultimately, jamming

Lastly, bridging represents a critical blockage mechanism. This occurs at locations where solids converge from multiple directions, resulting in the formation of a stable bridge structure. This phenomenon

can completely block the passage, causing significant operational challenges.

8.1.3. Vulnerable Pump Areas

Flow assurance issues were observed at various critical locations within the pump. In the diffuser vanes, flow assurance risks arise due to the rapid narrowing of the vanes, which reduces the available space for solids. Combined with the insufficient blade angle, this leads to contact-dominated transport, where the velocity drops rapidly, further exacerbated by axial dispersion, ultimately resulting in jamming.

The transition from the diffuser to the impeller is a highly sensitive area for bridging. This obstruction can propagate back into the diffuser vanes, further exacerbating the issue.

The impeller blade design was a significant cause of blockages. Testing revealed that it was necessary to partially adjust the entry of the impeller to continue experiments. The curvature of the blades created a barrier effect, causing solids to accumulate against this curvature. Modifying this edge nearly eliminated the associated flow assurance issues. However, this modification introduces compromises under standard operating conditions, potentially reducing the overall efficiency of the pump.

The diffuser support was identified in the literature as a location prone to blockages. However, in tests conducted with solids having a maximum size equal to the solid passage diameter, no blockages were observed. When solids exceeded the solid passage diameter, some blockages occurred.

8.1.4. Influence of Variables

The geometry of the impeller blades requires redesign to enhance reflux performance. Increasing the blade angles of both the diffuser and impeller improves solid transport, reducing the likelihood of blockages.

Size distribution significantly impacts blockage formation. Solids exceeding the solid passing diameter tend to obstruct the pump earlier, primarily within the diffuser vanes. Even when the maximum particle diameter remains below the solid passage diameter, obstructions occur over time at various locations. This demonstrates that, during extended operation with large volumes of solids, blockages become inevitable. A narrower particle size distribution appears to improve flow assurance, although further research is required to confirm this effect.

Smaller solid size results in a higher surface-to-volume ratio. This increased surface area enhances particle-particle and particle-wall contact, which can exacerbate blockage formation.

A higher initial batch concentration and greater batch height lead to an increased pump arrival concentration. This elevated arrival concentration reduces the solids' throughput percentage due to intensified contact-dominated flow within the pump vanes. Consequently, blockages form more rapidly and are larger in scale.

The density of solids directly impacts their inertia. Solid density plays a critical role, as higher-density solids maintain higher momentum within the pump.

8.1.5. Evaluation of Experimental Setup for Investigating Reflux and Flow Assurance in Multi-Stage Centrifugal Pumps

The experimental setup proved to be an effective method for investigating reflux and flow assurance in multi-stage centrifugal pumps. The open-loop design allowed for numerous repeat tests under controlled conditions, enabling a thorough examination of various scenarios. The transparent pump casing facilitated detailed visual observations of blockages and solid movement, which were crucial for identifying and analyzing entrapment mechanisms. Additionally, the adaptability of the setup made it possible to test design modifications and directly assess their impact on flow assurance. Overall, the setup provided valuable insights and a reliable basis for optimizing pump performance.

8.2. Recommendations

8.2.1. Recommendations for Future Testing

- **DEM Simulations:** Conduct Discrete Element Method (DEM) simulations to further analyze variables that influence pump blockages. These simulations could replace extensive physical testing and be validated using results from this study.
- **Investigation of Spacing and Angle Combinations:** Conduct detailed testing to identify the optimal combination of spacing and blade angles needed to prevent blockages. Performing tests without a clear understanding of what causes the blockages is time-consuming and inefficient.
- **Use of Transparent Materials for Observation:** Ensure future setups include transparent components where feasible. Transparent materials allowed for critical observations of internal processes in this study. Without transparency, many of these insights would have been missed.
- **Size and Shape of Solids:** The size, shape, and size distribution of the solids after passing through the pump need to be better understood. These factors highly influence reflux behavior. While the size of the solids may decrease significantly after the 4000-meter ascent and their passage through the pump, the shape of the solids also plays a critical role.

8.2.2. Recommendations for an Improved Setup

- **Reverse Rotation of the Pump During Reflux:** Investigate the feasibility of eliminating resistance on the impeller to allow the pump to rotate freely in the direction of the reflux flow. By enabling the impeller to move with the flow, this adjustment could prevent issues such as bridging at the transition from diffuser to impeller, improving reflux handling.
- **Longer Axial Stages:** Develop a more optimized design for the pump stages, incorporating steeper inclines within the pump. This adjustment increases the influence of gravitational forces on the solids, helping to maintain their momentum and reducing the risk of settling.
- **Testing Additional Stages:** Include additional stages in the pump to examine if the likelihood of blockages decreases. Initial findings suggest that most blockages occur in the first stage, but it remains unclear if the frequency of blockages reduces or persists across subsequent stages.
- **Bypass System Design:** Consider implementing a bypass system that redirects the water-solid mixture above the pump stages during reflux. This would allow the pump geometry to be optimized for normal operation without needing to accommodate reflux scenarios, simplifying the design and enhancing efficiency.

8.2.3. Adjustments for the Current Test Setup

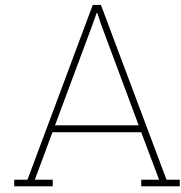
- **Blade Adjustment:** To improve flow assurance, the blades require optimization.
 - Adjust impeller blades to reduce the barrier effect that obstructs flow.
 - Optimize diffuser vane angles to promote momentum using gravitational forces.
 - Ensure consistent spacing between diffuser vanes to avoid performance deviations.
- **Sealing the Pump Model:** Ensure proper sealing of the model pump to prevent water leakage. Current issues with sealing resulted in water loss during tests.
- **Improved Imaging:** Enhancing imaging is key to accurately analyzing blockages and flow.
 - Avoid image distortion caused by the rounded, transparent parts of the pump and water by counteracting refraction effects through the use of materials with matched refractive indices or applying post-processing corrections in imaging software.
 - Capture footage from multiple angles to improve visualization and analysis of blockages.
 - Use blades with distinct colors compared to the pump's core to facilitate easier identification during video analysis.
 - Utilize color videos in addition to black-and-white recordings to enhance clarity for analysis.
- **Controlled Water Flow Setup:** Simulate real-world conditions by implementing a controlled water flow setup. In actual systems, the water partially settles due to the higher density of the mixture compared to the surrounding fluid. This effect was accounted for in the original design of the current setup through a U-loop, but it was omitted to save cost and space in the lab.
- **Testing with Actual Solids:** Conduct tests using actual nodules to replicate real-world conditions better and gain more representative results.

References

- [1] A.Ahnert et al. "Environmental risk assessment of anthropogenic activity in the deep sea". In: (2016).
- [2] C. Blanchard et al. "The current status of deep-sea mining governance at the International Seabed Authority". In: *Marine Policy* (2023).
- [3] D. Jones et al. "Environment, ecology, and potential effectiveness of an area protected from deep-sea mining (Clarion Clipperton Zone, abyssal Pacific)". In: *Progress in Oceanography* (2021).
- [4] D.Song et al. "Wall Effects on a Sphere Falling in Quiescent Power Law Fluids in Cylindrical Tubes". In: *American Chemical Society* (2009).
- [5] Fouquet et al. *Deep Marine Mineral Resources*. Springer Netherlands, 2014. URL: <https://link-springer-com.tudelft.idm.oclc.org/book/10.1007/978-94-017-8563-1>.
- [6] H. Zheng et al. "Lifting System". In: *Encyclopedia of Ocean Engineering* (2021).
- [7] j. chung et al. "Deep-Ocean Mining Technology III: Developments". In: *The International Society of Offshore and Polar Engineers* (2009).
- [8] J. Parianos et al. "Geology of parts of the central and eastern Clarion Clipperton Zone". In: *Journal of maps* (2022).
- [9] L. Liu et al. "Numerical Investigation on the Dynamics of Mixture Transport in Flexible Risers during Deep-Sea Mining". In: *Journal of Marine Science and Engineering* (2022).
- [10] L. Yuanwen et al. "Research on reflux in deep-sea mining pump based on DEM-CFD". In: (2022).
- [11] M. Elerian et al. "Flocculation effect on turbidity flows generated by deep-sea mining: A numerical study". In: *Ocean engineering* (2023).
- [12] M. Ozgoren et al. "Investigation of flow characteristics around a sphere placed in a boundary layer over a flat plate". In: *Experimental Thermal and Fluid Science* (2012).
- [13] Q. Hu et al. "CFD-DEM Simulation of Backflow Blockage of Deep-Sea Multistage Pump". In: *minerals* (2022).
- [14] Q. Hu et al. "Development of Hydraulic Lifting System of Deep-Sea Mineral Resources". In: *minerals* (2022).
- [15] R. James et al. "Critical metals in manganese nodules from the Cook Islands EEZ, abundances and distributions". In: *Ore Geology Reviews* (2015).
- [16] S. Poniaev et al. "Drag coefficient of solid micro-sphere between parallel plates". In: *Journal of Physics* (2016).
- [17] Y. Li et al. "Degradation of Polymetallic Nodules in Deep-Sea Multi-Stage Lifting Motor Pump". In: *Minerals* (2021).
- [18] Y. Liu et al. "Development of an efficient numerical model for two-phase flows in air-lift pumps and its application to deep-sea mining". In: *ocean engineering* (2021).
- [19] F. Ravelet et al. "Experimental study of hydraulic transport of large particles in horizontal pipes". In: *Experimental Thermal and Fluid Science* (2013).
- [20] H. Stel et al. "Numerical investigation of the flow in a multistage electric submersible pump". In: *Journal of Petroleum Science and Engineering* (2015).
- [21] K. Xia et al. "Experimental study of Air-lift system". In: (2017).
- [22] S. Teng et al. "Blockage of the Deep-Sea Mining Pump Transporting Large Particles with Different Sphericity". In: *China Ocean Engineering* (2023).
- [23] Y. Kang et al. "Design and analysis of an innovative deep-sea lifting motor pump". In: *Applied ocean research* (2019).
- [24] Y. Kang et al. "On the axial thrust and hydraulic performance of a multistage lifting pump for deep-sea mining". In: *Ocean Engineering* (2022).
- [25] Allseas. "Deep-Sea Polymetallic Nodule Collection". In: *Allseas Official Website* (2023). Accessed January 20, 2025. URL: <https://allseas.com/activities/deep-seapolymetallicnodulecollection/>.
- [26] G. Ardito. "Racing the clock: Recent developments and open environmental regulatory issues at the International Seabed Authority on the eve of deep-sea mining". In: *Marine policy* <volume number>. <issue number> (2022), <page range>.
- [27] R. Babu. "Design of Hydraulic Transportation System Using Positive Displacement Pump for Deep Sea Mining". In: *Journal of Thermal and Fluid Science* (2022).

- [28] J.L. Calderon. "Reviewing the material and metal security of low-carbon energy transitions". In: *Renewable and Sustainable Energy Reviews* <volume number>. <issue number> (2020), <page range>.
- [29] Ocean Conservancy. "Risks of Deep-Sea Mining: Economic and Social Disruptions". In: *Ocean Conservancy Blog* (2024). Accessed January 14, 2025. URL: <https://oceanconservancy.org/blog/2024/12/18/risks-deep-sea-mining/>.
- [30] Kumar D. "Air-lift pump systems for vertical solid particle transport: A comprehensive review and deep sea mining potential". In: *ocean engineering* (2024).
- [31] L. Deng. "Particle anti-accumulation design at impeller suction of deep-sea mining pump and evaluation by CFD-DEM simulation". In: *Ocean engineering* (2021).
- [32] L. Deng. "Particle Distribution and Motion in Six-Stage Centrifugal Pump by Means of Slurry Experiment and CFD-DEM Simulation". In: *Journal of Marine Science and Engineering* (2021).
- [33] R. Visintainer en el. *Slurry Transport Using Centrifugal Pumps*. Fourth Edition. Springer, 2017.
- [34] *Environmental Impact Assessment for Deep-Sea Mining*. Federal Institute for Geosciences and Natural Resources (BGR), 2020. URL: https://www.bgr.bund.de/EN/Home/homepage_node.html.
- [35] S. Graat. "Vertical transportation of collected manganese nodules by means of mechanical lifting". In: (2017).
- [36] J. Gulich. *Centrifugal Pumps*. Springer international publisher, 2020. URL: <http://link.springer.com/10.1007/978-3-030-14788-4>.
- [37] C. Han et al. "Influence of Blade Exit Angle on the Performance and Internal Flow Pattern of a High-Speed Electric Submersible Pump". In: *Water* (2023).
- [38] Hoog. "Transient Hydraulic Transport in Pipelines". In: (2024).
- [39] Impossible Metals. *Nodule Harvesting*. 2024. URL: <https://impossiblemetals.com/technology/robotic-collection-system/> (visited on 07/22/2024).
- [40] *Initial Assessment US SK 1300*. NORI D, 2021. URL: <https://www.nori-d.com>.
- [41] International Seabed Authority. *Exploration areas*. 2024. URL: <https://www.isa.org.jm/exploration-contracts/exploration-areas/> (visited on 06/18/2024).
- [42] Karassik. *Pump Handbook*. fourth Edition. McGraw-Hill, 2008.
- [43] G. Kuntz. "Advantages of Submersible Motor Pumps in Deep-Sea Mining". In: *KSB Homburg Work* (1980).
- [44] s. Lobanoff en el. *Centrifugal Pumps Design application*. second Edition. Transferred to digital printing 2010. 2010.
- [45] J. Miller. *The reciprocating pump : theory, design, and use*. Krieger Pub Co, 1995. URL: <https://tudelft.on.worldcat.org/search/detail/840278921?queryString=the%20reciprocating%20pump>.
- [46] K. Miller. "An Overview of Seabed Mining Including the Current State of Development, Environmental Impacts, and Knowledge Gaps". In: *Frontiers in Marine Science* <volume number>. <issue number> (2018), <page range>.
- [47] H. Nguyen. *Minerals for Climate Action: The Mineral Intensity of the Clean Energy Transition*. 2020. URL: <https://pubdocs.worldbank.org/en/961711588875536384/Minerals-for-Climate-Action-The-Mineral-Intensity-of-the-Clean-Energy-Transition.pdf> (visited on 12/05/2020).
- [48] C. van Rhee. *LectureNotes OE4627*. Tu Delft, 2018.
- [49] C. Van Rhee. *Centrifugal Pumps*. Fourth Edition. 2009.
- [50] Richardson and Zaki. "Sedimentation and fluidisation: part 1". In: *Chemical engineering research and design* (1954).
- [51] R.k. Sahu. *Pumps*. second Edition. New Age International Publishers, 2006.
- [52] R. Sharma. *Deep-Sea Mining: Resource Potential, Technical and Environmental Considerations*. <https://link.springer.com/book/10.1007/978-3-319-52557-0>. Springer, 2017.
- [53] SMD. *SMD deliver deep sea mining vehicles*. 2024. URL: <https://www.smd.co.uk/smd-deliver-deep-sea-mining-vehicles/> (visited on 08/22/2024).
- [54] O. Sparenberg. "A historical perspective on deep-sea mining for manganese nodules, 1965–2019". In: *The Extractive Industries and Society* (2019).
- [55] G. Takacs. *Electrical Submersible Pumps Manual: Design, Operations, and Maintenance*. 2nd ed. Gulf Professional Publishing, 2017.
- [56] The Metals Company. *The Metals Company*. 2024. URL: <https://metals.co/> (visited on 05/06/2024).
- [57] P. Vlasak. "Experimental investigation of coarse particle conveying in pipes". In: *Epj web of conferences* 92 (2015).

-
- [58] r. Wang. "Slurry pumps in deep-sea mining: A review of numerical and experimental studies". In: *Ocean engineering* (2022).
- [59] J. Van Wijk. "Vertical Hydraulic Transport for deep sea mining". In: (2016).
- [60] K. Willaert. "Fair Share: Equitable Distribution of Deep Sea Mining Proceeds". In: *International Journal of Marine and Coastal Law*. 37 (2022).
- [61] S. Worlanyo. "Evaluating the environmental and economic impact of mining for post-mined land restoration and land-use: A review". In: *Journal of Environmental Management* 279 (2021). <https://www.sciencedirect.com/science/article/pii/S0301479720315486>.
- [62] x. Zhang. "A Review on Underwater Collection and Transportation Equipment of Polymetallic Nodules in Deep-Sea Mining". In: *marine science and engineering* (2024).



Python Code: Particle Reynolds Number

```
1 import numpy as np
2 import matplotlib.pyplot as plt
3
4 # Parameters
5 rho = 1000 # Density of water (kg/m^3)
6 mu = 0.001 # Dynamic viscosity of water (Pa·s)
7 rho_knikker = 2400 # Density of the marble (kg/m^3)
8 g = 9.81 # Gravitational acceleration (m/s^2)
9 Cd = 0.47 # Drag coefficient for a sphere
10 phi_values = [0.05, 0.10, 0.15, 0.2] # Volume fractions
11 n = 2.4 # Empirical exponent stokes: 4.65 newton:2.4
12 v_f = 0 # Fluid velocity (m/s)
13
14 # Particle size ranges for each pipe diameter
15 d_knikker_ranges = [
16     np.linspace(0.00133, 0.012, 100), # for 40mm
17     np.linspace(0.003, 0.03, 100), # for 100mm
18     np.linspace(0.01, 0.09, 100) # for 300mm
19 ]
20
21 pipe_diameters = [0.04, 0.10, 0.3] # Pipe diameters
22
23 # Loop through each pipe diameter
24 for index, d_buis in enumerate(pipe_diameters):
25     d_knikker_range = d_knikker_ranges[index]
26
27     # Prepare figure for each pipe diameter
28     plt.figure()
29
30     # Calculate and plot for each phi value
31     for phi in phi_values:
32         Rep = np.zeros_like(d_knikker_range)
33         for i, d_knikker in enumerate(d_knikker_range):
34             # Terminal velocity
35             v_t = np.sqrt((4 * g * (rho_knikker - rho) * d_knikker) / (3 * rho * Cd))
36
37             # Hindered settling velocity
38             v_hindered = v_t * (1 - phi)**n * 10**(-d_knikker / d_buis)
39
40             # Solids phase Reynolds number
41             Rep[i] = (abs(v_f - v_hindered) * d_knikker * rho) / mu
42
43     # Plotting
44     plt.plot(d_knikker_range * 1000, Rep, label=f'Re□{phi}')
45
46     # Add reference lines
47     plt.axhline(y=4000, color='r', linewidth=2, label='Re□4000')
48     plt.axhline(y=3000, color='b', linewidth=2, label='Re□3000')
49
50     # Labels and legends
51     plt.xlabel('Solid□Size□(mm)')
```

```
52 plt.ylabel('Reynolds Number')
53 plt.title(f'Reynolds Number vs Solid Size for Pipe Diameter {d_buis*1000:.0f}mm')
54 plt.legend()
55 plt.grid(True)
56 plt.show()
```

B

Python Code: Required Pump Pressure

This appendix provides the Python code used to calculate the required pump pressure in an offshore system. The code computes hydrostatic pressure drops, frictional losses, and density-related pressure differences.

```
1 """
2 # Given parameters
3 rho_mix = 1200          # Density of the mixture (kg/m^3)
4 rho_water = 1025       # Density of water (kg/m^3)
5 Hriser = 4000          # Height of the riser (m)
6 Hjumper = 500          # Height of the jumper (m)
7 Hdeck = 10             # Height of the deck (m)
8 L = 4500               # Pipeline length (m)
9 D = 0.3                # Pipeline diameter (m)
10 v = 3                 # Fluid velocity (m/s)
11 f = 0.02              # Darcy friction factor
12 g = 9.81              # Gravitational acceleration (m/s^2)
13 Hpump = 1000          # Pump depth (m)
14
15 # Calculations
16 # Hydrostatic pressure drop due to deck height
17 deltaP_hydrostatic_deck = rho_mix * g * Hdeck
18
19 # Pressure drop due to the difference in densities over the riser and jumper
20 deltaP_density = (rho_mix - rho_water) * g * (Hriser + Hjumper)
21
22 # Frictional pressure drop through the pipeline
23 deltaP_friction = (L / D) * f * 0.5 * rho_mix * (v**2)
24
25 # Total pressure drop
26 deltaP_total = deltaP_hydrostatic_deck + deltaP_density + deltaP_friction
27
28 # Hydrostatic pressure at pump depth using the density of water
29 P_pump = rho_water * g * Hpump
30
31 # Convert pressures to bar
32 deltaP_bar = deltaP_total / 100000
33 P_pump_bar = P_pump / 100000
34
35 # Calculate the difference between the total pressure drop and the pump pressure
36 pressure_difference = P_pump - deltaP_total
37 pressure_difference_bar = pressure_difference / 100000
38
39 # Results
40 print(f"Hydrostatic pressure drop due to deck height: {deltaP_hydrostatic_deck:.2f} Pa")
41 print(f"Pressure drop due to difference in density: {deltaP_density:.2f} Pa")
42 print(f"Frictional pressure drop through the pipeline: {deltaP_friction:.2f} Pa")
43 print(f"Total pressure drop: {deltaP_total:.2f} Pa")
44 print(f"Total pressure drop: {deltaP_bar:.2f} bar")
45 print(f"Hydrostatic pressure at pump depth (H_pump = 1000m): {P_pump:.2f} Pa")
46 print(f"Hydrostatic pressure at pump depth: {P_pump_bar:.2f} bar")
47 print(f"Difference between total pressure drop and hydrostatic pressure: {pressure_difference:.2f} Pa")
48 print(f"Difference in pressure: {pressure_difference_bar:.2f} bar")
```

C

Testing

Initial Batch Concentration

The nodule dispenser is placed on top of the fallpipe and consists of two compartments. These compartments can be closed using gate valves and can be used either separately or together, depending on the test. The height of the compartments are 50 cm high and 30 cm, giving a volume of 3.88 liters and 2.32 liter, resulting in a total volume of 6.21 liters.

The term "initial batch concentration" refers to the volume fraction occupied by solids within the nodule dispenser. An initial batch concentration of 26% and 55% are commonly used, with additional tests occasionally conducted at 41% and 46%. The standard batch heights are set to either 10 cm or 20 cm, making these two variables batch height and initial batch concentration selectable per test. Appendix J provides the correct values for each test configuration. The height and initial batch concentration are target values and may not be exactly the same in every test. However, using this filling method ensures consistency across tests as much as possible. A measuring tape is attached to the compartments to clearly indicate the fill level for each test. To achieve the desired initial batch concentration, a second tube is inserted into the dispenser for tests with an initial batch concentration of 26%. This setup allows for adjusting the concentration to lower levels if needed. The placement of this tube within the dispenser is shown in Figure C.1 on the right. The inner diameter of this tube is 68.6 mm, which reduces the available area for solids by 52%.

In Section C, the confirmation test is presented, which verifies whether the specified fill heights and filling method correspond to the given initial density of the batch. The results of this confirmation test indicate that the correct values are obtained. In Figure C.1, the left image shows a 55% mixture with a filling height of 10 cm, while the right image displays a 26% mixture with a filling height of 20 cm.



Figure C.1: L: Nodule dispenser 55 % and 10cm height, R: Nodule dispenser 26% and height of 20 cm

Confirmation Test: initial batch concentration

The initial batch concentration is frequently referenced. It is used to consistently reproduce the initial conditions of the test, rather than to create a predefined concentration at the pump. However, it is important to note that the initial batch concentration is not always exactly the same across different tests. To gain a clearer understanding of the actual percentage of the solids' volume, a control was performed using homogeneous batches.

The results of this control test are presented in Table C.1. The procedure for these tests was as follows: the nodule dispenser was filled with water up to a height of 10 cm, after which the relevant batch of solids was added. The subsequent increase in water height was measured and converted into a percentage, which corresponds to the volume occupied by the solids.

Table C.1: Summary of Results for Tests with Different Densities and Sizes

Test	Density (kg/m ³)	Size (mm)	Height Batch (mm)	Initial Density (%)	Weight Batch (g)	End Height Water (mm)	Measured Density (%)
2	1400	10	100	26	284	125	25
4	1400	10	100	46	503	147	47
6	1400	10	100	55	599	158	58
8	1400	20	100	26	284	126	26
12	1400	20	100	55	599	157	57
14	1400	30	100	26	284	127	27
52	2400	10	100	26	487	125	25
54	2400	10	100	46	862	146.5	47
56	2400	10	100	55	1028	156	56
58	2400	20	100	26	487	125	25
62	2400	20	100	55	1028	154	54
64	2400	30	100	26	487	127	27
68	2400	30	100	55	1028	154	54

The results of these tests indicate that the expected initial batch concentration percentage closely aligns with the actual values. This demonstrates that it serves as a reliable indicator.

Step-by-Step Procedure for Series A1

This section provides a step-by-step procedure for conducting Series A1 of the fallpipe experiment, including setup, execution, and data recording.

The procedure for Series A1 is as follows:

1. Start by closing all valves except valve number 1.
2. Fill up the test setup with water.
3. Set up the camera with the correct settings, turn on the backlight and ensure everything is visible.
4. In the document "Fallpipe experiment Series One," look up the next test. Here, the correct solid density and diameter are indicated.
5. Measure the weight of the solid and fill in the document.
6. Place the solid in the solid dispenser and start the camera.
7. Open the nodule dispenser.
8. Once the solid passes through the pipe, stop the camera.
9. Using the software, record the entrance time (passing the first marker) and the exit time (passing the second marker) in the document.
10. If there are any notable occurrences, record them in the document.
11. End the test.

Check-List

This checklist provides a step-by-step guide for conducting the experimental procedure, including setup preparation, testing, and cleanup.

Table C.2: Step-by-Step Experimental Procedure

#	Description	DONE	Notes
1	Check that the valves are properly closed.	<input type="checkbox"/>	
2	Fill the setup with water.	<input type="checkbox"/>	
3	Check for any leaks.	<input type="checkbox"/>	
4	Start preparing the nodule sample. Refer to [document or section].	<input type="checkbox"/>	
4.1	Get the correct mix from the bucket and weigh the correct amount.	<input type="checkbox"/>	
5	Place the sample in the dispenser and ensure it is at the correct height as indicated in [document or section].	<input type="checkbox"/>	
6	Fill the rest with water.	<input type="checkbox"/>	
7	Check if the camera is in the correct position.	<input type="checkbox"/>	
8	Check the lighting.	<input type="checkbox"/>	
9	Fill in the information as per [document or section].	<input type="checkbox"/>	
10	Start the camera.	<input type="checkbox"/>	
11	Show test number.	<input type="checkbox"/>	
12	Open the nodule valve.	<input type="checkbox"/>	
13	The test is complete when all nodules are stationary.	<input type="checkbox"/>	
14	Stop the camera.	<input type="checkbox"/>	
15	Take a picture of the end result.	<input type="checkbox"/>	
16	Note the results in [document or section].	<input type="checkbox"/>	
17	Empty the water.	<input type="checkbox"/>	
18	Clean the setup.	<input type="checkbox"/>	

D

Pump-Pipe Connection Drawing

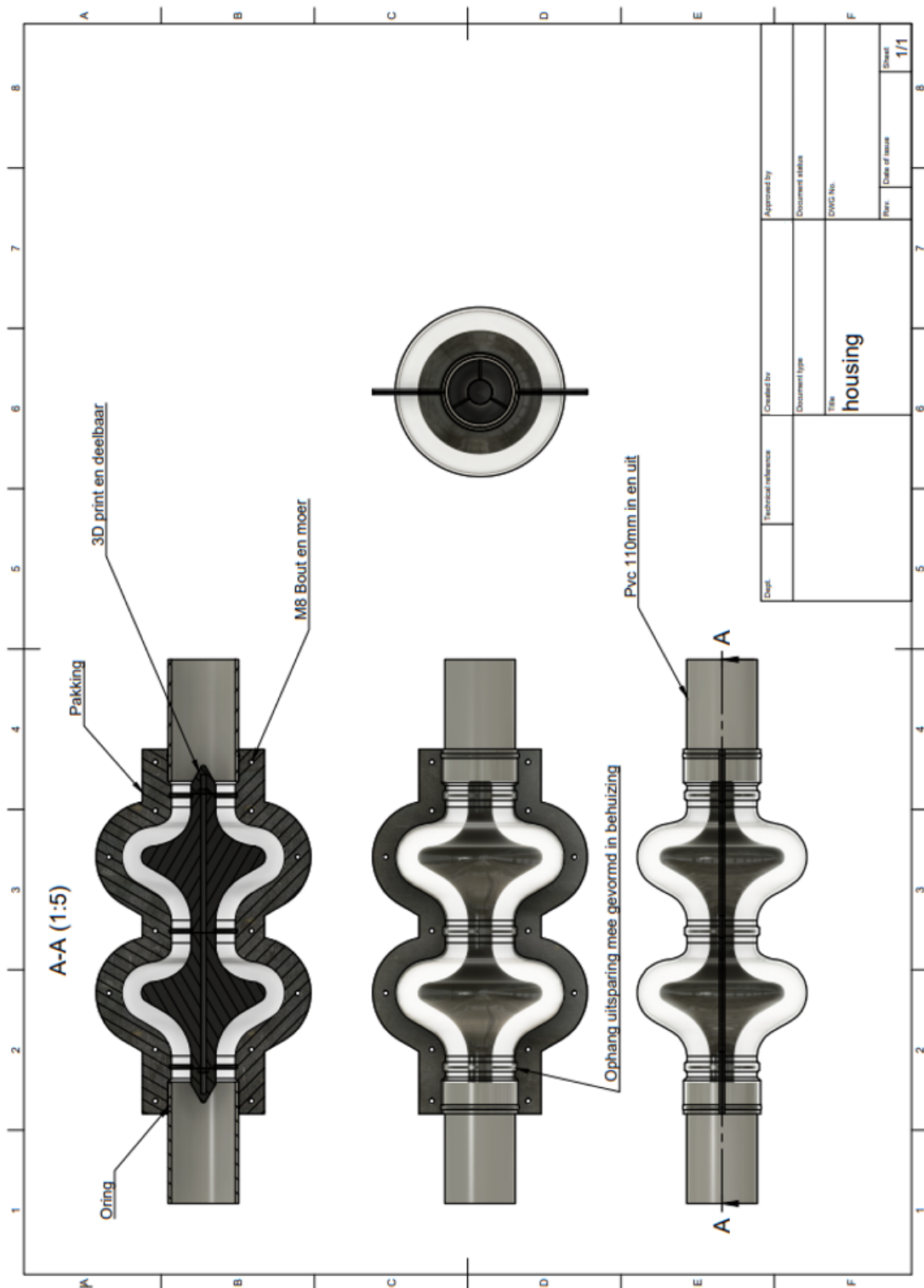


Figure D.1: Drawing Pump Model

E

Fallpipe Settling

Fallpipe Terminal Settling Velocity by Size Glass spheres

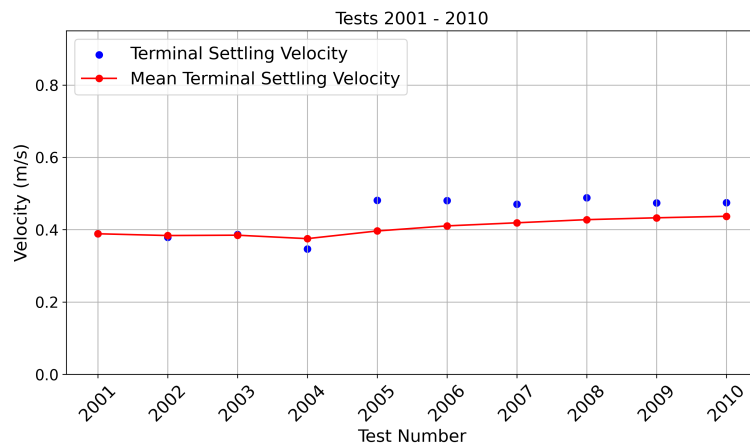


Figure E.1: Glass spheres - Solid Size:5mm

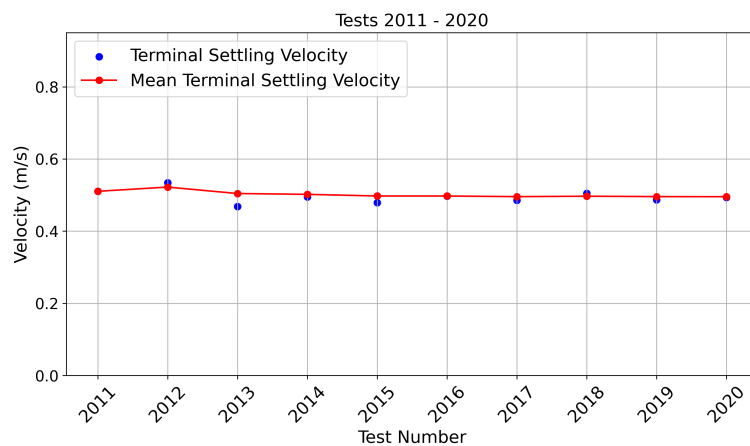


Figure E.2: Glass spheres - Solid Size 10mm

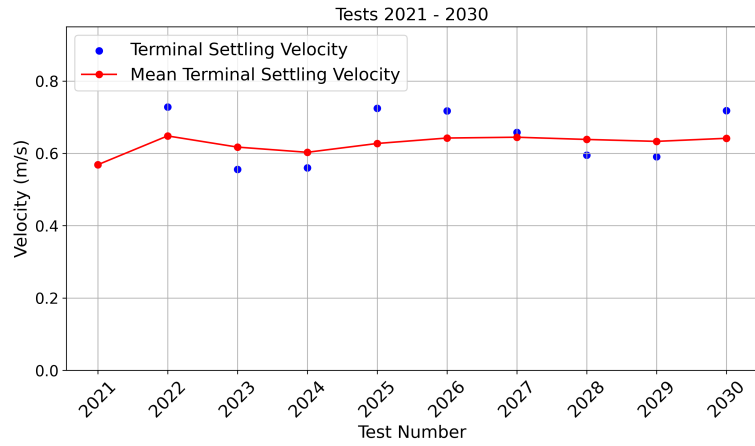


Figure E.3: Glass spheres - Solid Size 15mm

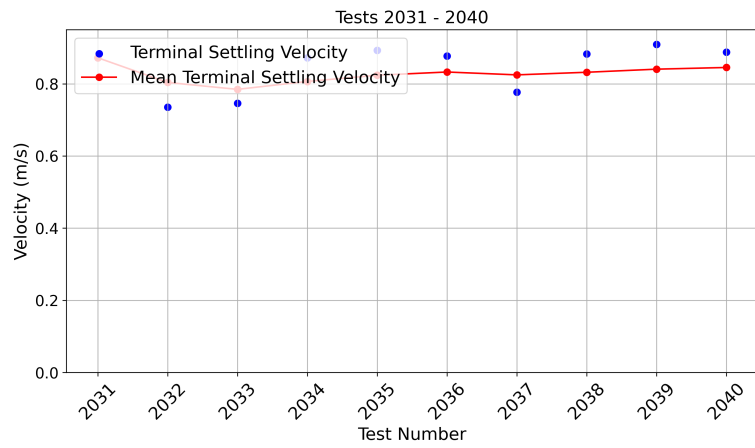


Figure E.4: Glass spheres - Solid Size 20mm

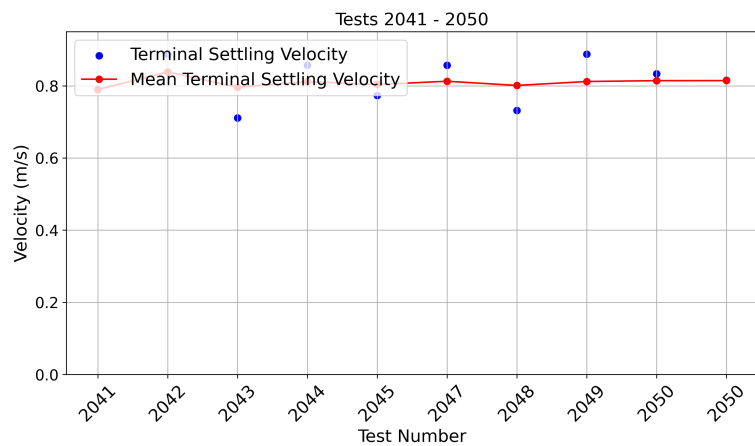


Figure E.5: Glass spheres - Solid Size 25mm

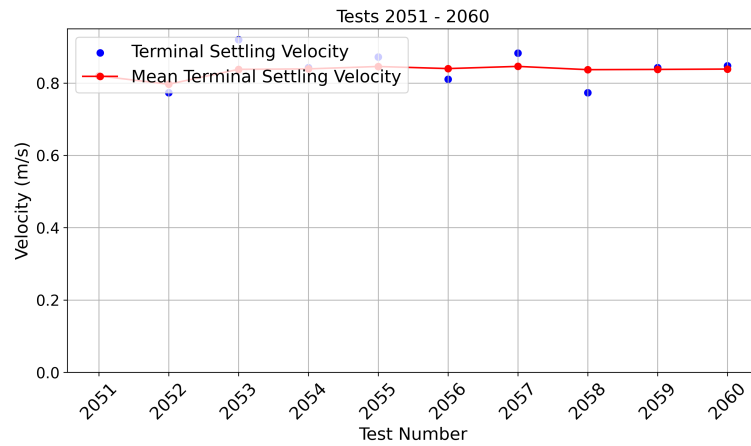


Figure E.6: Glass spheres - Solid size 25mm

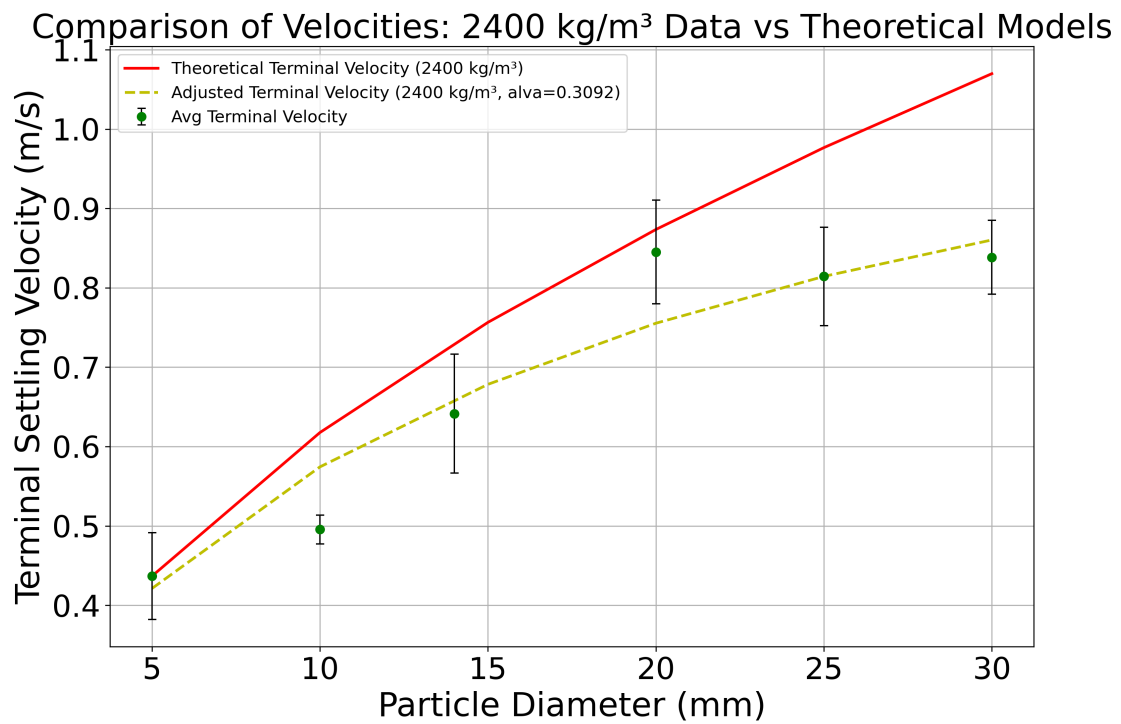


Figure E.7: Comparison of Velocities: Test Data vs Theoretical Models for Density 2400 kg/m^3 ($R^2 = 0.90$)

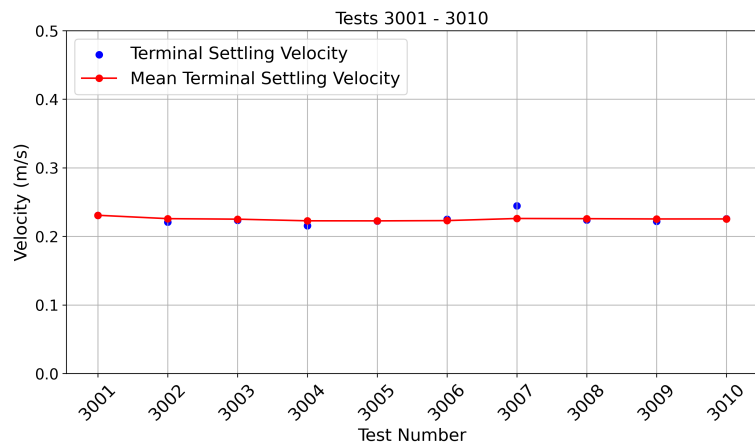
1400kg/m³

Figure E.8: POM spheres - Solid Size 5mm

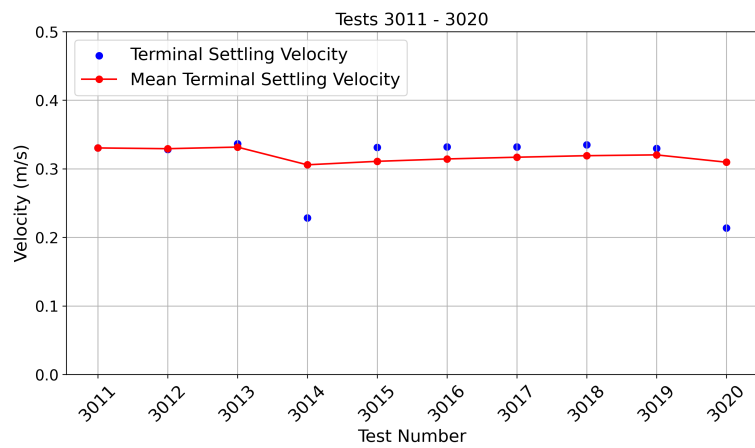


Figure E.9: POM spheres - Solid Size 10mm

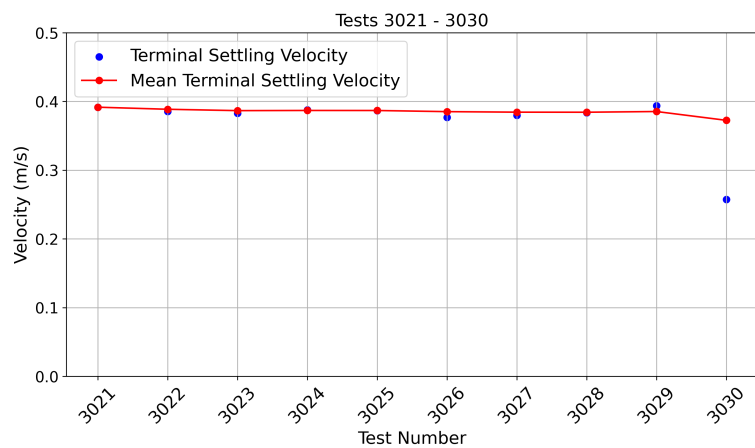


Figure E.10: POM spheres - Solid Size 15mm

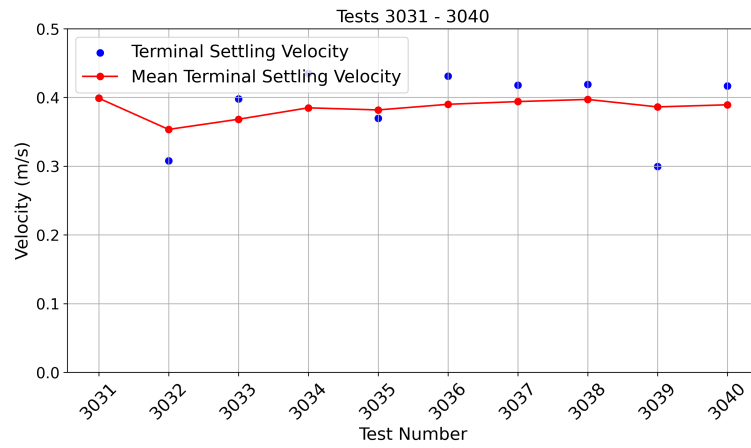


Figure E.11: POM spheres - Solid Size 20mm

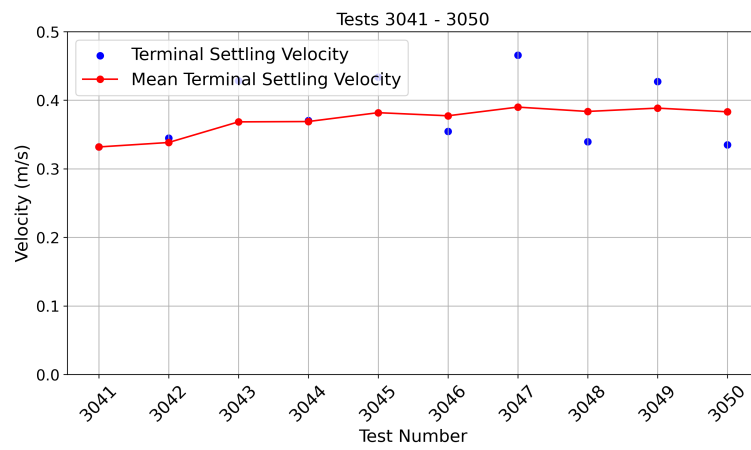


Figure E.12: POM spheres - Solid Size 25mm

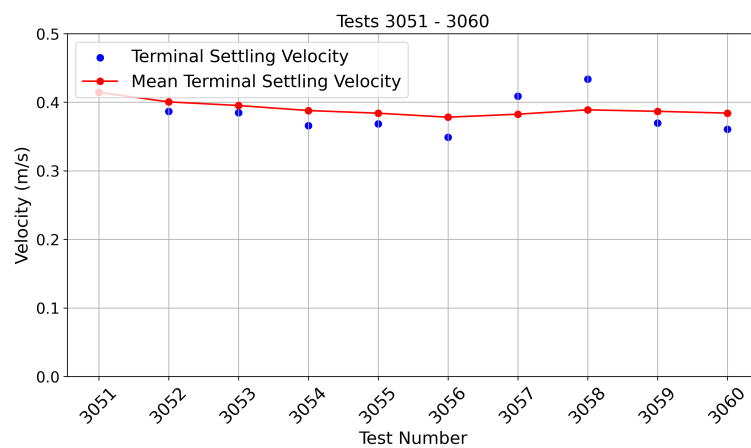


Figure E.13: POM spheres - Solid Size 30mm

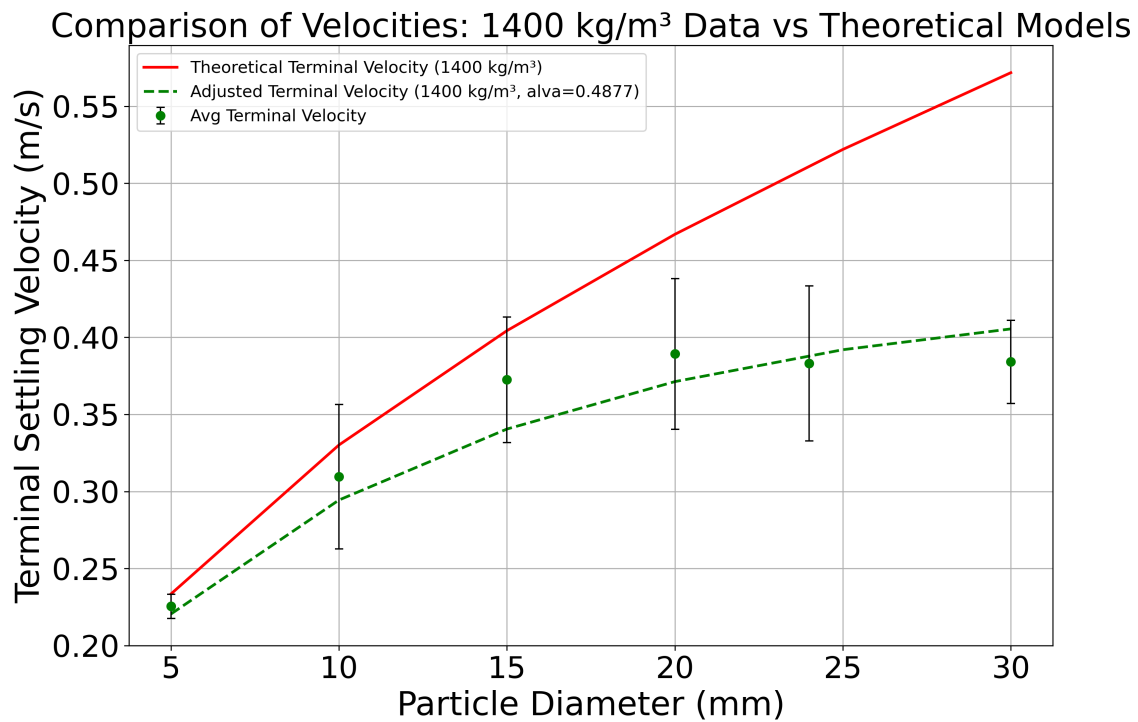


Figure E.14: Comparison of Velocities: Test Data vs Theoretical Models for Density 1400 kg/m³ ($R^2 = 0.90$)

Filtered Data Result

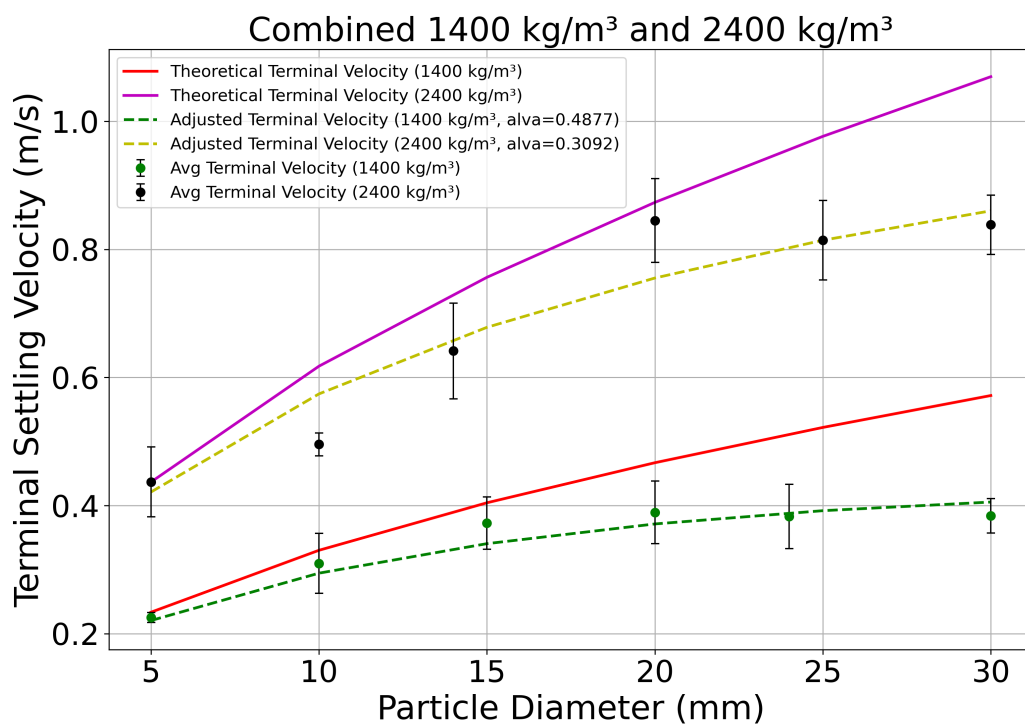


Figure E.15: Comparison of measured and theoretical velocities for filtered data, 2400kg/m³ ($R^2 = 0.81$) 1400kg /m³ ($R^2 = 0.88$)

Fallpipe Batch
2400 kg/m³

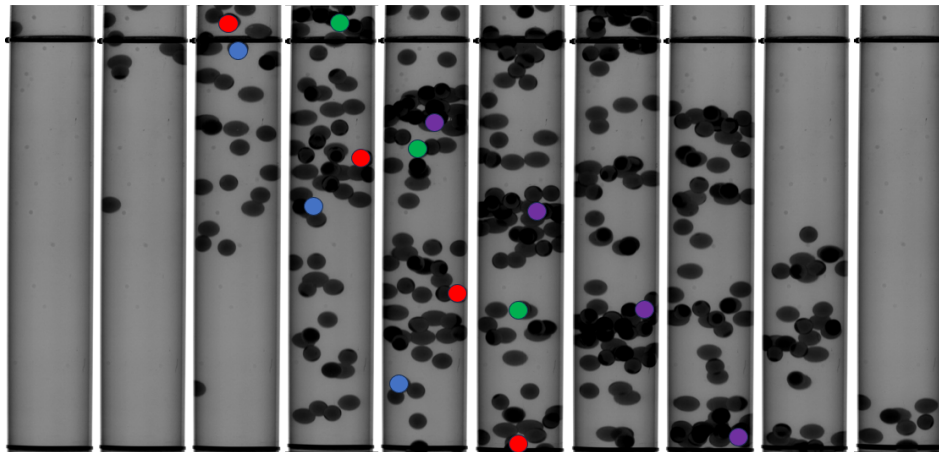


Figure E.16: Overview of settling behaviour test 4004 (2400 kg/m³, 20 mm, initial density 46, batch height 10 cm)

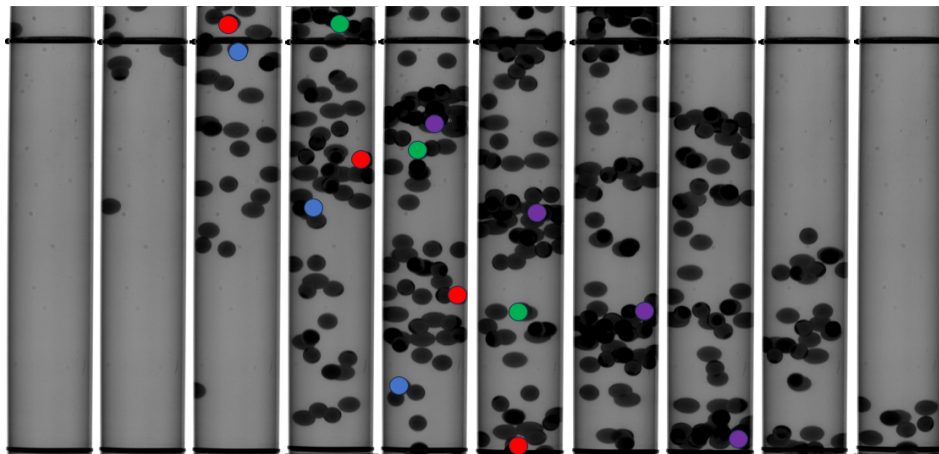


Figure E.17: Overview of settling behaviour test 4008 (2400 kg/m³, 20 mm, initial density 46, batch height 20 cm)

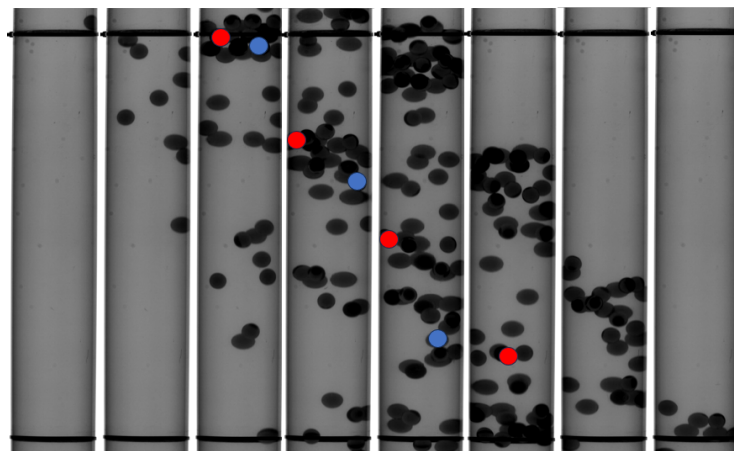


Figure E.18: Overview of settling behaviour test 4013 (2400 kg/m³, 20 mm, initial density 26, batch height 20 cm)

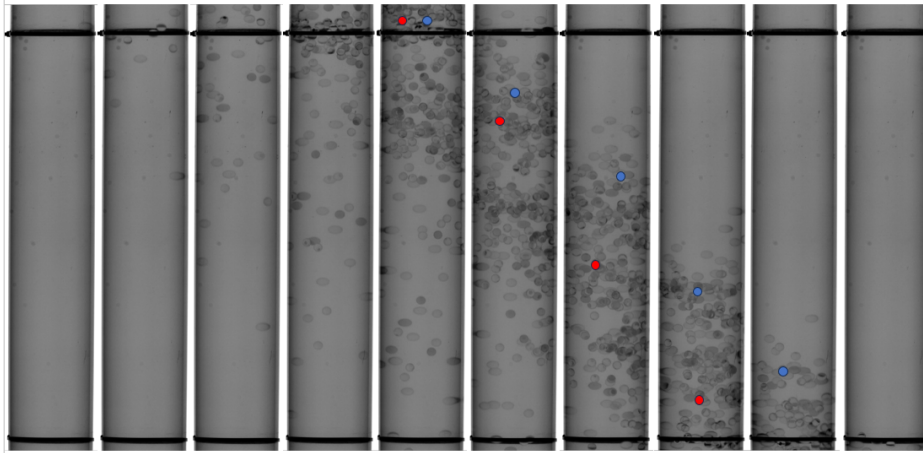


Figure E.19: Overview of settling behaviour test 4016 (2400 kg/m^3 , 10 mm, initial density 26, batch height 10 cm)

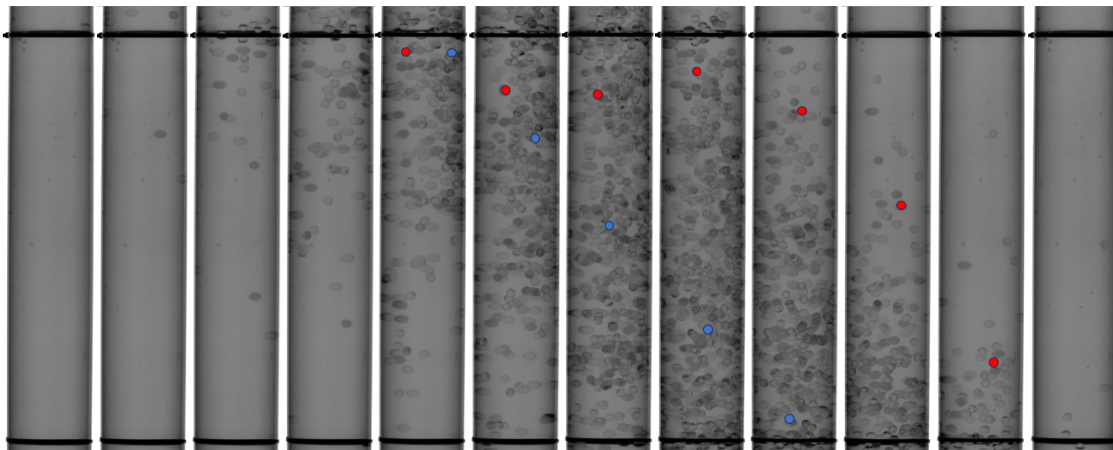


Figure E.20: Overview of settling behaviour test 4019 (2400 kg/m^3 , 10 mm, initial density 26, batch height 20 cm)

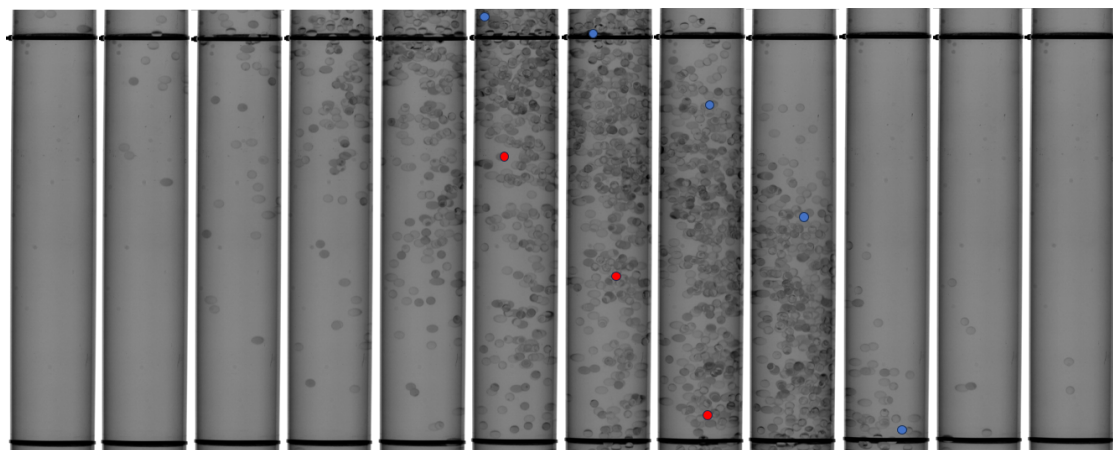


Figure E.21: Overview of settling behaviour test 4022 (2400 kg/m^3 , 10 mm, initial density 46, batch height 10 cm)

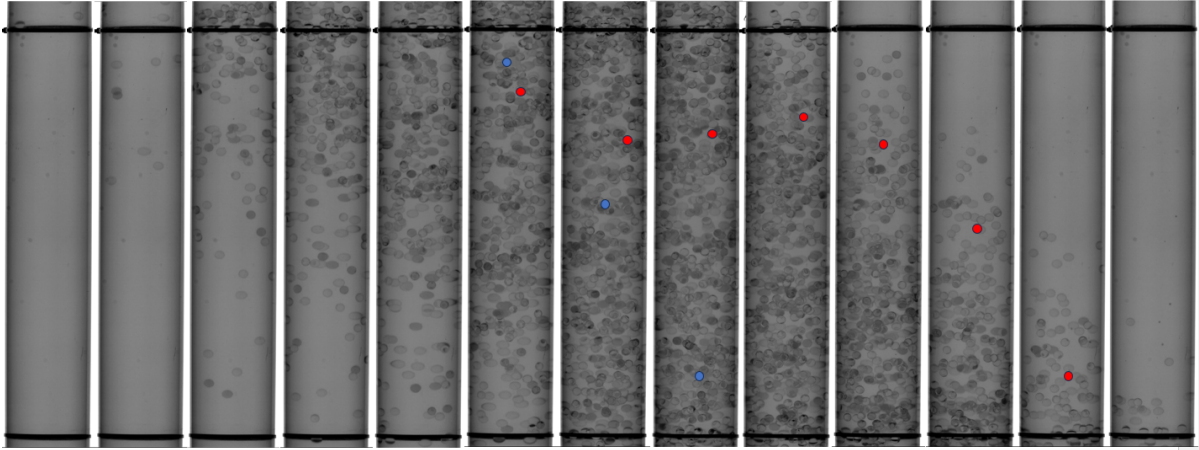


Figure E.22: Overview of settling behaviour test 4025 (2400 kg/m^3 , 10 mm, initial density 46, batch height 20 cm)

POM spheres

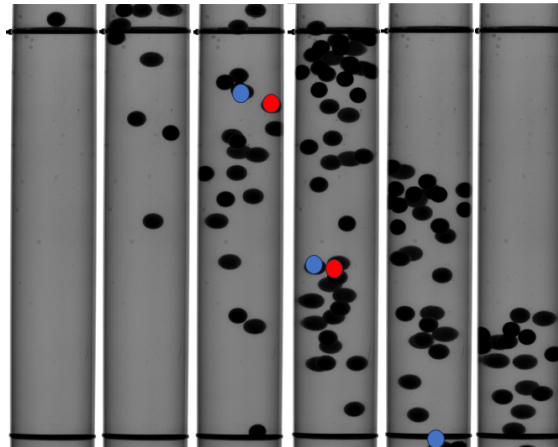


Figure E.23: Overview of settling behaviour test 5002 (1400 kg/m^3 , 20 mm, initial density 26, batch height 10 cm)

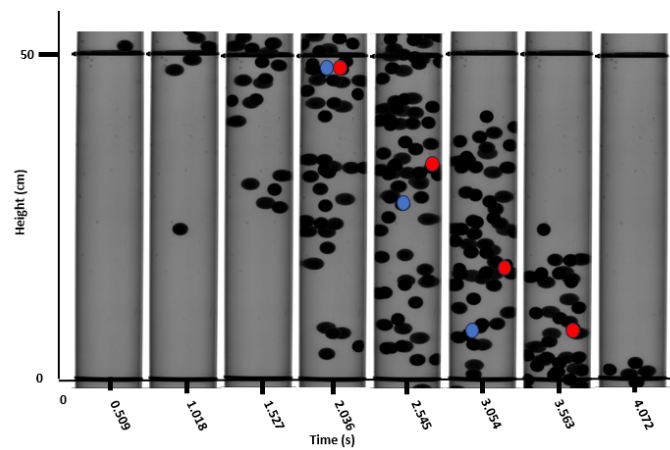


Figure E.24: Overview of settling behaviour test 5005 (POM spheres, 20 mm, initial concentration 46%, batch height 20 cm, Timestamp: 0.509s)

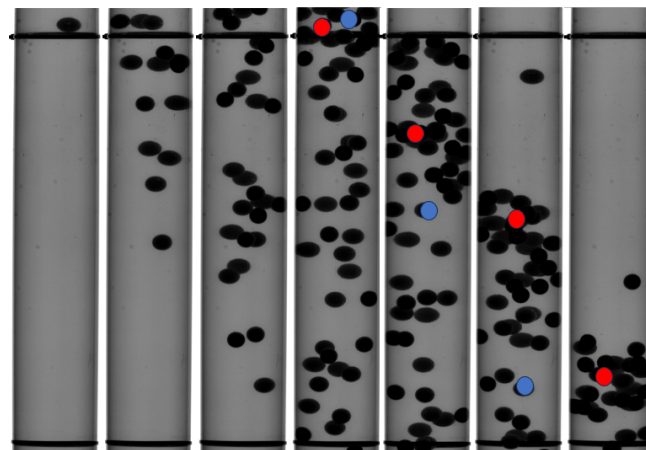


Figure E.25: Overview of settling behaviour test 5007 (1400 kg/m^3 , 20 mm, initial density 26, batch height 10 cm)

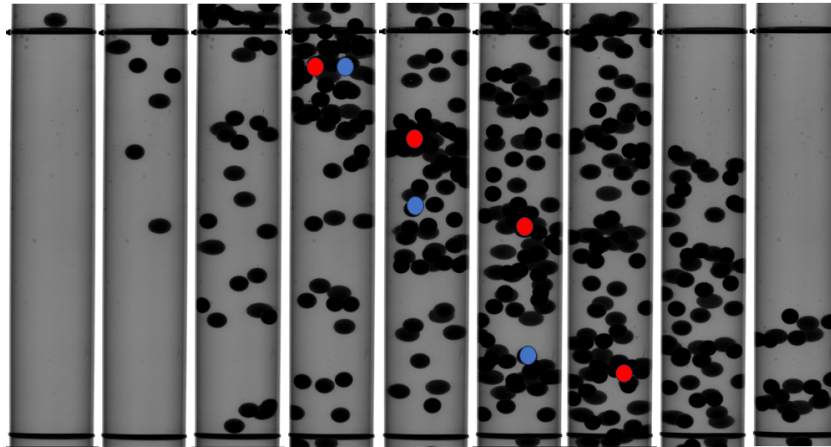


Figure E.26: Overview of settling behaviour test 5010 (1400 kg/m^3 , 20 mm, initial density 46, batch height 20 cm)

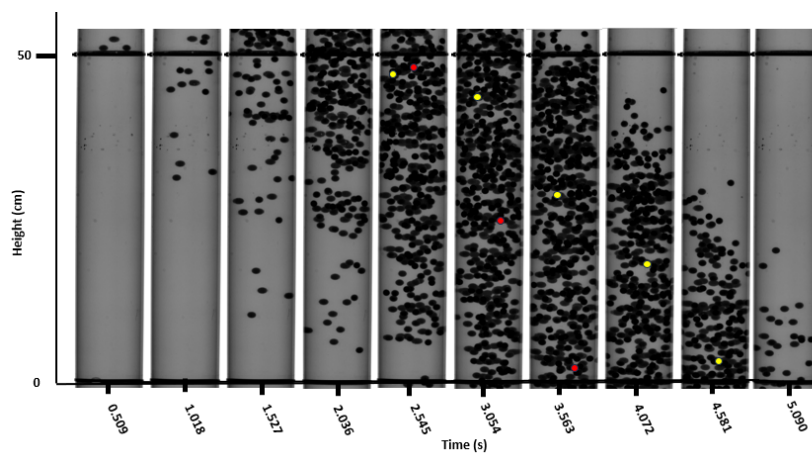


Figure E.27: Overview of settling behaviour test 5018 (POM spheres, 10 mm, initial concentration 26%, batch height 20 cm, Timestamp: 0.509s)

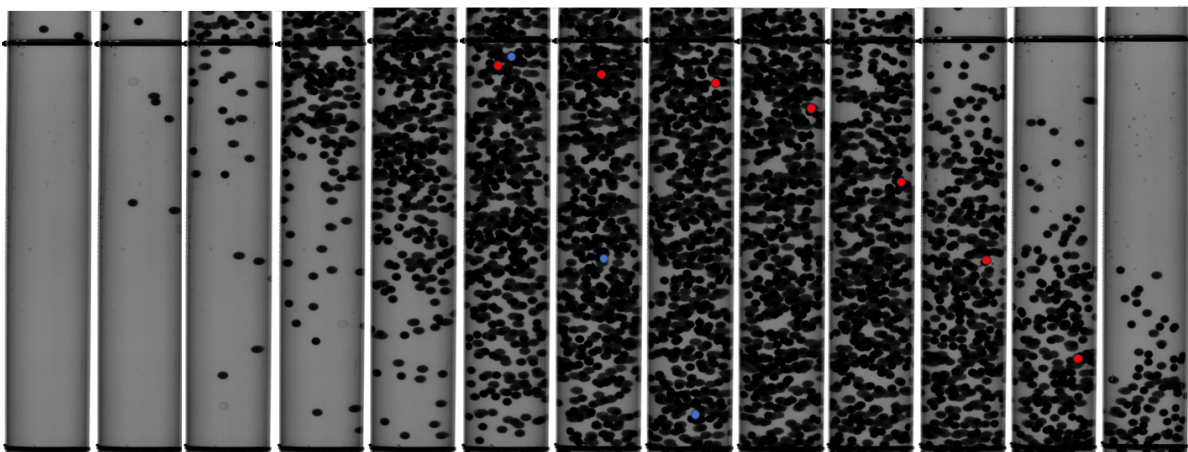


Figure E.28: Overview of settling behaviour test 5023 (1400 kg/m^3 , 10 mm, initial density 46, batch height 20 cm)

F

Pump One: Pump Without Blades

Pump One, Series Two

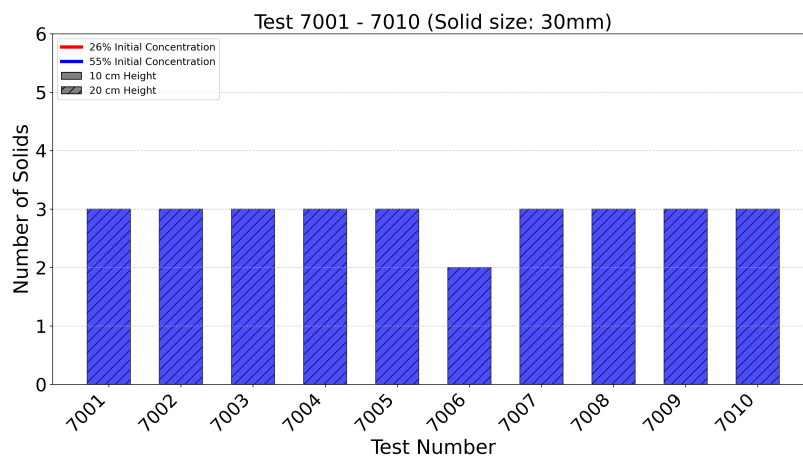


Figure F.1: Test 7001 to 7010 (1400 kg/m³, 30mm, Initial batch concentration 55%, bed height 20cm)

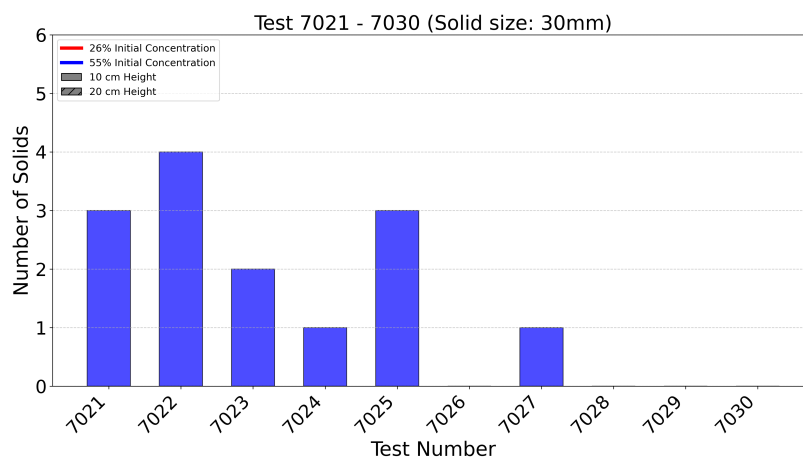


Figure F.2: Test 7021 to 7030 (1400 kg/m³, 30mm, Initial batch concentration 55%, Batch height 10cm)

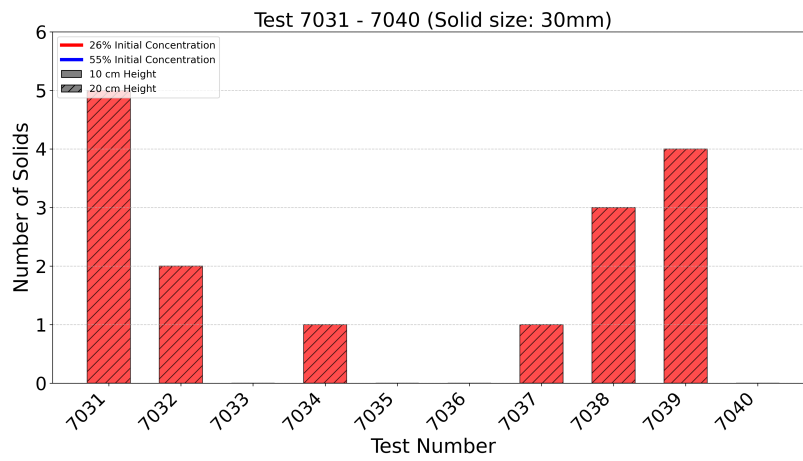


Figure F.3: Test 7031 to 7040 (1400 kg/m^3 , 30mm, Initial batch concentration 26%, Batch height 20cm)

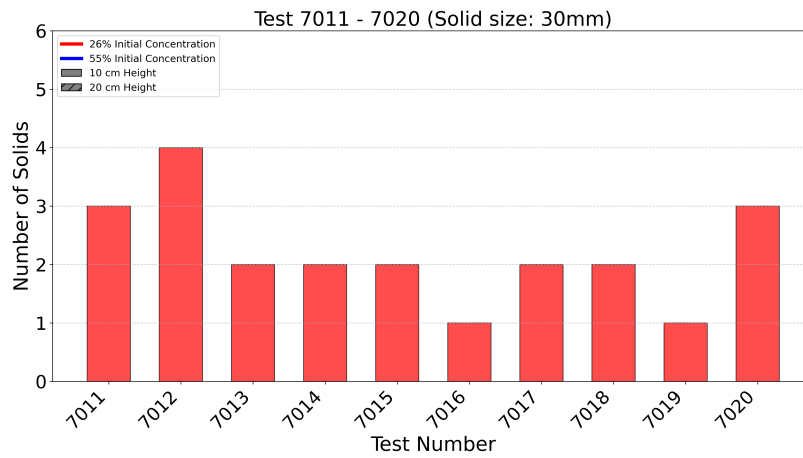


Figure F.4: Test 7011 to 7020 (1400 kg/m^3 , 30mm, Initial batch concentration 26%, Batch height 10cm)

G

Drag Force

Considering the solid positioned between the pump core and the pump housing, the configuration can be conceptualized as a solid situated between two inclined planes. The solid has a thickness of 30 mm, while the spacing between the two planes is 30.4 mm, leaving a narrow clearance of just 0.4 mm for fluid flow. This narrow gap suggests the formation of a thin water layer between the solid and the planes, which likely prevents direct contact between the solid and the planes. This setup implies that the water displaced by the solid must flow upward through the narrow clearance, introducing additional drag forces. Therefore, the influence of the drag force exerted by the moving fluid should be analyzed in greater detail, as it may significantly affect the overall behavior of the system.

Given the small spacing of 0.004 m, the Reynolds number for the flow is likely below 1000, indicating a laminar flow regime at this location. This type of flow is characterized by a predominance of viscous forces and relatively high friction compared to turbulent flow.

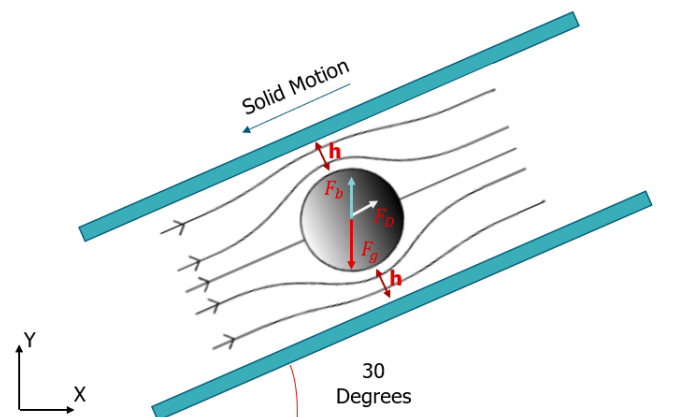


Figure G.1: Situation sketch Drag Force

The figure G.1 schematically illustrates the situation, with the two planes positioned to enclose the solid. The spacing between the solid and the planes is denoted as h . This represents a very specific configuration, for which limited research is available. The available research does not precisely match the described situation.

I. Song conducted a study that numerically examines the effect of finite boundaries on the drag force experienced by a sphere settling in fluids within tubes. The findings indicate that finite boundaries increase drag, thereby slowing the sphere's descent. This effect was analyzed for Reynolds numbers in the range of 1–100, power-law indices between 0.2 and 1, and sphere-to-tube diameter ratios ranging from 0 to 0.5 [4]. Figure G.2 illustrates the velocity vector and streamline patterns as presented in the results.

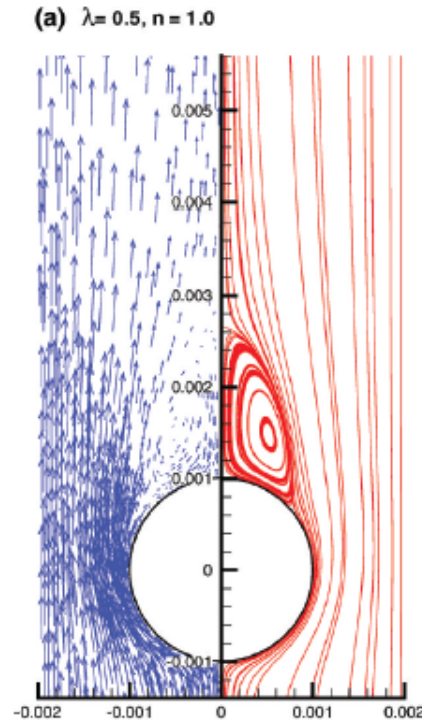


Figure G.2: Velocity vector and streamline patterns for a sphere-to-tube diameter ratio of 0.5, $Re = 100$, and $n = 1$ [4].

M. Ozgoren in his study experimentally investigated how the interaction between a sphere and a turbulent boundary layer flow affects the flow characteristics at various gap ratios (G/D), where G is the gap between the bottom of the sphere and the flat plate, and D is the diameter of the sphere. The gap ratio (G/D) ranged from 0 to 1.5, with the sphere having a diameter of $D = 42.5$ mm. The study considered Reynolds numbers in the range of $2500 \leq Re \leq 10,000$. The results show that at small G/D values, the flow is significantly disturbed by the proximity of the plate. This leads to jet-like flow through the small gap, asymmetric wakes, and increased drag, while vortex shedding is suppressed, particularly at the lower section of the sphere. [12] The flow behavior at $G/D = 0.5$ and $Re = 5000$, including the flow structure, velocity distribution, and vorticity patterns, is shown in Figure G.3.

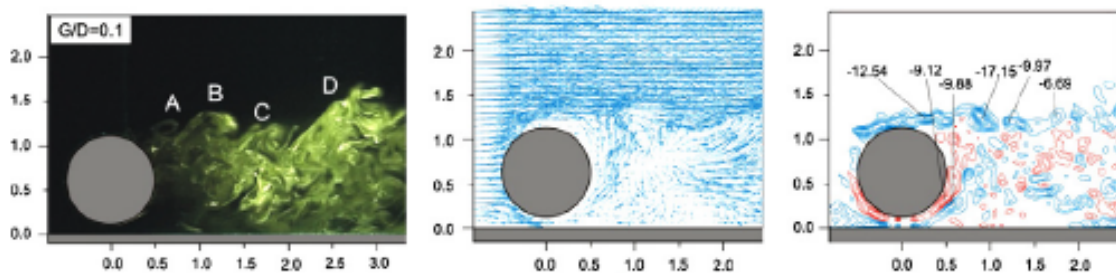


Figure G.3: Flow visualization around the sphere at $G/D = 0.5$ and $Re = 5000$. The left panel shows the flow structure visualized using laser illumination and a Rhodamine dye injection technique, the middle panel presents the normalized instantaneous velocity (V), and the right panel depicts the dimensionless vorticity (ω^*). [12]

S. A. Poniaev et al. conducted a numerical simulation to investigate the drag coefficient of a solid sphere in a two-wall channel formed by parallel plates. The study explored the dependence of drag on the normalized distance between the sphere and the channel wall (d/D), as well as the channel height (H/D), where H is the channel height and D is the sphere diameter. The simulation considered micro-spheres with $D = 1$ mm and Reynolds numbers of $Re = 10^{-3}$. Results show that in channels with $H/D < 5$, the drag coefficient is significantly higher compared to both unbounded flows and single-wall channels with the same d/D . This effect diminishes as H/D increases, but remains substantial for small H/D , emphasizing the strong influence of confinement on drag forces in micro-scale flows [16].

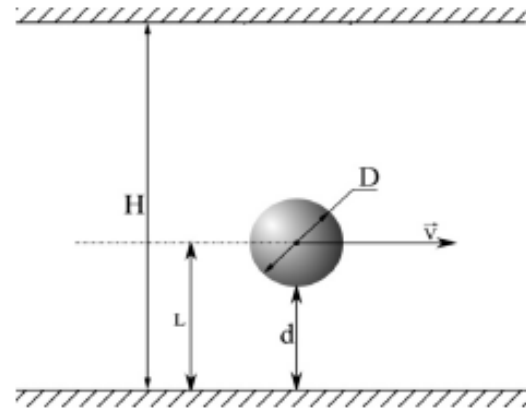
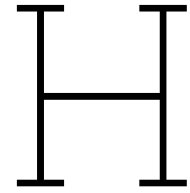


Figure G.4: Schematic of sphere motion in the channel [16]

The setup discussed in this research involves a solid positioned between two inclined planes with a narrow clearance of 0.4 mm, creating a highly confined flow environment. The referenced studies, while not directly replicating this geometry, provide valuable insights into the role of confinement in increasing drag forces. Song's study demonstrates how finite boundaries significantly enhance drag by restricting fluid flow. Similarly, Ozgoren's findings highlight that small gaps can lead to jet-like flow, asymmetric wakes, and increased drag. Poniaev et al. further confirm that confined geometries, such as narrow channels, result in higher drag forces compared to unbounded flows, with the effect becoming more pronounced as the degree of confinement increases. These studies collectively underline the importance of considering drag force in this setup, as it is likely to have a substantial impact on the force equilibrium and overall flow dynamics.



Pump Two: Pump With Blades

Pump Two, Series Two
2400 kg/m³ Different sizes (1500g)

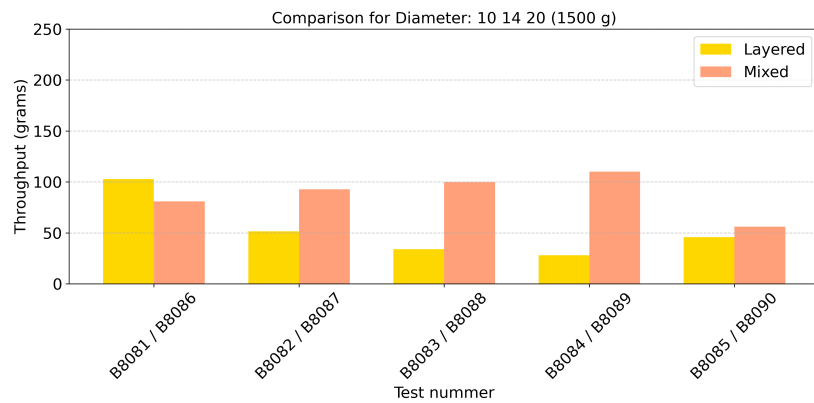


Figure H.1: Comparison for sizes 10, 14, and 20 with density 2400 kg/m³

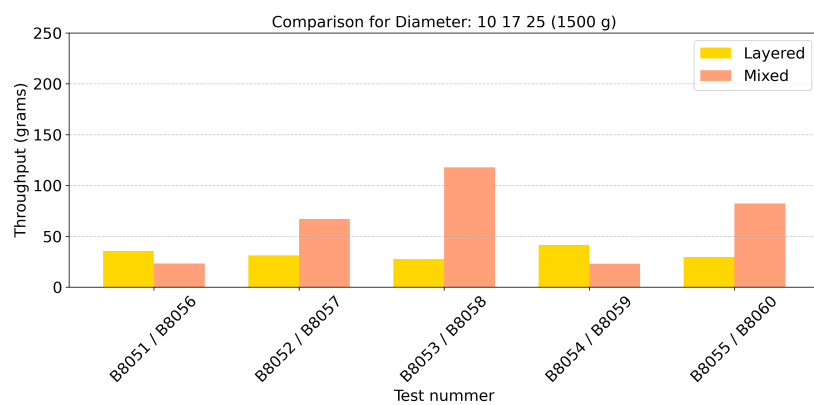


Figure H.2: Comparison for sizes 10, 17, and 25 with density 2400 kg/m³

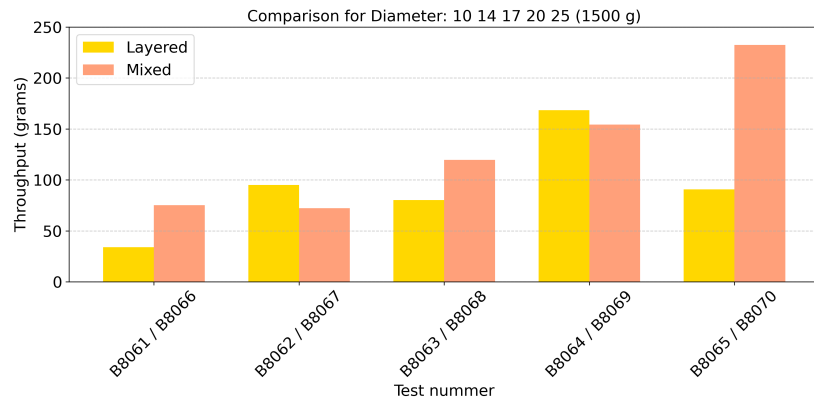


Figure H.3: Comparison for sizes 10, 14, 17, 20, and 25 with density 2400 kg/m³

Sizes 10 14 20 (3000g)

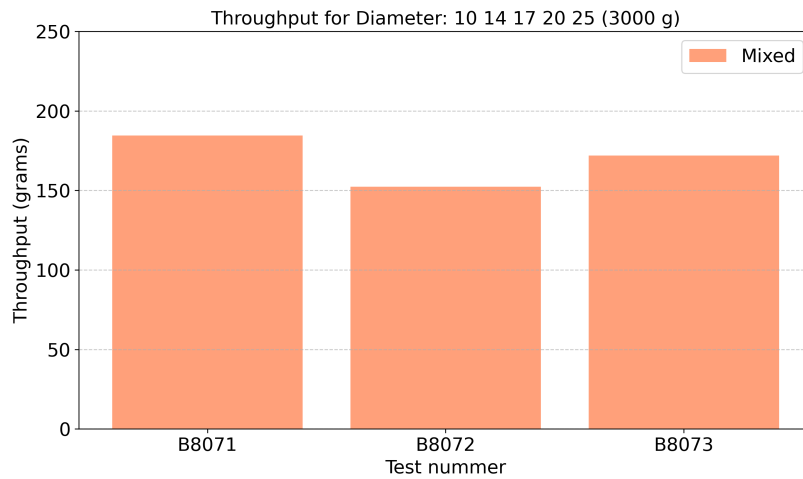


Figure H.4: Throughput comparison for sizes 10, 14, and 20 (3000 g)

Sizes 10 14 17 20 25(3000g)

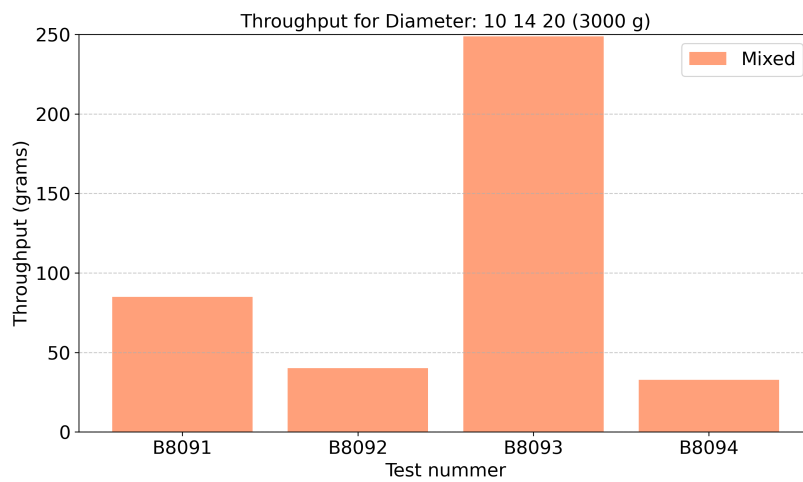


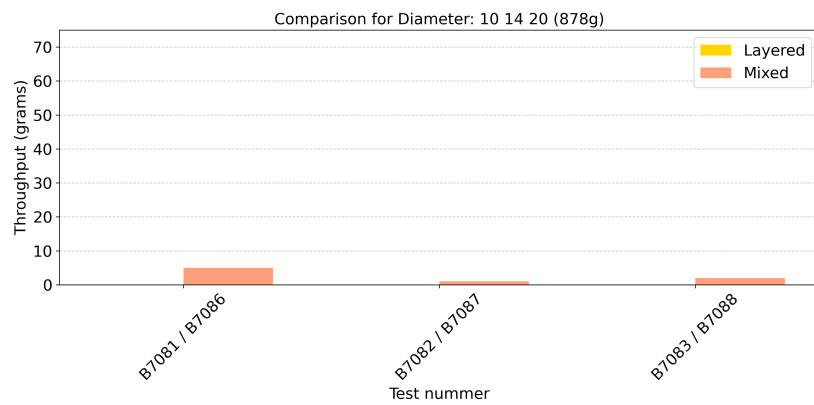
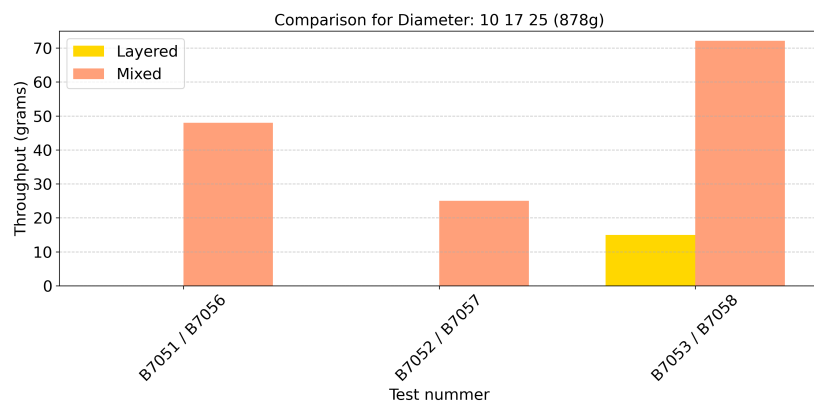
Figure H.5: Throughput comparison for sizes 10, 14, 17, 20, and 25 (3000 g)

Summary of all tests Glass

Table H.1: Summary of Throughput and Percentages for Different Sizes and Situations (Glass Spheres)

Size (mm)	Repetition (-)	Layered/Mixed (-)	Amount (g)	Throughput (g)	Percentage (%)
10 14 20	5	Layered	1500	52.36	3.5
10 14 20	5	Mixed	1500	87.90	5.9
10 14 20	4	Mixed	3000	101.65	3.4
10 14 20	1	Mixed	4500	190.00	4.2
10 17 25	5	Layered	1500	33.08	2.2
10 17 25	5	Mixed	1500	62.71	4.2
10 14 17 20 25	5	Layered	1500	93.68	6.2
10 14 17 20 25	5	Mixed	1500	130.76	8.7
10 14 17 20 25	3	Mixed	3000	169.60	5.7

Pump Two, Series Two
1400 kg/m³ Different sizes (878g)

**Figure H.6:** Comparison for sizes 10, 14, and 20 with density 1400 kg/m³**Figure H.7:** Comparison for sizes 10, 17, and 25 with density 1400 kg/m³

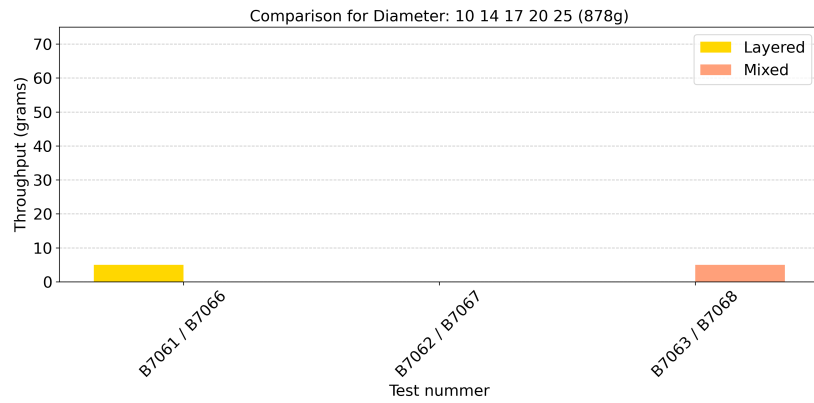


Figure H.8: Comparison for sizes 10, 14, 17, 20, and 25 with density 1400 kg/m³

Sizes 10 14 17 20 25

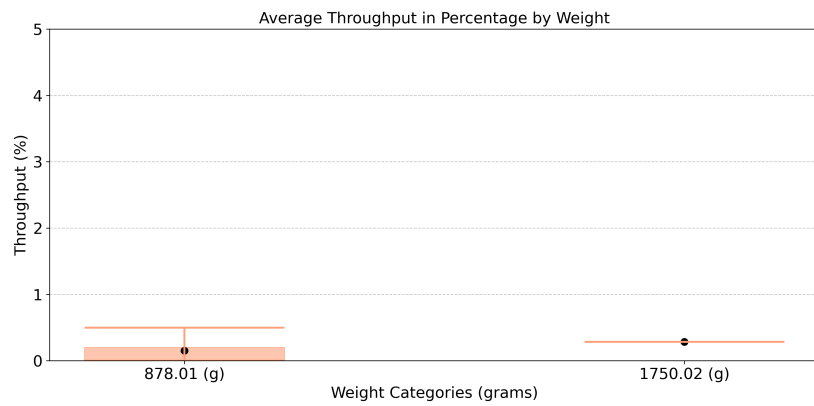


Figure H.9: Average throughput for sizes 10, 14, and 20 with density 1400 kg/m³

Summary of all tests POM

Table H.2: Summary of Throughput and Percentages for Different Sizes and Situations (POM Spheres)

Size (mm)	Repetition (-)	Layered/Mixed (-)	Amount (g)	Throughput (g)	Percentage (%)
10 15 20	3	Layered	878	0.00	0.0
10 15 20	3	Mixed	878	2.67	0.3
10 15 20	1	Mixed	1750	5.00	0.3
10 17 24	3	Layered	878	5.00	0.6
10 17 24	3	Mixed	878	48.37	5.5
10 15 17 20 24	3	Layered	878	1.67	0.2
10 15 17 20 24	3	Mixed	878	1.67	0.2

Pump Two, Series Three
2400 kg/m³

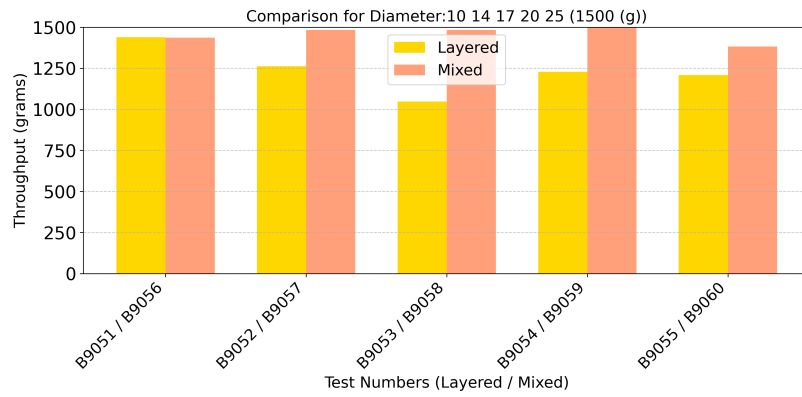


Figure H.10: Throughput comparison for sizes 10, 14, 17, 20, and 25 (1500 g) at 2400 kg/m³

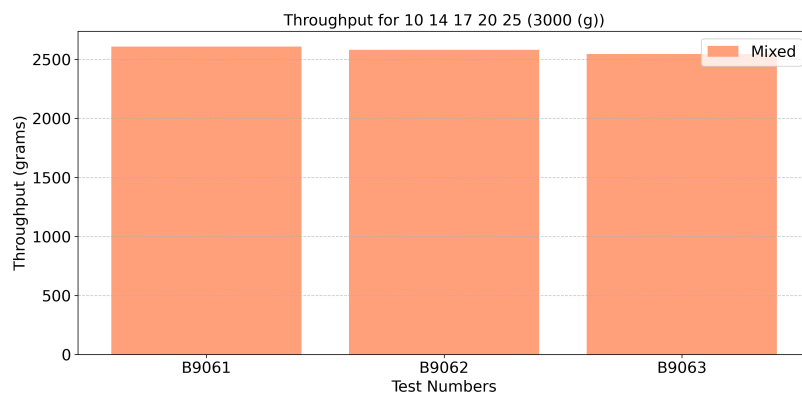


Figure H.11: Throughput comparison for sizes 10, 14, 17, 20, and 25 (3000 g) at 2400 kg/m³

Table H.3: Summary of Throughput and Percentages for Different Sizes and Situations Glass Spheres)

Size (mm)	Repetitions (-)	Layered/Mixed (-)	Weight Category (g)	Percentage Throughput (%)
10 14 17 20 25	5	Layered	1500	82.5
10 14 17 20 25	5	Mixed	1500	98.3
10 14 17 20 25	3	Mixed	3000	86.8

Pump Two, Series Three
1400 kg/m³

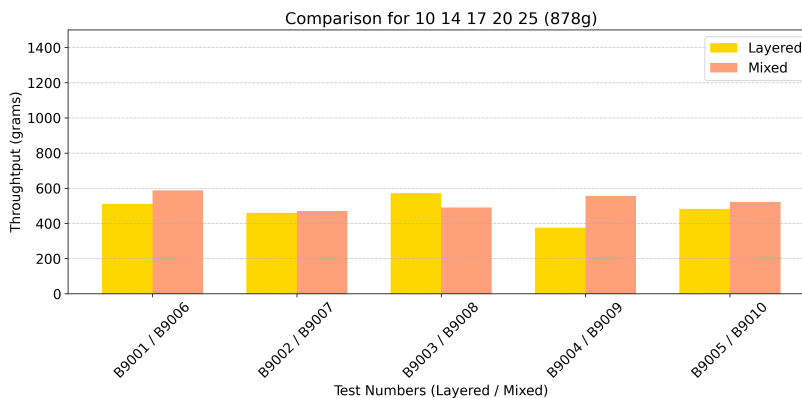


Figure H.12: Throughput comparison for sizes 10, 14, 17, 20, and 25 (878 g) at 1400 kg/m³

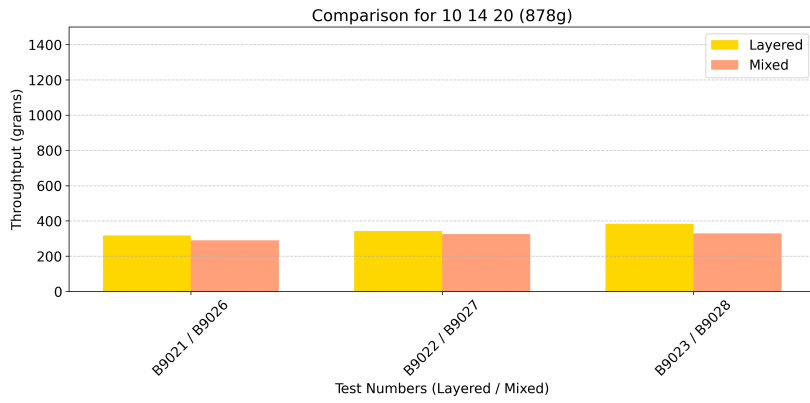


Figure H.13: Throughput comparison for sizes 10, 14, and 20 (878 g) at 1400 kg/m³

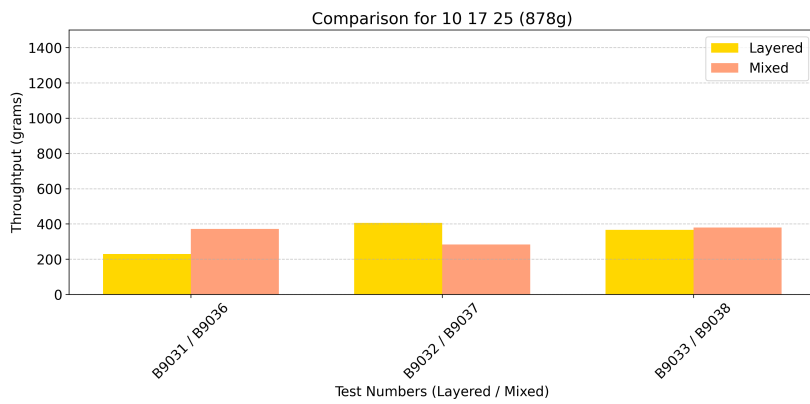


Figure H.14: Throughput comparison for sizes 10, 17, and 25 (878 g) at 1400 kg/m³

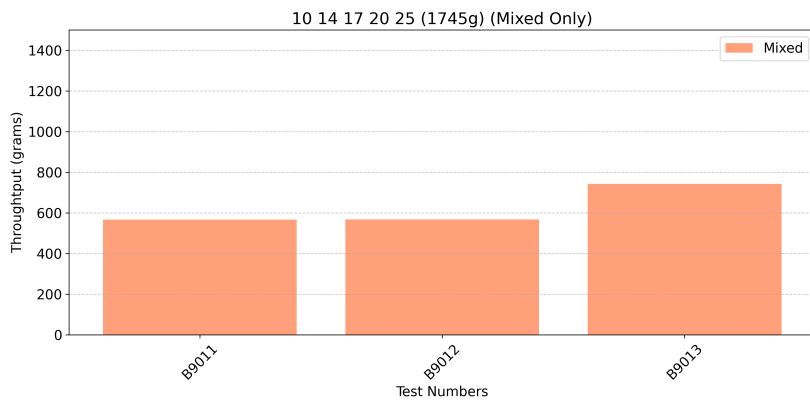


Figure H.15: Throughput comparison for sizes 10, 14, 17, 20, and 25 (1745 g) in Mixed configuration at 1400 kg/m³

Table H.4: Summary of Throughput and Percentages for Different Sizes and Situations (POM Spheres)

Size (mm)	Repetitions (-)	Layered/Mixed (-)	Weight Category (g)	Percentage Throughput (%)	
10 15 17 20 24	5	Layered	878.01	480.34	54.7
10 15 17 20 24	3	Mixed	1745	625.77	36.1
10 15 17 20 24	5	Mixed	878.01	525.26	59.8
10 15 20	3	Layered	878.01	348.33	39.8
10 15 20	3	Mixed	878.01	314.77	36.5
10 17 24	3	Layered	878.01	333.67	38.1
10 17 24	4	Mixed	878.01	344.75	39.8

Location of blockages

Table H.5: Summary of Blockages for Different Situations at Various Concentration (POM Spheres)

Situation (-)	Test Number	Density (kg/m ³)	Diameter (mm)	# Diffuser Vanes 1	# Transition 1	# Diffuser Vanes 2	# Transition 2
Layered	B9001	1400	10 14 17 20 25	1	2	-	-
Layered	B9002	1400	11 14 17 20 25	2	2	-	1
Layered	B9003	1400	12 14 17 20 25	2	3	-	1
Layered	B9004	1400	13 14 17 20 25	2	2	-	2
Layered	B9005	1400	14 14 17 20 25	4	2	-	-
Mixed	B9006	1400	15 14 17 20 25	2	2	-	1
Mixed	B9007	1400	16 14 17 20 25	2	1	-	-
Mixed	B9008	1400	17 14 17 20 25	2	1	-	-
Mixed	B9009	1400	18 14 17 20 25	2	2	1	-
Mixed	B9010	1400	19 14 17 20 25	2	2	-	1
Layered	B9021	1400	10 14 20	2	2	-	-
Layered	B9022	1400	10 14 20	2	2	-	2
Layered	B9023	1400	10 14 20	-	3	1	3
Mixed	B9026	1400	10 14 20	2	2	-	2
Mixed	B9027	1400	10 14 20	2	3	-	1
Mixed	B9028	1400	10 14 20	2	1	-	1
Layered	B9031	1400	10 17 25	4	-	-	-
Layered	B9032	1400	10 17 25	4	-	-	-
Layered	B9033	1400	10 17 25	4	-	-	-
Mixed	B9036	1400	10 17 25	2	3	-	-
Mixed	B9037	1400	10 17 25	2	2	-	-
Mixed	B9038	1400	10 17 25	3	-	-	-
Mixed	B9039	1400	10 17 25	3	-	-	3



Confirmation Tests

Confirmation Test: Distance for Terminal Settling Velocity

In Series one, the terminal settling velocity was determined by measuring the time required for a solid particle to travel a distance of 50 cm. The first measurement point was located 1.5 meters from the nodule dispenser. For accurate velocity determination, it was essential that the solid had already reached its maximum velocity at this point. To verify this, a simple test was conducted using a 1-meter-long tube marked at intervals of 20 cm, 30 cm, 40 cm, and 50 cm from the nodule dispenser.

An illustration of this test setup is shown in Figure I.1. During the test, 10 solids were released through the tube, and the time taken to pass each marked interval was recorded using high-speed camera footage. The results indicated that the velocity became constant after 30 cm. This confirmed that the 1.5-meter fallpipe used in Series One and Series Two was more than sufficient to allow the solids to reach terminal velocity.

Figure I.2 shows a frame from one of the tests, illustrating the experimental setup and measurements.

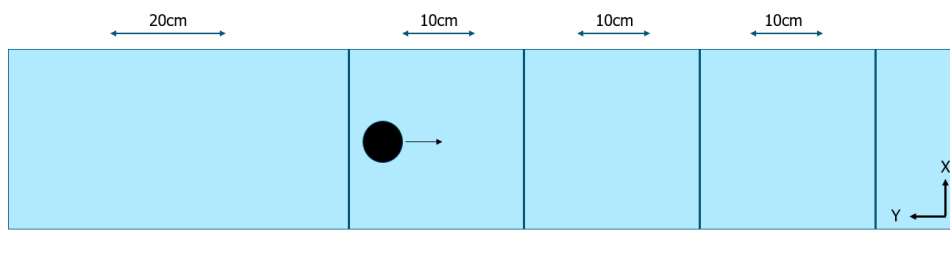


Figure I.1: Overview of Confirmation Test Setup

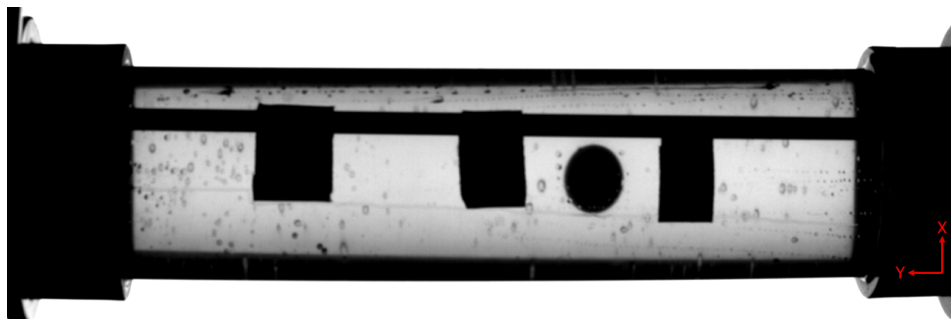


Figure I.2: Frame from Confirmation Test

Confirmation Test: Analysis of Forces Acting on Solids: Sliding, Rolling, or Resting Visual Analysis

To determine the friction coefficient between the solids and the PLA material of the model pump's core, an analysis was performed to assess whether the solids roll or slide in areas where they occasionally

become lodged. Observing this behavior using the original setup proved challenging due to the uniform color of the solids, making it difficult to differentiate between rolling and sliding.

To improve visibility, a portion of the solids was painted in two contrasting colors. This modification enables clearer identification of motion (rolling or sliding) through camera footage. An example of the visual results is shown in Figure I.3.

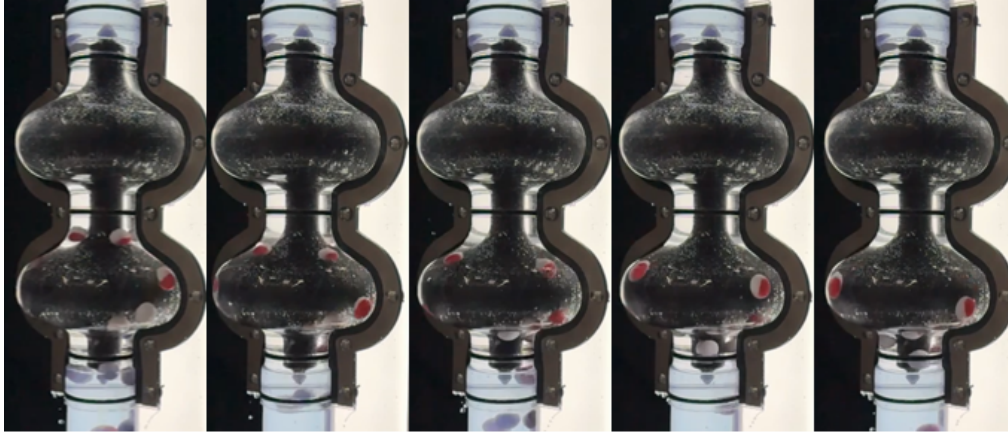


Figure I.3: Friction Test: Visual Analysis of Rolling vs Sliding

As shown in Figure I.3, the solid slides over the surface, indicating that the friction coefficient is overcome. This behavior is observed for both POM solids and glass solids.

Theoretical Analysis

To better understand whether a solid will roll, slide, or remain stationary according to theory, a force equilibrium analysis is performed. This analysis is based on experimental observations where solids were seen to remain stationary. Calculations are carried out for both glass and PLA balls, with the detailed computations available in Appendix F. The analyzed situation assumes static friction, and it is further assumed that the solid does not roll.

Sliding Condition

For a solid to slide, the following condition must hold:

$$F_{\text{parallel}} > F_{\text{friction}} \quad (I.1)$$

The force equilibrium for the scenario is illustrated in Figure I.4, where the forces acting on the solid are defined as follows:

- F_g : Gravitational force acting on the solid.
- F_b : Buoyancy force due to water.
- F_n : Normal force exerted on the solid by the inclined surface.
- F_w : Frictional force opposing motion.
- F_{parallel} : Net force acting parallel to the inclined plane, equal to the difference between gravitational and buoyant forces projected along the incline.

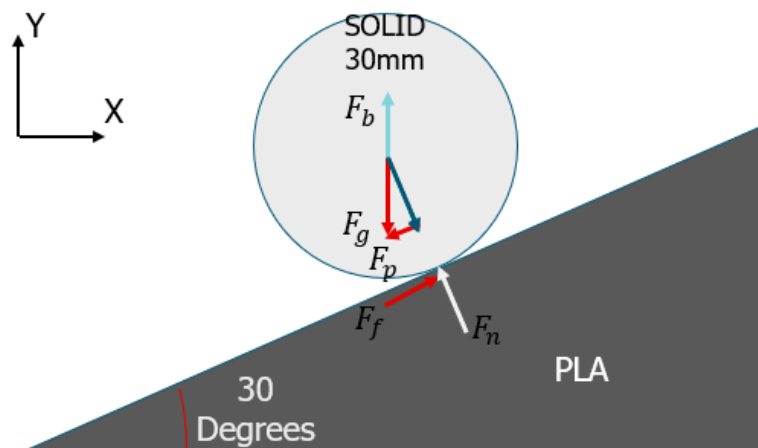


Figure I.4: Force Balance: Forces Acting on the Solid

Force Equilibrium Equations

The following equations describe the forces acting on the solid:

$$F_{\text{normal}} = F_g \cdot \cos(\theta) - F_b \cdot \cos(\theta), \quad (1.2)$$

$$F_{\text{friction}} = \mu \cdot F_{\text{normal}}, \quad (1.3)$$

$$F_{\text{parallel}} = (F_g - F_b) \cdot \sin(\theta), \quad (1.4)$$

where:

- μ : Coefficient of friction.
- θ : Inclination angle of the surface.

Coefficients

The friction coefficient (μ) used in the calculations is set to 0.45. While POM typically exhibits friction coefficients ranging from 0.2 to 0.4 when interacting with other plastics, a conservative estimate of 0.45 is chosen due to the lack of precise experimental data. Similarly, for glass beads, the same coefficient of friction is assumed, although it is likely to be slightly lower in practice.

Results and Observations

The calculations presented in Section I indicate that for both POM and glass solids, $F_{\text{parallel}} > F_{\text{friction}}$, meaning the solids will slide. The friction coefficient is insufficient to keep the solids stationary or to induce rolling motion. These theoretical findings align with experimental observations, where the solids were seen to slide rather than roll or remain stationary.

Calculation for POM Solid with Density 1400 kg/m³

Given Parameters:

$$\rho_{\text{solid}} = 1400 \text{ kg/m}^3 \quad (\text{density of the POM solid}),$$

$$d = 0.03 \text{ m} \quad (\text{diameter of the solid}),$$

$$\mu = 0.45 \quad (\text{friction coefficient}),$$

$$g = 9.81 \text{ m/s}^2 \quad (\text{gravitational acceleration}),$$

$$\rho_{\text{water}} = 1000 \text{ kg/m}^3 \quad (\text{density of water}),$$

$$\theta = 30^\circ \quad (\text{inclination angle of the surface}).$$

Step 1: Volume and Mass of the Solid

The volume of a sphere is given by:

$$V = \frac{4}{3}\pi r^3, \quad r = \frac{d}{2} = 0.015 \text{ m.}$$

$$V = \frac{4}{3}\pi(0.015)^3 = 1.413 \times 10^{-5} \text{ m}^3.$$

The mass of the solid is:

$$m = \rho_{\text{solid}} \cdot V = 1400 \cdot 1.413 \times 10^{-5} = 0.0198 \text{ kg.}$$

Step 2: Buoyancy Force (F_b)

The buoyancy force is:

$$F_b = \rho_{\text{water}} \cdot V \cdot g.$$

$$F_b = 1000 \cdot 1.413 \times 10^{-5} \cdot 9.81 = 0.1385 \text{ N.}$$

Step 3: Gravitational Force (F_g)

The gravitational force is:

$$F_g = m \cdot g.$$

$$F_g = 0.0198 \cdot 9.81 = 0.1943 \text{ N.}$$

Step 4: Normal Force (F_{normal})

The normal force is the force perpendicular to the surface:

$$F_{\text{normal}} = F_g \cdot \cos(\theta) - F_b \cdot \cos(\theta).$$

$$F_{\text{normal}} = (0.1943 - 0.1385) \cdot \cos(30^\circ).$$

$$F_{\text{normal}} = 0.0558 \cdot 0.866 = 0.0483 \text{ N.}$$

Step 5: Friction Force (F_{friction})

The friction force is:

$$F_{\text{friction}} = \mu \cdot F_{\text{normal}}.$$

$$F_{\text{friction}} = 0.45 \cdot 0.0483 = 0.0217 \text{ N.}$$

Step 6: Force Parallel to the Surface (F_{parallel})

The force parallel to the surface is:

$$F_{\text{parallel}} = (F_g - F_b) \cdot \sin(\theta).$$

$$F_{\text{parallel}} = (0.1943 - 0.1385) \cdot \sin(30^\circ).$$

$$F_{\text{parallel}} = 0.0558 \cdot 0.5 = 0.0279 \text{ N}.$$

Friction Glass Calculation for Glass Solid with Density 2400 kg/m³

Given Parameters:

$$\begin{aligned} \rho_{\text{solid}} &= 2400 \text{ kg/m}^3 \quad (\text{density of the glass solid}), \\ d &= 0.03 \text{ m} \quad (\text{diameter of the solid}), \\ \mu &= 0.45 \quad (\text{friction coefficient}), \\ g &= 9.81 \text{ m/s}^2 \quad (\text{gravitational acceleration}), \\ \rho_{\text{water}} &= 1000 \text{ kg/m}^3 \quad (\text{density of water}), \\ \theta &= 30^\circ \quad (\text{inclination angle of the surface}). \end{aligned}$$

Step 1: Volume and Mass of the Solid

The volume of a sphere is given by:

$$V = \frac{4}{3}\pi r^3, \quad r = \frac{d}{2} = 0.015 \text{ m}.$$

$$V = \frac{4}{3}\pi(0.015)^3 = 1.413 \times 10^{-5} \text{ m}^3.$$

The mass of the solid is:

$$m = \rho_{\text{solid}} \cdot V = 2400 \cdot 1.413 \times 10^{-5} = 0.0339 \text{ kg}.$$

Step 2: Buoyancy Force (F_b)

The buoyancy force is:

$$F_b = \rho_{\text{water}} \cdot V \cdot g.$$

$$F_b = 1000 \cdot 1.413 \times 10^{-5} \cdot 9.81 = 0.1385 \text{ N}.$$

Step 3: Gravitational Force (F_g)

The gravitational force is:

$$F_g = m \cdot g.$$

$$F_g = 0.0339 \cdot 9.81 = 0.3328 \text{ N}.$$

Step 4: Normal Force (F_{normal})

The normal force is the force perpendicular to the surface:

$$F_{\text{normal}} = F_g \cdot \cos(\theta) - F_b \cdot \cos(\theta).$$

$$F_{\text{normal}} = (0.3328 - 0.1385) \cdot \cos(30^\circ).$$

$$F_{\text{normal}} = 0.1943 \cdot 0.866 = 0.1681 \text{ N.}$$

—

Step 5: Friction Force (F_{friction})

The friction force is:

$$F_{\text{friction}} = \mu \cdot F_{\text{normal}}.$$

$$F_{\text{friction}} = 0.45 \cdot 0.1681 = 0.0757 \text{ N.}$$

—

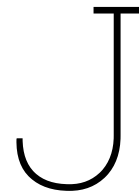
Step 6: Force Parallel to the Surface (F_{parallel})

The force parallel to the surface is:

$$F_{\text{parallel}} = (F_g - F_b) \cdot \sin(\theta).$$

$$F_{\text{parallel}} = (0.3328 - 0.1385) \cdot \sin(30^\circ).$$

$$F_{\text{parallel}} = 0.1943 \cdot 0.5 = 0.0971 \text{ N.}$$



List of tests

Fallpipe Phase One

Target (-)	Test. (-)	ρ_s (kg/m ³)	d (mm)	w_s (g)	T_{start} (s)	T_{end} (s)	Δt (s)	v_t (m/s)	\bar{v}_t (m/s)	σ^2 (-)	stop? (-)	touch? (-)
check	2001	2400	5	0.163	-6.6233	-5.3367	1.2866	0.3886	0.3886	0	Yes	
check	2002	2400	5	0.163	-4.82	-3.5	1.32	0.3788	0.3837	2.42E-05	Yes	
check	2003	2400	5	0.163	-4.0967	-2.8033	1.2934	0.3866	0.3847	1.80E-05	Yes	
check	2004	2400	5	0.162	-9.3733	-7.93	1.4433	0.3464	0.3751	0.0002876	Yes	ja
check	2005	2400	5	0.162	-7.3267	-6.2876	1.0391	0.4812	0.3963	0.002031	Yes	
check	2006	2400	5	0.163	-6.7933	-5.7533	1.04	0.4808	0.4104	0.002683	Yes	
check	2007	2400	5	0.163	-6.3367	-5.2733	1.0634	0.4702	0.4189	0.002737	Yes	
check	2008	2400	5	0.162	-8.2067	-7.1833	1.0234	0.4886	0.4276	0.002925	Yes	
check	2009	2400	5	0.16	-6.4223	-5.3667	1.0556	0.4737	0.4328	0.00281	Yes	
check	2010	2400	5	0.16	-7.39	-6.3367	1.0533	0.4747	0.4369	0.002687	Yes	
check	2011	2400	10	1.379	-7.1167	-6.137	0.9797	0.5104	0.5104	0	Yes	ja
check	2012	2400	10	1.312	-9.11	-8.1733	0.9367	0.5338	0.5221	0.0001372	Yes	ja
check	2013	2400	10	1.316	-7.937	-6.87	1.067	0.4686	0.5043	0.0007268	Yes	ja
check	2014	2400	10	1.358	-7.5	-6.49	1.01	0.4950	0.5020	0.000561	Yes	ja
check	2015	2400	10	1.29	-8.6533	-7.61	1.0433	0.4792	0.4974	0.0005313	Yes	ja
check	2016	2400	10	1.388	-6.5667	-5.56	1.0067	0.4967	0.4973	0.0004428	Yes	
check	2017	2400	10	1.34	-5.9667	-4.9367	1.03	0.4854	0.4956	0.0003967	Yes	
check	2018	2400	10	1.405	-4.71	-3.72	0.99	0.5051	0.4968	0.0003569	Yes	
check	2019	2400	10	1.414	-4.0667	-3.04	1.0267	0.4870	0.4957	0.0003267	Yes	
check	2020	2400	10	1.357	-4.3733	-3.36	1.0133	0.4934	0.4955	0.0002945	Yes	
check	2021	2400	14	3.523	-4.3267	-3.447	0.8797	0.5684	0.5684	0	Yes	ja
check	2022	2400	14	3.49	-9.12	-8.433	0.687	0.7278	0.6481	0.006354	No	
check	2023	2400	14	3.325	-8.267	-7.3667	0.9003	0.5554	0.6172	0.006147	No	ja
check	2024	2400	14	3.448	-8.6267	-7.7333	0.8934	0.5597	0.6028	0.00523	No	ja
check	2025	2400	14	3.457	-7.8733	-7.1833	0.69	0.7246	0.6272	0.006559	No	
check	2026	2400	14	3.47	-8.45	-7.7533	0.6967	0.7177	0.6423	0.006604	No	
check	2027	2400	14	3.439	-7.9467	-7.1867	0.76	0.6579	0.6445	0.00569	No	
check	2028	2400	14	3.459	-9.71	-8.87	0.84	0.5952	0.6383	0.005244	No	
check	2029	2400	14	3.452	-8.11	-7.2633	0.8467	0.5905	0.6330	0.004887	Yes	
check	2030	2400	14	3.363	-8.4833	-7.7867	0.6966	0.7178	0.6415	0.005045	No	
check	2031	2400	20	12.228	-7.81	-7.2367	0.5733	0.8721	0.8721	0	Yes	
check	2032	2400	20	11.868	-8.3333	-7.6533	0.68	0.7353	0.8037	0.004682	Yes	
check	2033	2400	20	11.791	-8.9167	-8.2467	0.67	0.7463	0.7846	0.003855	Yes	
check	2034	2400	20	12.018	-8.4367	-7.8633	0.5734	0.8720	0.8064	0.004324	Yes	
check	2035	2400	20	11.755	-8.78	-8.22	0.56	0.8929	0.8237	0.004655	Yes	
check	2036	2400	20	11.852	-8.2567	-7.6867	0.57	0.8772	0.8326	0.004276	Yes	
check	2037	2400	20	12.055	-8.9467	-8.3033	0.6434	0.7771	0.8247	0.004042	Yes	
check	2038	2400	20	12.029	-11.4133	-10.8467	0.5666	0.8825	0.8319	0.003902	Yes	
check	2039	2400	20	12.116	-9.1567	-8.6067	0.55	0.9091	0.8405	0.004057	Yes	
check	2040	2400	20	11.827	-8.4467	-7.8833	0.5634	0.8875	0.8452	0.00385	Yes	
check	2041	2400	25	20.056	-7.8967	-7.2633	0.6334	0.7894	0.7894	0	Yes	ja
check	2042	2400	25	19.21	-8.1933	-7.63	0.5633	0.8876	0.8385	0.002413	Yes	
check	2043	2400	25	19.163	-9.1833	-8.48	0.7033	0.7109	0.7960	0.005225	No	ja
check	2044	2400	25	20.033	-9.4267	-8.8433	0.5834	0.8570	0.8112	0.004618	Yes	
check	2045	2400	25	19.418	-8.3367	-7.69	0.6467	0.7732	0.8036	0.003927	Yes	
check	2047	2400	25	19.14	-8.6733	-8.09	0.5833	0.8572	0.8126	0.003671	Yes	ja
check	2048	2400	25	20.153	-8.7033	-8.02	0.6833	0.7317	0.8010	0.003946	Yes	ja

Continued on next page...

Target (-)	Test. (-)	ρ_s (kg/m ³)	d (mm)	w_s (g)	T_{start} (s)	T_{end} (s)	Δt (s)	v_t (m/s)	\bar{v}_t (m/s)	σ^2 (-)	stop? (-)	touch? (-)
check	2049	2400	25	20.017	-8.8133	-8.25	0.5633	0.8876	0.8118	0.004273	Yes	
check	2050.2	2400	25	19.183	-10.6467	-10.0467	0.6	0.8333	0.8142	0.003844	Yes	ja
check	2050	2400	25	19.521	-8.87	-8.25703	0.61297	0.8157	0.8144	0.00346	Yes	
check	2051	2400	30	32.378	-8.4233	-7.8133	0.61	0.8197	0.8197	0	Yes	
check	2052	2400	30	33.102	-8.5833	-7.9367	0.6466	0.7733	0.7965	0.000538	Yes	
check	2053	2400	30	32.912	-9.7067	-9.1633	0.5434	0.9201	0.8377	0.003757	Yes	
check	2054	2400	30	33.116	-8.83	-8.2367	0.5933	0.8427	0.8390	0.002822	Yes	
check	2055	2400	30	32.629	-10.0433	-9.47	0.5733	0.8721	0.8456	0.002434	Yes	
check	2056	2400	30	32.957	-7.4967	-6.88	0.6167	0.8108	0.8398	0.002197	Yes	
check	2057	2400	30	33.1	-7.7433	-7.1767	0.5666	0.8825	0.8459	0.002106	Yes	
check	2058	2400	30	33.021	-9.5733	-8.9267	0.6466	0.7733	0.8368	0.002419	Yes	ja
check	2059	2400	30	32.988	-8.5	-7.9067	0.5933	0.8427	0.8375	0.002154	Yes	
check	2060	2400	30	32.924	-7.42	-6.83	0.59	0.8475	0.8385	0.001948	Yes	ja

Fallpipe 1400 kg/m³

Target (-)	Test. (-)	ρ_s (kg/m ³)	d (mm)	w_s (g)	T_{start} (s)	T_{end} (s)	Δt (s)	v_t (m/s)	\bar{v}_t (m/s)	σ^2 (-)	stop? (-)	touch? (-)
check	3001	1400	5	0.091	-5.5233	-3.3567	2.1666	0.2308	0.2308	0	Yes	
check	3002	1400	5	0.0902	-6.0767	-3.8133	2.2634	0.2209	0.2258	2.44E-05	Yes	
check	3003	1400	5	0.093	-5.09	-2.8533	2.2367	0.2235	0.2251	1.74E-05	Yes	
check	3004	1400	5	0.092	-5.8	-3.48	2.32	0.2155	0.2227	3.02E-05	Yes	ja
check	3005	1400	5	0.09	-6.2367	-3.9867	2.25	0.2222	0.2226	2.42E-05	Yes	
check	3006	1400	5	0.091	-6.933	-4.71	2.223	0.2249	0.2230	2.09E-05	Yes	
check	3007	1400	5	0.092	-5.5767	-3.533	2.0437	0.2447	0.2261	7.54E-05	Yes	
check	3008	1400	5	0.092	-6.5	-4.267	2.233	0.2239	0.2258	6.65E-05	Yes	
check	3009	1400	5	0.092	-6.0533	-3.8	2.2533	0.2219	0.2254	6.06E-05	Yes	
check	3010	1400	5	0.09	-6.0133	-3.7967	2.2166	0.2256	0.2254	5.46E-05	Yes	
check	3011	1400	10	0.718	-8.0133	-6.5	1.5133	0.3304	0.3304	0	Yes	
check	3012	1400	10	0.704	-5.9467	-4.4233	1.5234	0.3282	0.3293	1.20E-06	Yes	
check	3013	1400	10	0.719	-6.4433	-4.9567	1.4866	0.3363	0.3317	1.18E-05	Yes	
check	3014	1400	10	0.714	-7.1567	-4.9667	2.19	0.2283	0.3058	0.00201	Yes	ja
check	3015	1400	10	0.707	-6.1967	-4.6867	1.51	0.3311	0.3109	0.00171	Yes	
check	3016	1400	10	0.72	-6.39	-4.8833	1.5067	0.3319	0.3144	0.00149	Yes	
check	3017	1400	10	0.714	-6.2433	-4.7367	1.5066	0.3319	0.3169	0.00131	Yes	
check	3018	1400	10	0.715	-6.1667	-4.6733	1.4934	0.3348	0.3191	0.00118	Yes	
check	3019	1400	10	0.715	-6.06	-4.5433	1.5167	0.3297	0.3203	0.00106	Yes	
check	3020	1400	10	0.716	-6.24	-3.9	2.34	0.2137	0.3096	0.00198	Yes	ja
check	3021	1400	14	2.375	-7.6767	-6.4	1.2767	0.3916	0.3916	0	Yes	
check	3022	1400	14	2.381	-6.2367	-4.94	1.2967	0.3856	0.3886	9.12E-06	Yes	
check	3023	1400	14	2.379	-7.7633	-6.4567	1.3066	0.3827	0.3866	1.39E-05	Yes	
check	3024	1400	14	2.389	-8.0533	-6.7633	1.29	0.3876	0.3869	1.06E-05	Yes	
check	3025	1400	14	2.399	-7.9233	-6.63	1.2933	0.3866	0.3868	8.51E-06	Yes	
check	3026	1400	14	2.399	-8.3433	-7.0167	1.3266	0.3769	0.3852	2.08E-05	Yes	
check	3027	1400	14	2.389	-7.5633	-6.2467	1.3166	0.3798	0.3844	2.14E-05	Yes	
check	3028	1400	14	2.392	-7.64	-6.3367	1.3033	0.3836	0.3843	1.88E-05	Yes	
check	3029	1400	14	2.403	-7.2767	-6.0067	1.27	0.3937	0.3853	2.54E-05	Yes	
check	3030	1400	14	2.388	-8.3633	-6.42	1.9433	0.2573	0.3725	0.00150	Yes	ja
check	3031	1400	20	5.628	-11.65	-10.3967	1.2533	0.3989	0.3989	0	Yes	ja
check	3032	1400	20	5.63	-7.4867	-5.8633	1.6234	0.3080	0.3535	0.00207	Yes	ja
check	3033	1400	20	5.623	-9.32	-8.0633	1.2567	0.3979	0.3683	0.00182	Yes	ja
check	3034	1400	20	5.663	-8.8033	-7.6533	1.15	0.4348	0.3849	0.00219	Yes	ja
check	3035	1400	20	5.63	-5.76	-4.4067	1.3533	0.3695	0.3818	0.00179	Yes	ja
check	3036	1400	20	5.641	-9.6567	-8.4967	1.16	0.4310	0.3900	0.00183	Yes	ja
check	3037	1400	20	5.609	-5.6567	-4.46	1.1967	0.4178	0.3940	0.00166	Yes	ja
check	3038	1400	20	5.623	-9.7	-8.5067	1.1933	0.4190	0.3971	0.00152	Yes	ja
check	3039	1400	20	5.621	-6.6433	-4.9733	1.67	0.2994	0.3863	0.00230	Yes	ja
check	3040	1400	20	5.628	-6.4033	-5.2033	1.2	0.4167	0.3893	0.00215	Yes	
check	3041	1400	25	9.761	-11.0767	-9.57	1.5067	0.3319	0.3319	0	Yes	ja
check	3042	1400	25	9.854	-6.3833	-4.9333	1.45	0.3448	0.3383	4.21E-05	Yes	ja
check	3043	1400	25	9.798	-10.6033	-9.4367	1.1666	0.4286	0.3684	0.00184	Yes	ja
check	3044	1400	25	9.799	-6.5333	-5.1833	1.35	0.3704	0.3689	0.00138	Yes	ja
check	3045	1400	25	9.783	-11.1633	-10.01	1.1533	0.4335	0.3818	0.00177	Yes	
check	3046	1400	25	9.802	-7.6967	-6.2867	1.41	0.3546	0.3773	0.00158	Yes	ja
check	3047	1400	25	9.819	-9.72	-8.6467	1.0733	0.4659	0.3899	0.00231	Yes	
check	3048	1400	25	9.793	-5.34	-3.8667	1.4733	0.3394	0.3836	0.00230	Yes	
check	3049	1400	25	9.896	-10.1367	-8.9667	1.17	0.4274	0.3885	0.00224	Yes	
check	3050	1400	25	9.767	-5.7433	-4.25	1.4933	0.3348	0.3831	0.00227	Yes	

Continued on next page...

Target (-)	Test. (-)	ρ_s (kg/m ³)	d (mm)	w_s (g)	T_{start} (s)	T_{end} (s)	Δt (s)	v_t (m/s)	\bar{v}_t (m/s)	σ^2 (-)	stop? (-)	touch? (-)
check	3051	1400	30	18.905	-8.1633	-6.9567	1.2066	0.4144	0.4144	0	Yes	
check	3052	1400	30	18.867	-6.7433	-5.45	1.2933	0.3866	0.4005	0.00019	Yes	
check	3053	1400	30	18.994	-9.8033	-8.5033	1.3	0.3846	0.3952	0.00018	Yes	
check	3054	1400	30	18.894	-6.9333	-5.5667	1.3666	0.3659	0.3879	0.00030	Yes	
check	3055	1400	30	18.897	-10.3533	-8.9967	1.3566	0.3686	0.3840	0.00030	Yes	
check	3056	1400	30	18.832	-8.0967	-6.6633	1.4334	0.3488	0.3781	0.00042	Yes	
check	3057	1400	30	18.865	-6.04	-4.8167	1.2233	0.4087	0.3825	0.00048	Yes	
check	3058	1400	30	18.93	-9.0833	-7.93	1.1533	0.4335	0.3889	0.00070	Yes	
check	3059	1400	30	18.91	-7.6933	-6.34	1.3533	0.3695	0.3867	0.00066	Yes	
check	3060	1400	30	18.973	-5.8633	-4.4767	1.3866	0.3606	0.3841	0.00066	Yes	

Fallpipe Phase Two 2400 kg/m³

d (mm)	C_i (kg/m ³)	h_b (cm)	\bar{h}_b (cm)	w_s (g)	\bar{w}_s (g)
20	46	10	10.5	862	879
20	46	10	10.5	862	855.5
20	46	20	20.2	1725	1692.5
20	46	20	20.5	1725	1680
20	26	10	10.7	487.9	522.4
20	26	10	10.5	487.9	498
20	26	10	10.5	487.9	500.1
20	26	20	20	975.0	1012.9
20	26	20	20	975.0	978.3
20	26	20	20.3	975.0	991.5
10	26	10	10.5	484.8	476.6
10	26	10	10.5	484.8	470.9
10	26	10	-	484.8	-
10	26	20	20	975.0	974.3
10	26	20	20	975.0	974
10	26	20	20	975.0	973
10	46	10	10	862	880.2
10	46	10	9.8	862	871.8
10	46	10	9.9	862	871.2
10	46	20	20	1725	1762.4
10	46	20	19.6	1725	1717.3
10	46	20	-	1725	-

1400 kg/m³

d (mm)	C_i (kg/m ³)	h_b (cm)	\bar{h}_b (cm)	w_s (g)	\bar{w}_s (g)
20	26	10	10	284.5	263.6
20	26	10	10.5	284.5	280.4
20	26	10	10.5	284.5	291.2
20	26	20	20.6	569.1	534.5
20	26	20	20	569.1	506.8
20	26	20	21	569.1	564
20	46	10	10.5	503.16	452
20	46	10	11	503.16	480
20	46	10	-	503.16	-
20	46	20	21	1006.32	890.5
20	46	20	20.5	1006.32	913.9
20	46	20	-	1006.32	-
10	26	10	-	284.5	-
10	26	10	-	284.5	-
10	26	10	-	284.5	-
10	26	20	19.5	569.1	571
10	26	20	20	569.1	568
10	26	20	19.5	569.1	572
10	46	10	-	503.16	-
10	46	10	-	503.16	-
10	46	10	-	503.16	-
10	46	20	20	1006.32	1008

Continued on next page...

d (mm)	C_i (kg/m³)	h_b (cm)	\bar{h}_b (cm)	w_s (g)	\bar{w}_s (g)
10	46	20	20	1006.32	1007
10	46	20	-	1006.32	-

Pump One
Pump One Phase One
1400 kg/m³

Test (-)	ρ_s (kg/m³)	d (mm)	C_i (kg/m³)	h_b (cm)	\bar{h}_b (cm)	w_s (g)	\bar{w}_s (g)	T (-)	Obstr. (-)	Remarks (-)	Count (-)
6001	1400	10mm	26%	10	-	284	286	-	No	-	-
6002_1	1400	10mm	26%	20	-	569	569	-	No	-	-
6003	1400	10mm	46%	10	-	503	506	-	No	-	-
6004	1400	10mm	46%	20	-	1006	1008	-	No	-	-
6005	1400	20mm	26%	10	-	284	292	-	No	-	-
6006	1400	20mm	26%	20	-	569	568	-	No	-	-
6007	1400	20mm	46%	10	-	503	506	-	No	-	-
6008	1400	20mm	46%	20	-	1006	1002	-	No	-	-
6009	1400	25mm	26%	10	11	284	286	-	No	-	-
6010	1400	25mm	26%	20	23	569	568	-	No	-	-
6011	1400	25mm	46%	10	-	503	-	-	No	-	-
6012	1400	25mm	46%	20	-	1006	-	-	No	-	-
6013	1400	10mm	55%	10	10	599	602	-	No	-	-
6014	1400	10mm	55%	20	19.5	1198	1197	-	No	-	-
6015	1400	20mm	55%	10	10.5	599	604	-	No	-	-
6016	1400	20mm	55%	20	17	1198	978	-	No	-	-
6017	1400	25mm	55%	10	10.5	599	603	-	No	-	-
6018	1400	25mm	55%	20	18.5	1198	1012	-	No	-	-
6017	1400	30mm	26%	10	12	284	284	-	Yes	Obstruction 5 balls	-
6018	1400	30mm	26%	20	14	569	560	-	Yes	Obstruction 6 balls	-
6019	1400	30mm	55%	10	14	599	606	-	Yes	Obstruction 5 balls	-
6020	1400	30mm	55%	20	20	1198	1016	-	Yes	Obstruction 6 balls	-
6020-2	1400	30mm	55%	20	20	1198	1016	-	Yes	Obstruction 6 balls	-
6050	1400	10 20	46%	16	-	1000	-	-	No	-	-
6051	1400	10 20 25	46%	16	-	1000	-	-	No	-	-
6052	1400	11 20 25	46%	16	-	1000	-	-	No	-	-

Pump One Phase Two

Test (-)	ρ_s (kg/m³)	d (mm)	C_i (kg/m³)	h_b (cm)	\bar{h}_b (cm)	w_s (g)	\bar{w}_s (g)	T_{start} (s)	T_{end} (s)	Δt (s)	(Obstruction) (-)	(Solids) (-)	(W) (g)
7001	1400	30mm	55%	20	19	1199	1006	-12.1667	-1.726	10.4407	Yes	3.00	56.73
7002	1400	30mm	55%	20	19	1199	1010	-11.62	-1.81	9.81	Yes	3.00	56.73
7003	1400	30mm	55%	20	19	1199	1010	-12.2167	-2.7467	9.47	Yes	3.00	56.73
7004	1400	30mm	55%	20	19	1199	996	-11.8933	-3.4567	8.4366	Yes	3.00	56.73
7005	1400	30mm	55%	20	19	1199	989	-12.8633	-1.4867	11.3766	Yes	3.00	56.73
7006	1400	30mm	55%	20	19	1199	1022	-10.3033	-1.3367	8.9666	Yes	2.00	37.82
7007	1400	30mm	55%	20	19	1199	1001	-10.97	-1.8433	9.1267	Yes	3.00	56.73
7008	1400	30mm	55%	20	18	1199	975	-11.9233	-2.8067	9.1166	Yes	3.00	56.73
7009	1400	30mm	55%	20	18.5	1199	976	-13.3567	-3.5867	9.77	Yes	3.00	56.73
7010	1400	30mm	55%	20	18	1199	983	-12.1333	-3.6067	8.5266	Yes	3.00	56.73
7011	1400	30mm	26%	10	12	284	283	-10.62	-5.23	5.39	Yes	3.00	56.73
7012	1400	30mm	26%	10	13	284	282	-12.433	-6.5133	5.9197	Yes	4.00	75.64
7013	1400	30mm	26%	10	12	284	283	-11.7033	-6.33	5.3733	Yes	2.00	37.82
7014	1400	30mm	26%	10	13	284	284	-12.3933	-6.0467	6.3466	Yes	2.00	37.82
7015	1400	30mm	26%	10	12	284	284	-11.48	-6.0933	5.3867	Yes	2.00	37.82
7016	1400	30mm	26%	10	13	284	286	-10.93	-5.2767	5.6533	Yes	1.00	18.91
7017	1400	30mm	26%	10	13	284	284	-10.88	-4.9167	5.9633	Yes	2.00	37.82
7018	1400	30mm	26%	10	12	284	284	-10.8833	-5.56	5.3233	Yes	2.00	37.82
7019	1400	30mm	26%	10	12	284	286	-11.2	-5.433	5.767	Yes	1.00	18.91
7020	1400	30mm	26%	10	13	284	284	-13.2067	-7.97	5.2367	Yes	3.00	56.73
7021	1400	30mm	55%	10	10	599.9	493	-10.53	-3.1767	7.3533	Yes	3.00	56.73
7022	1400	30mm	55%	10	11	599.9	513	-12	-4.0133	7.9867	Yes	4.00	75.64
7023	1400	30mm	55%	10	10	599.9	488	-10.66	-2.7933	7.8667	Yes	2.00	37.82
7024	1400	30mm	55%	10	10	599.9	503	-10.4133	-4.5433	5.87	Yes	1.00	18.91
7025	1400	30mm	55%	10	10	599.9	474	-10.49	-2.5	7.99	Yes	3.00	56.73

Continued on next page...

Test (-)	ρ_s (kg/m ³)	d (mm)	C_i (kg/m ³)	h_b (cm)	\bar{h}_b (cm)	w_s (g)	\bar{w}_s (g)	T_{start} (s)	T_{end} (s)	Δt (s)	(Obstruction) (-)	(Solids) (-)	(W) (g)
7026	1400	30mm	55%	10	10	599.9	492	-10.91	-3.3167	7.5933	No	0.00	0.00
7027	1400	30mm	55%	10	9.5	599.9	471	-10.5467	-2.26	8.2867	Yes	1.00	18.91
7028	1400	30mm	55%	10	9.5	599.9	474	-10.5	-1.96	8.54	No	0.00	0.00
7029	1400	30mm	55%	10	9.5	599.9	470	-11.1567	-4.3267	6.83	No	0.00	0.00
7030	1400	30mm	55%	10	9.5	599.9	475	-11.2667	-3.0867	8.18	No	0.00	0.00
7031	1400	30mm	26%	20	22	569	470	-10.53	-3.1767	7.3533	Yes	5.00	94.55
7032	1400	30mm	26%	20	21	569	472	-11.4233	-4.7367	6.6866	Yes	2.00	37.82
7033	1400	30mm	26%	20	20	569	473	-12.0367	-3.4533	8.5834	No	0.00	0.00
7034	1400	30mm	26%	20	21	569	473	-10.92	-3.6367	7.2833	Yes	1.00	18.91
7035	1400	30mm	26%	20	21	569	490	-12.1833	-4.0267	8.1566	No	0.00	0.00
7036	1400	30mm	26%	20	22	569	492	-12.97	-5.62	7.35	No	0.00	0.00
7037	1400	30mm	26%	20	22	569	475	-12.3367	-5.0933	7.2434	Yes	1.00	18.91
7038	1400	30mm	26%	20	24	569	607	-10.89	-3.61	7.28	Yes	3.00	56.73
7039	1400	30mm	26%	20	22	569	502	-10.5567	-4.42	6.1367	Yes	4.00	75.64
7040	1400	30mm	26%	20	21	569	510	-10.74	-2.1067	8.6333	No	0.00	0.00

1400 kg/m³ Mixed

Test (-)	ρ_s (kg/m ³)	d (mm)	C_i (kg/m ³)	\bar{h}_b (cm)	w_s (g)	\bar{w}_s (g)	T_{start} (s)	T_{end} (s)	Δt (s)	(Obstruction) (-)	(Solids) (-)	(W) (g)
7051	1400	10 20 30	55%	-	1503	-16.216	-4.84	11.376	-	No	gemixt	-
7052	1400	11 20 30	55%	-	1505	-12.564	-1.264	11.3	-	No	gemixt	-
7053	1400	12 20 30	55%	-	1508	-13.708	-2.384	11.324	-	No	gemixt	-
7054	1400	13 20 30	55%	-	1502	-12.696	-0.956	11.74	-	Yes	gemixt	2
7054.2	1400	14 20 30	55%	-	1506	-12.048	-0.9	11.148	11.3776	No	gemixt	-
7055	1400	15 20 30	55%	25	1500	-12.6467	-2.2533	10.3934	-	Yes	gelaagd	3
7056	1400	16 20 30	55%	25.5	1505	-11.5167	-0.9933	10.5234	-	No	gelaagd	-
7057	1400	17 20 30	55%	25	1498	-11.2033	-0.5633	10.64	-	No	gelaagd	-
7058	1400	18 20 30	55%	-	1506	-10.812	-0.628	10.184	-	No	gelaagd	-
7059	1400	19 20 30	55%	-	1512	-10.756	-0.644	10.112	10.37056	No	gelaagd	-
7061	-	20 20 30	55%	-	-	-	-	-	-	mix	-	-
7066	-	10 14 20 25 30	55%	26	1502	-11.736	-1.148	10.588	-	No	gelaagd	-
7067	-	12 14 20 25 30	55%	26	1502	-11.092	-1.084	10.008	-	No	gelaagd	-
7068	-	14 14 20 25 30	55%	26	1507	-10.69	-0.648	10.042	-	No	gelaagd	-
7069	-	16 14 20 25 30	55%	26	1508.638	-11.16	-0.716	10.444	-	No	gelaagd	-
7070	-	18 14 20 25 30	55%	26	1508.19	-11.24	-1.125	10.114	10.2394	No	gelaagd	-
7071	-	20 14 20 25 30	55%	23	1502	-11.976	-1.516	10.46	-	No	mix	-
7072	-	22 14 20 25 30	55%	24	1502	-11.432	-1.212	10.22	-	No	mix	-
7073	-	24 14 20 25 30	55%	23	1507	-11.416	-1.036	10.38	-	No	mix	-
7074	-	26 14 20 25 30	55%	23	1507	-10.836	-0.572	10.264	-	No	mix	-
7074.3	-	28 14 20 25 30	55%	24	1509	-12.712	-1.72	10.992	10.4632	Yes	mix	1
7075	-	30 14 20 25 30	55%	45	3000	-15.964	-0.0668	15.8972	-	No	mix	-
7076	-	32 14 20 25 30	55%	46	3000	-15.972	-0.708	15.264	-	No	mix	-
7077	-	34 14 20 25 30	55%	-	3000	-15.648	-0.308	15.34	15.5004	No	mix	-

Pump One Phase Three

2400 kg/m³

Test. (-)	ρ_s (kg/m ³)	d (mm)	C_i (kg/m ³)	h_b (cm)	w_s (g)	\bar{w}_s (g)	T_{start} (s)	T_{end} (s)	Δt (s)	(Obstruction) (-)	(Solids) (-)
9111	2400	30	55%	10	1028	1019	-9.544	-6.2	3.344	yes	6
9112	2400	30	55%	10	1028	1019	-7.752	-3.94	3.812	yes	3
9113	2400	30	55%	10	1028	1019	-9.052	-5.656	3.396	Yes	1
9114	2400	30	55%	10	1028	1028	-10.1	-6.976	3.124	yes	2
9114	2400	30	55%	10	1028	995	-10.62	-7.516	3.104	yes	4
9121	2400	30	26%	10	478	461	-9.104	-6.368	2.736	yes	1
9122	2400	30	26%	10	478	476	-7.37	-4.884	2.486	No	0
9123	2400	30	26%	10	478	459	-6.548	-4.132	2.416	Yes	3
9124	2400	30	26%	10	478	464	-7.2	-4.796	2.404	no	0
9125	2400	30	26%	10	478	464	-7.308	-4.108	3.2	no	0
9130	2400	10 20 30	55%	-	900	-	-11.012	-6.5	4.512	no	-
9131	2400	11 20 30	55%	-	900	-	-6.388	-1.968	4.42	yes	2
9132	2400	12 20 30	55%	-	900	-	-6.896	-2.252	4.644	yes	2

1400 kg/m³

Test (-)	ρ_s (kg/m ³)	d (mm)	C_i (kg/m ³)	h_b (cm)	\bar{h}_b (cm)	w_s (g)	\bar{w}_s (g)	T_{start} (s)	T_{end} (s)	Δt (s)	(Obstruction) (-)	(Solids) (-)	(W) (g)
9011	1400	30mm	55%	10	13	599	605	-11.824	-5.16	6.664	yes	7	
9012	1400	30mm	55%	10	13	599	606	-9.888	-1.396	8.492	yes	8	
9013	1400	30mm	55%	10	13	599	606	-9.2	-2.644	6.556	yes	10	
9016	1400	20mm	55%	10	11	599	601	-6.76	-0.824	5.936	No	-	
9017	1400	25mm	55%	10	11.5	599	601	-8.116	-2.144	5.972	No	-	
9018	1400	25mm	55%	10	11.5	599	599	-8.14	-2.304	5.836	No	-	
9019	1400	20mm	55%	20	-	1200	950	-9.876	-2.316	7.56	No	-	
9031	1400	10 20 30	55%	20	-	-	-	-10.156	0.972	11.128	ja	-	
9032	1400	10 20 30	55%	20	16	-	-	-	-	-	ja	-	
9033	1400	10 20 30	55%	20	-	-	-	-	-	-	ja	-	
9111	2400	30mm	55%	10	-	1028	1019	-9.544	-6.2	3.344	yes	6	
9112	2400	30mm	55%	10	-	1028	1019	-7.752	-3.94	3.812	yes	3	
9113	2400	30mm	55%	10	-	1028	1019	-9.052	-5.656	3.396	Yes	1	
9114	2400	30mm	55%	10	-	1028	1028	-10.1	-6.976	3.124	yes	2	
9115	2400	30mm	55%	10	-	1028	995	-10.62	-7.516	3.104	yes	4	
9121	2400	30	26%	10	-	478	461	-9.104	-6.368	2.736	yes	1	
9122	2400	30	26%	10	-	478	476	-7.37	-4.884	2.486	No	0	
9123	2400	30	26%	10	-	478	459	-6.548	-4.132	2.416	Yes	3	
9124	2400	30	26%	10	-	478	464	-7.2	-4.796	2.404	No	0	
9125	2400	30	26%	10	-	478	464	-7.308	-4.108	3.2	No	0	
9130	2400	10 20 30	55%	10	-	900	-	-11.012	-6.5	4.512	No	0	
9131	2400	10 20 30	55%	10	-	900	-	-6.388	-1.968	4.42	yes	2	
9132	2400	10 20 30	55%	10	-	900	-	-6.896	-2.252	4.644	yes	2	

Pump Two
Pump Two Phase One
2400 kg/m³

Test N. (-)	ρ_s (kg/m ³)	d (mm)	C_i (kg/m ³)	h_b (cm)	\bar{h}_b (cm)	w_s (g)	\bar{w}_s (g)	Solids Passing Pump? (-)	How Many (-)
B6101	2400	10mm	26%	10	10	487.87	488	No	0
B6102	2400	10mm	26%	20	21	975.75	976	No	0
B6103	2400	10mm	55%	10	10	1028.44	1029	No	0
B6104	2400	10mm	55%	20	20	2056.89	2055	Yes	35
B6105	2400	15mm	26%	10	11	487.87	788	Yes	7
B6106	2400	15mm	26%	20	21	975.75	978	Yes	8
B6107	2400	15mm	55%	10	10	1028.44	1029	Yes	7
B6108	2400	15mm	55%	20	20	2056.89	2040	Yes	35
B6109	2400	20mm	26%	10	11	487.87	487	Yes	26
B6110	2400	20mm	26%	20	20	975.75	976	Yes	11
B6111	2400	20mm	55%	10	10	1028.44	1026	Yes	13
B6112	2400	20mm	55%	20	18	2056.89	2048	Yes	18
B6113	2400	25mm	26%	10	-	487.87	490	Yes	15
B6114	2400	25mm	26%	20	24	975.75	960	Yes	16
B6115	2400	25mm	55%	10	-	1028.44	960	Yes	20

1400 kg/m³

Test N. (-)	ρ_s (kg/m ³)	d (mm)	C_i (kg/m ³)	h_b (cm)	\bar{h}_b (cm)	w_s (g)	\bar{w}_s (g)	Solids Passing Pump? (-)	How Many (-)
B6001	1400	10mm	26%	10	9.8	284.59	284	No	0
B6002	1400	10mm	26%	20	20.5	569.19	572	No	0
B6003	1400	10mm	55%	10	10	599.928	598	No	0
B6004	1400	10mm	55%	20	19	1199.85	1198	No	0
B6005	1400	15mm	26%	10	10.5	284.59	285	No	0
B6006	1400	15mm	26%	20	19.8	569.19	568	No	0
B6007	1400	15mm	55%	10	9	599.928	600	No	0
B6008	1400	15mm	55%	20	-	1199.85	1000	No	0
B6009	1400	20mm	26%	10	9	284.59	280	Yes	7
B6010	1400	20mm	26%	20	22	569.19	565	Yes	6
B6011	1400	20mm	55%	10	9.8	599.928	601	Yes	7
B6012	1400	20mm	55%	20	17	1199.85	970	Yes	9
B6013	1400	25mm	26%	10	11	284.59	286	Yes	13
B6014	1400	25mm	26%	20	22	569.19	568	Yes	14
B6015	1400	25mm	55%	10	-	599.928	599	Yes	21

Continued on next page...

Test N. (-)	ρ_s (kg/m ³)	d (mm)	C_i (kg/m ³)	h_b (cm)	\bar{h}_b (cm)	w_s (g)	\bar{w}_s (g)	Solids Passing Pump? (-)	How Many (-)
B6016	1400	25mm	55%	20	18	1199.85	960	Yes	32

Pump Two Phase Two 2400 kg/m³

Situation (-)	Test N. (-)	ρ_s (kg/m ³)	d (mm)	w_s (g)	C_i (kg/m ³)	\bar{h}_b (cm)	Throughput (g)	Avg Throughput (g)
Layered	B8051	2400	10 17 25	1500	55%	13	35.5	–
Layered	B8052	2400	10 17 25	1500	55%	14.5	31.3	–
Layered	B8053	2400	10 17 25	1500	55%	15	27.6	–
Layered	B8054	2400	10 17 25	1500	55%	14	41.4	–
Layered	B8055	2400	10 17 25	1500	55%	15	29.6	33.08
Mixed	B8056	2400	10 17 25	1500	55%	14	23.24	–
Mixed	B8057	2400	10 17 25	1500	55%	14	67.1	–
Mixed	B8058	2400	10 17 25	1500	55%	14	117.9	–
Mixed	B8059	2400	10 17 25	1500	55%	14	23	–
Mixed	B8060	2400	10 17 25	1500	55%	14	82.3	62.71
Layered	B8061	2400	10 14 17 20 25	1500	55%	15	33.9	–
Layered	B8062	2400	10 14 17 20 25	1500	55%	15	95.1	–
Layered	B8063	2400	10 14 17 20 25	1500	55%	15	80.3	–
Layered	B8064	2400	10 14 17 20 25	1500	55%	15	168.4	–
Layered	B8065	2400	10 14 17 20 25	1500	55%	15	90.7	93.68
Mixed	B8066	2400	10 14 17 20 25	1500	55%	14	75.3	–
Mixed	B8067	2400	10 14 17 20 25	1500	55%	14	72.2	–
Mixed	B8068	2400	10 14 17 20 25	1500	55%	14	119.6	–
Mixed	B8069	2400	10 14 17 20 25	1500	55%	14	154.2	–
Mixed	B8070	2400	10 14 17 20 25	1500	55%	14	232.5	130.76
Layered	B8081	2400	10 14 20	1500	55%	14	102.7	–
Layered	B8082	2400	10 14 20	1500	55%	14	51.4	–
Layered	B8083	2400	10 14 20	1500	55%	14	34	–
Layered	B8084	2400	10 14 20	1500	55%	14	28	–
Layered	B8085	2400	10 14 20	1500	55%	14	45.7	52.36
Mixed	B8086	2400	10 14 20	1500	55%	13	80.8	–
Mixed	B8087	2400	10 14 20	1500	55%	13	92.8	–
Mixed	B8088	2400	10 14 20	1500	55%	13	99.8	–
Mixed	B8089	2400	10 14 20	1500	55%	13	110	–
Mixed	B8090	2400	10 14 20	1500	55%	13	56.1	87.9
Mixed	B8071	2400	10 14 17 20 25	3000	55%	26	184.6	–
Mixed	B8072	2400	10 14 17 20 25	3000	55%	26	152.3	–
Mixed	B8073	2400	10 14 17 20 25	3000	55%	26	171.9	169.6
Mixed	B8091	2400	10 14 20	3000	55%	26	85	–
Mixed	B8092	2400	10 14 20	3000	55%	26	40.1	–
Mixed	B8093	2400	10 14 20	3000	55%	26	248.7	–
Mixed	B8094	2400	10 14 20	3000	55%	26	32.8	101.65
Mixed	B8095	2400	10 14 20	4500	55%	39	190	–

1400 kg/m³

Situation (-)	Test N. (-)	ρ_s (kg/m ³)	d (mm)	w_s (g)	C_i (kg/m ³)	\bar{h}_b (cm)	Throughput (g)	Avg Throughput (g)
Layered	B7051	1400	10 17 25	878.01	55%	15	0	–
Layered	B7052	1400	10 17 25	878.01	55%	15	0	–
Layered	B7053	1400	10 17 25	878.01	55%	15	15	5
Mixed	B7056	1400	10 17 25	878.01	55%	14	48	–
Mixed	B7057	1400	10 17 25	878.01	55%	14	25	–
Mixed	B7058	1400	10 17 25	878.01	55%	14	72.1	48.37
Layered	B7061	1400	10 14 17 20 25	878.01	55%	15	5	–
Layered	B7062	1400	10 14 17 20 25	878.01	55%	15	0	–
Layered	B7063	1400	10 14 17 20 25	878.01	55%	15	0	1.67
Mixed	B7066	1400	10 14 17 20 25	878.01	55%	14	0	–
Mixed	B7067	1400	10 14 17 20 25	878.01	55%	14	0	–
Mixed	B7068	1400	10 14 17 20 25	878.01	55%	14	5	1.67
Layered	B7081	1400	10 14 20	878.01	55%	15	0	–
Layered	B7082	1400	10 14 20	878.01	55%	15	0	–
Layered	B7083	1400	10 14 20	878.01	55%	15	0	0

Continued on next page...

Situation (-)	Test N. (-)	ρ_s (kg/m ³)	d (mm)	w_s (g)	C_i (kg/m ³)	\bar{h}_b (cm)	Throughput (g)	Avg Throughput (g)
Mixed	B7086	1400	10 14 20	878.01	55%	14	5	–
Mixed	B7087	1400	10 14 20	878.01	55%	14	1	–
Mixed	B7088	1400	10 14 20	878.01	55%	13.5	2	2.67
Gemixed	B8091	1400	10 14 20	1750.02	55%	–	5	–

Pump Two Phase Three 2400 kg/m³

Situation (-)	Test N. (-)	ρ_s (kg/m ³)	d (mm)	w_s (g)	C_i (kg/m ³)	\bar{h}_b (cm)	Throughput (g)	Avg Throughput (g)
Layered	B9051	2400	10 14 17 20 25	1500.00	55%	14	1439.20	–
Layered	B9052	2400	10 14 17 20 25	1500.00	55%	14	1263.00	–
Layered	B9053	2400	10 14 17 20 25	1500.00	55%	14	1048.00	–
Layered	B9054	2400	10 14 17 20 25	1500.00	55%	–	1228.10	–
Layered	B9055	2400	10 14 17 20 25	1500.00	55%	–	1208.15	1237.29
Mixed	B9056	2400	10 14 17 20 25	1455.20	55%	13	1436.20	–
Mixed	B9057	2400	10 14 17 20 25	1495.30	55%	13	1482.80	–
Mixed	B9058	2400	10 14 17 20 25	1482.60	55%	13	1482.60	–
Mixed	B9059	2400	10 14 17 20 25	1518.00	55%	13	1518.00	–
Mixed	B9060	2400	10 14 17 20 25	1477.00	55%	13	1382.30	1460.38
Mixed	B9061	2400	10 14 17 20 25	2961.00	55%	26	2608.00	–
Mixed	B9062	2400	10 14 17 20 25	2967.00	55%	26	2580.10	–
Mixed	B9063	2400	10 14 17 20 25	2988.60	55%	–	2546.00	2578.03

1400 kg/m³

Situation (-)	Test N. (-)	ρ_s (kg/m ³)	d (mm)	w_s (g)	C_i (kg/m ³)	\bar{h}_b (cm)	Throughput (g)	Avg Throughput (g)
Layered	B9001	1400	10 14 17 20 25	878.01	55%	15	511.40	–
Layered	B9002	1400	10 14 17 20 25	878.01	55%	15	460.00	–
Layered	B9003	1400	10 14 17 20 25	878.01	55%	15	572.00	–
Layered	B9004	1400	10 14 17 20 25	878.01	55%	15	376.00	–
Layered	B9005	1400	10 14 17 20 25	878.01	55%	15	482.30	480.34
Mixed	B9006	1400	10 14 17 20 25	878.01	55%	14	587.60	–
Mixed	B9007	1400	10 14 17 20 25	878.01	55%	14	470.70	–
Mixed	B9008	1400	10 14 17 20 25	878.01	55%	14	489.90	–
Mixed	B9009	1400	10 14 17 20 25	878.01	55%	14	556.10	–
Mixed	B9010	1400	10 14 17 20 25	878.01	55%	14	522.00	525.26
Layered	B9021	1400	10 14 20	875.01	55%	15	318.00	–
Layered	B9022	1400	10 14 20	875.01	55%	15	343.00	–
Layered	B9023	1400	10 14 20	875.01	55%	15	384.00	348.33
Mixed	B9026	1400	10 14 20	855.00	55%	14	290.30	–
Mixed	B9027	1400	10 14 20	863.20	55%	13	325.00	–
Mixed	B9028	1400	10 14 20	872.00	55%	14	329.00	314.77
Layered	B9031	1400	10 17 25	875.01	55%	–	229.00	–
Layered	B9032	1400	10 17 25	875.01	55%	–	406.00	–
Layered	B9033	1400	10 17 25	875.01	55%	–	366.00	333.67
Mixed	B9036	1400	10 17 25	875.01	55%	–	371.00	–
Mixed	B9037	1400	10 17 25	867.00	55%	–	283.00	–
Mixed	B9038	1400	10 17 25	857.00	55%	–	379.00	–
Mixed	B9039	1400	10 17 25	866.00	55%	–	346.00	344.75
Mixed	B9011	1400	10 14 17 20 25	1745.00	55%	27	567.00	–
Mixed	B9012	1400	10 14 17 20 25	1740.00	55%	27	567.30	–
Mixed	B9013	1400	10 14 17 20 25	1710.00	55%	27	743.00	625.77